UNIVERSITÀ DEGLI STUDI DI PADOVA

Dipartimento di Fisica e Astronomia “Galileo Galilei”

Master Degree in Physics

Thesis

Boosting the physics performances of the ENUBET monitored neutrino beam with a redesign of the hadron beamline

Supervisor
Prof. Andrea Longhin
Co-supervisor
Dott. Fabio Pupilli

Student
Luigi Zappacosta

Academic Year 2024/2025

Pagina lasciata vuota intenzionalmente.

Abstract

The ENUBET project is addressing the possibility of building a facility for high precision neutrino cross-section measurements leveraging on the concept of “monitored beams”. These are facilities in which the neutrino flux could be accurately predicted by measuring the rates of charged leptons produced in a fully instrumented decay region. The R&D has demonstrated the possibility of building a beamline based on static focusing elements to perform a ν_e cross section measurement in the DUNE energy range with 1% statistical uncertainty employing 1.4×10^{19} 400 GeV protons on target (PoT), achieving a sample of about 10^6 ν_μ CC events and 1.2×10^4 ν_e CC events over a detector with a 500 t mass. The instrumentation of the decay tunnel, based on a cost effective sampling calorimeter solution, has been tested with a large scale prototype achieving the performance required to identify positrons and muons from kaon decays with high signal-to-noise ratio. The systematics budget on the neutrino flux is constrained at the 1% level by fitting the charged leptons observables. Based on these successful results ENUBET is now pursuing a study for a site dependent implementation at CERN in the framework of the “Physics Beyond Colliders” initiative.

In this context a new beamline, able to enrich the neutrino flux at the energy of HK and to reduce by more than a factor 3 the needed pot, has been designed and is being optimized. This beamline is currently only simulated with a tool (BDSIM) that limits the analysis needed to assess the achievable systematic uncertainty on the neutrino flux. I this thesis I implemented this improved beamline into the GEANT4 framework. This powerful simulation has been used to fully characterize the potential of the new setup. In particular the study involves a re-evauation of the performances of the previous beamline for the operation in “time-tagged” mode and the possibility to exploit the position of the interacting neutrino to have a prior on its energy (“narrow-band off-axis” technique). The latter technique has been exploited in particular to estimate the performances for measuring the cross-section of neutral current events with production of neutral pions.

The optics of the new beamline have been studied with the possibility of inserting high-granularity and fast silicon detectors (similar to the “Giga-tracker” detector used in the NA-62 experiment). GEANT4 data allows understanding the requirements for these detectors in terms of geometry and time-resolution to be able to operate in the running conditions of the experiment which characterized by an extremely high particle flux.

In addition an optimization of the shielding in the region close to the proton target has been carried out in order to reduce the fraction of neutrinos that are not produced in the instrumented decay region.

Contents

1 Neutrino physics and the ENUBET project 5
- 1.1 Theoretical introduction 5
  - 1.1.1 Oscillation theory and experimental data 5
  - 1.1.2 Cross-section theory and experimental data 8
- 1.2 Neutrino beams 11
- 1.3 The ENUBET project 14
  - 1.3.1 Motivations 14
  - 1.3.2 Beamline and instrumented decay tunnel 15
  - 1.3.3 Events tagging and background discrimination 18
  - 1.3.4 NuTag integration 18

2 Beamline simulation 20
- 2.1 Beamline design considerations 20
- 2.2 Introduction to Geant4 22
  - 2.2.1 Main classes and functions 22
  - 2.2.2 Particle propagation 25
  - 2.2.3 From BDSIM to Geant4 27
- 2.3 Beamline modeling 28
  - 2.3.1 Target 28
  - 2.3.2 Dipoles 29
  - 2.3.3 Quadrupoles 30
  - 2.3.4 Collimators 31
  - 2.3.5 Decay tunnel 32
  - 2.3.6 Outer elements 33
- 2.4 Detectors simulation 36
  - 2.4.1 NuTag detectors 36
  - 2.4.2 Virtual detectors 36
- 2.5 Simulation and data handling 38

3 Simulation results 40
- 3.1 Particle budget 40
  - 3.1.1 Particle production at target 40
  - 3.1.2 Positron reduction 43
  - 3.1.3 Beamline yield 45
  - 3.1.4 Neutrinos budget 49
- 3.2 Shielding optimization studies 53
  - 3.2.1 Benchmark designs 55
  - 3.2.2 Additional target shielding studies 59

3.2.3 Additional studies on the shielding along the beamline . . . 62
3.2.4 Dipole shieldings studies 67
3.2.5 Final design 70

Chapter 1

Neutrino physics and the ENUBET project

In the last few decades, neutrino physics has become one of the most important and relevant physics sectors due to its capability at probing for physics beyond the Standard Model. Moreover, neutrino physics is also related to cosmological problems, such as matter-antimatter asymmetry in our Universe.

To find answers to such problems we thus need to study how neutrinos interact with other particles; in particular, neutrinos cross section is an important value to measure, as it is linked to most of systematic errors in other neutrino measurements. A deep understanding of neutrinos cross section across different energy ranges is thus needed, but the main limit on cross-section measurements precision comes from neutrino flux estimations: the precision that can be achieved is usually larger than 10% [1], but $\sim 1\%$ precision is needed.

ENUBET was proposed to address this precision requirements on neutrino fluxes: tagging charged leptons produced along with neutrinos in mesons decay, the main mode of neutrino productions in beamline setups, it is possible to achieve high precision neutrino flux estimations.

1.1 Theoretical introduction

Neutrinos are assumed massless in the Standard Model. In reality, neutrino flavor oscillation proves that neutrinos have a non zero mass, albeit it is very small, below the eV threshold. First proofs of this phenomenon came from solar neutrino flux measurements at SNO.

1.1.1 Oscillation theory and experimental data

Neutrino mass in introduced in the *minimally expanded Standard Model* by extending the Standard model with right-handed neutrinos $\nu_{\ell R}$ [2]. The newly added fields are sterile because they are singlets under SM symmetries. The Yukawa lepton sector is thus extended, accounting for a new *neutrino mass term*:

$$\mathscr{L}_{H,L} = -\frac{v+h}{\sqrt{2}} \left(\overline{\ell'_L} Y'_\ell \ell'_R + \overline{\nu'_L} Y'_\nu \nu'_R \right) + \text{H.c.} \tag{1.1}$$

With

$$\nu'_L = \begin{pmatrix} \nu'_{eL} \\ \nu'_{\mu L} \\ \nu'_{\tau L} \end{pmatrix} \tag{1.2}$$

Y'_ν is the neutrino Yukawa couplings matrix and can be diagonalizes as $Y_\nu = V_L^{\nu\dagger} Y'_\nu V_R^\nu$. Equation 1.1 thus yields:

$$\mathscr{L}_{H,L} = -\frac{v+h}{\sqrt{2}} \left(\overline{\ell_L} Y_\ell \ell_R + \overline{n_L} Y_\nu n_R \right) + \text{H.c.} \tag{1.3}$$

where

$$n_{L,R} = \nu_{L,R} V_{L,R}^{\nu\dagger} = \begin{pmatrix} \nu_{1L,R} \\ \nu_{2L,R} \\ \nu_{3L,R} \end{pmatrix} \tag{1.4}$$

are the neutrino mass eigenstate vectors. With this definition we can calculate the weak leptonic charged current as

$$J^\rho = 2\overline{n_L} U^\dagger \gamma^\rho \ell_L \tag{1.5}$$

with $U = V_L^{\ell\dagger} V_L^\nu$ and the left handed neutrino fields conventionally defined as

$$\nu_L = U n_L, \ \text{ with } \ \nu_L = \begin{pmatrix} \nu_{e,L} \\ \nu_{\mu,L} \\ \nu_{\tau,L} \end{pmatrix}$$

and thus Equation 1.5 becomes

$$J^\rho = 2 \sum_{\alpha=e,\mu,\tau} \nu_{\alpha L} \gamma^\rho \ell_{\alpha L} \tag{1.6}$$

$U \equiv V_L^{\ell\dagger} V_L^\nu$ is the *Pontecorvo–Maki–Nakagawa–Sakata matrix* and it is not diagonal, thus a flavor eigenstate $|\nu_\ell\rangle$ does not correspond to a mass eigenstate $|\nu_i\rangle$ but it is instead a superpositions of all mass eigenstates:

$$|\nu_\ell\rangle = \sum_{i=1}^{3} U_{\ell i}^* |\nu_i\rangle \tag{1.7}$$

U_{PMNS} is a 3×3 matrix, thus depends on 9 parameters. These parameters can be divided into $\frac{N(N-1)}{2} = 3$ mixing angles, called θ_{12}, θ_{13} and θ_{23}, and $\frac{N(N+1)}{2} = 6$ phases; however it can be proved that 5 of these 6 phases induce global phases transformations under whose the SM Lagrangian is invariant, and thus are not real physical phases. The only leftover is δ_{CP}, that is the phase related to CP symmetry violations in neutrino oscillations.

Defining $c_{ij} = \cos\theta_{ij}$ and $s_{ij} = \sin\theta_{ij}$ U_{PMNS} can be rewritten as follows:

$$\begin{aligned} U^D_{PMNS} &= \begin{pmatrix} 1 & 0 & 0 \\ 0 & c_{23} & s_{23} \\ 0 & -s_{23} & c_{23} \end{pmatrix} \cdot \begin{pmatrix} c_{13} & 0 & s_{13}e^{-i\delta_{CP}} \\ 0 & 1 & 0 \\ -s_{13}e^{i\delta_{CP}} & 0 & c_{13} \end{pmatrix} \cdot \begin{pmatrix} c_{12} & s_{12} & 0 \\ -s_{12} & c_{12} & 0 \\ 0 & 0 & 1 \end{pmatrix} \\ &= \begin{pmatrix} c_{12}c_{13} & s_{12}c_{13} & s_{12}e^{-i\delta_{CP}} \\ -s_{12}c_{23} - c_{12}s_{23}s_{13}e^{i\delta_{CP}} & c_{12}c_{23} - s_{12}s_{23}s_{13}e^{i\delta_{CP}} & s_{23}c_{13} \\ s_{12}s_{23} - c_{12}c_{23}s_{13}e^{i\delta_{CP}} & -c_{12}s_{23} - s_{12}c_{23}s_{13}e^{i\delta_{CP}} & c_{23}c_{13} \end{pmatrix} \end{aligned} \tag{1.8}$$

If neutrinos are Majorana particles, there will be three physical phases instead of one, and the new U_{PMNS} will be

$$U^M_{PMNS} = U^D_{PMNS} \cdot \mathcal{M}_p, \qquad \mathcal{M}_p = \begin{pmatrix} 1 & 0 & 0 \\ 0 & e^{i\alpha_1/2} & 0 \\ 0 & 0 & e^{i\alpha_2/2} \end{pmatrix} \tag{1.9}$$

The important consequence of Equation 1.7 is that neutrinos do not conserve flavor during travel. Mass eigenstates are Hamiltonian eigenstates and evolve as plane waves:

$$|\nu_k(t)\rangle = e^{-iE_k t}\,|\nu_k\rangle \tag{1.10}$$

Applying Equation 1.10 in Equation 1.7 the evolution of a flavor eigentates yields:

$$|\nu_\alpha(t)\rangle = \sum_{\beta=e,\nu,\tau} \left(\sum_k U^*_{\alpha k} e^{-iE_k t} U_{\beta k} \right) |\nu_\beta\rangle \tag{1.11}$$

Thus, because U_{PMNS} is non diagonal, a flavor states evolves into a superposition of all flavor states; this is what causes the *neutrino oscillation* phenomenon. The oscillation probability from flavor α to β is found as:

$$\begin{aligned} P_{\nu_\alpha \to \nu_\beta}(t) &= \sum_{k,j} U^*_{\alpha k} U_{\beta k} U_{\alpha j} U^*_{\beta j} e^{-i(E_k - E_J)t} \\ &\simeq \sum_{k,j} U^*_{\alpha k} U_{\beta k} U_{\alpha j} U^*_{\beta j} \exp\left(-i \frac{\Delta m^2_{kj} L}{2E} \right) \end{aligned} \tag{1.12}$$

where the second formula was found in ultra-relativistic approximation:

$$\begin{aligned} E_k &\simeq E + \frac{m_k^2}{2E} \\ \Rightarrow E_k - E_j &\simeq \frac{m_k^2 - m_j^2}{2E} = \frac{\Delta m^2_{kj}}{2E} \end{aligned} \tag{1.13}$$

and is the most commonly used.

Equation 1.12 can be rewritten as

$$\begin{aligned} P_{\nu_\alpha \to \nu_\beta} = \delta_{\alpha\beta} &- 4 \sum_{i>j} \mathrm{Re}\left(U^*_{\alpha i} U_{\beta i} U_{\alpha j} U^*_{\beta j} \right) \sin\left(\frac{1.267 \cdot \Delta m^2_{ij}(\mathrm{eV}^2) L(\mathrm{km})}{E(\mathrm{GeV})} \right) \\ &+ 2 \sum_{i>j} \mathrm{Im}\left(U^*_{\alpha i} U_{\beta i} U_{\alpha j} U^*_{\beta j} \right) \sin\left(\frac{2.534 \cdot \Delta m^2_{ij}(\mathrm{eV}^2) L(\mathrm{km})}{E(\mathrm{GeV})} \right) \end{aligned} \tag{1.14}$$

This formulas only account for neutrino traveling in a vacuum. In matter, due to $e^- - \nu_e$ charged current weak interactions, the effective neutrino masses are slightly different than the vacuum neutrino masses, changing also oscillation probabilities; this is known as the *Mikheyev–Smirnov–Wolfenstein effect* (MSW effect for short) [3]. One can also define the oscillation length: $L_{osc} = 4E/\Delta m^2_{ij}$

A neutrino oscillation experiment should set up in such a way that $E/L \simeq \Delta m^2_{ij}$: if $L \gg L_{osc}$, the term $\sin^2(L/L_{osc})$ oscillates rapidly and it averages out to $\langle \sin^2(L/L_{osc}) \rangle = \frac{1}{2}$ and there is no oscillation pattern; if instead $L \ll L_{osc}$, neutrinos have no time to oscillates and the oscillation probabilities cannot be properly measured [4]. Because $\Delta m^2_{21} \equiv \Delta m^2_{sol} \ll \Delta m^2_{32}$ and as such $\Delta m^2_{32} \approx \Delta m^2_{31} \equiv \Delta m^2_{atm}$, in the condition described above $\nu_e \leftrightarrow \nu_\mu$ oscillations become predominant and the formulas below can be used as an approximation in place of Equation 1.14 [4]:

$$P_{\nu_e \to \nu_e} \approx 1 - \sin^2(2\theta_{13}) \sin^2 \left(1.267 \Delta m^2_{31} \frac{L}{E} \right) \tag{1.15}$$

$$P_{\nu_\mu \to \nu_e} = P_{\nu_e \to \nu_\mu} \approx \sin^2(2\theta_{13}) \sin^2(\theta_{23}) \sin^2 \left(1.267 \Delta m^2_{31} \frac{L}{E} \right) \tag{1.16}$$

$$P_{\nu_\mu \to \nu_\mu} \approx 1 - 4\cos^2(\theta_{13}) \sin^2(\theta_{23}) \left(1 - \cos^2(\theta_{13}) \sin^2(\theta_{23})\right) \sin^2 \left(1.267 \Delta m^2_{31} \frac{L}{E} \right) \tag{1.17}$$

These are the formulas used to fit data and estimate oscillation parameters in neutrinos experiments. Up-to-date oscillation parameters are reported in Table 1.1, and are results of fit from global data [5].

	Normal ordering		**Inverted ordering** ($\Delta\chi^2 = 6.1$)	
	Best fit $\pm 1\sigma$	3σ **range**	**Best fit** $\pm 1\sigma$	3σ **range**
θ_{12} (°)	$33.68^{+0.73}_{-0.12}$	$31.635 - 35.95$	$33.68^{+0.73}_{-0.12}$	$31.635 - 35.95$
θ_{23} (°)	$43.3^{+1.0}_{-0.8}$	$41.3 - 49.9$	$47.9^{+0.7}_{-0.9}$	$41.5 - 49.8$
θ_{13} (°)	$8.56^{+0.11}_{-0.11}$	$8.19 - 8.89$	$8.59^{+0.11}_{-0.11}$	$8.25 - 8.93$
δ_{CP} (°)	212^{+26}_{-41}	$124 - 364$	274^{+22}_{-25}	$201 - 335$
$\frac{\Delta m^2_{21}}{10^{-5}}$ (eV^2)	$7.49^{+0.19}_{-0.19}$	$6.92 - 8.05$	$7.49^{+0.19}_{-0.19}$	$6.92 - 8.05$
$\frac{\Delta m^2_{3\ell}}{10^{-3}}$ (eV^2)	$+2.513^{+0.021}_{-0.019}$	$+2.451 - +2.578$	$-2.484^{+0.020}_{-0.020}$	$-2.574 - -2.421$

Table 1.1: Oscillation parameters. From [5, 6]

It is also of notice that, because oscillation experiments can only measure the squared mass differences and not the absolute neutrino masses, there are two possible *neutrino mass hierarchies* possible for mass eigenstates; which one of those is the real one is still unknown.

1.1.2 Cross-section theory and experimental data

Neutrino detection techniques are based on their interaction with regular matter through weak current interactions, either neutral or charged current events, since appearance and disappearance probabilities are calculated from the interaction rate

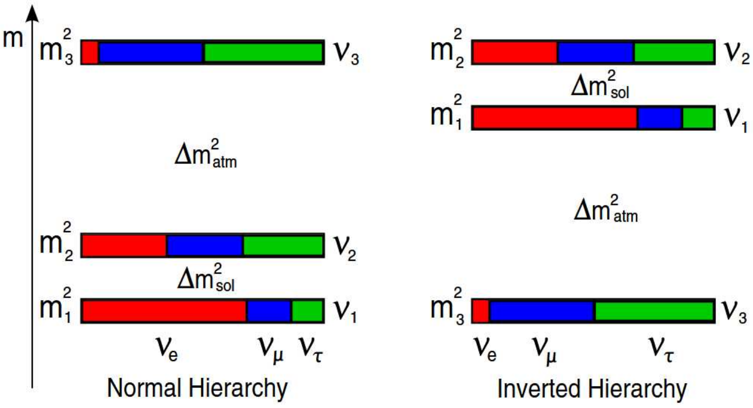

Figure 1.1: Neutrino hierarchies schemes.

of neutrinos in the detector. As such, an accurate estimation of oscillation parameters requires a precise estimation of neutrino cross section in the MeV-GeV energy range, as it is the most common energy range for accelerator neutrino experiments.

Neutrino cross sections can be calculated in the Standard Model, as neutrino masses are very small (<eV) and a massless neutrino is a good enough approximation for these calculations. Main focus is on charged current interactions with nucleons, as they're the easiest to detect since a charged lepton is produced and are also the only interaction that gives leptonic flavor information. Most up to date data is reported in Figure 1.2.

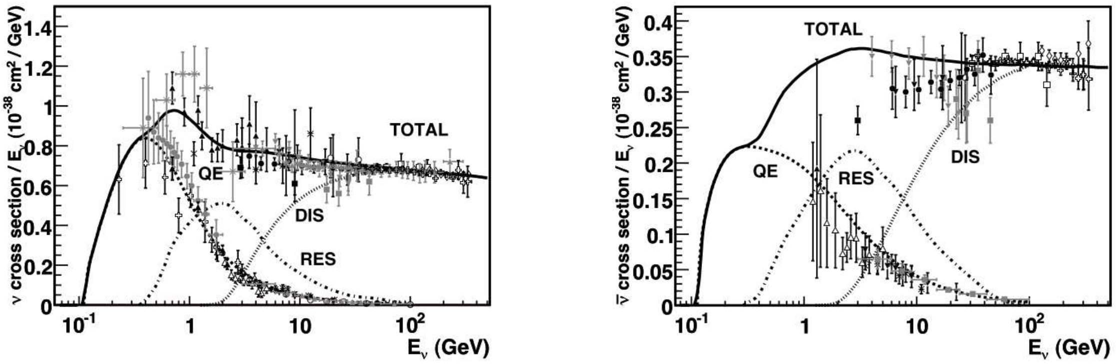

Figure 1.2: Neutrino (left) and antineutrino (right) cross sections as a function of E_ν. From [7].

Quasi-elastic neutrino-nucleon scattering

Those are interactions in which the impacted nucleon does not split up. Those are the predominant interactions for energies lower than $E_\nu \sim 2$ GeV [7]:

$$\begin{array}{lll} \textbf{CC:} & \nu_\ell + n \rightarrow \ell^- + p & \overline{\nu_\ell} + p \rightarrow \ell^+ + n \\ \textbf{NC:} & \nu_\ell + n/p \rightarrow \nu_\ell + n/p & \overline{\nu_\ell} + n/p \rightarrow \overline{\nu_\ell} + n/p \end{array}$$

Thresholds are given by energy conservation: in the Lab F.o.R.

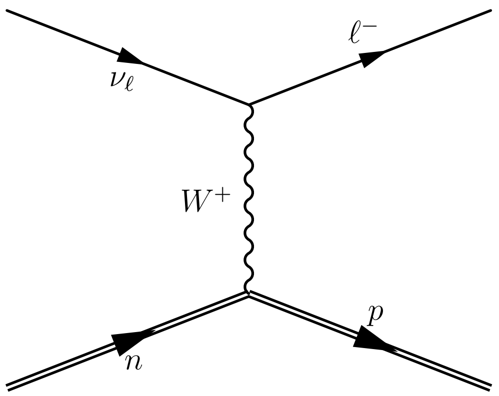

$s = (\mathbf{p}_\nu + \mathbf{p_n}) = (E_\nu + m_n)^2 - E_\nu^2$

Condition for production is $s > (m_\ell + m_p)^2$

$\Rightarrow E_{th,\ell} = \frac{(m_p - m_n)^2 + m_\ell^2 + 2m_p m_\ell}{2m_n}$

Threshold energies for lepton productions are written in Table 1.2

Lepton	e	μ	τ
Production threshold	0 eV	110 MeV	3.5 GeV

Table 1.2: Thresholds for lepton productions in quasi-elastic CC scatterings

Resonant production

When the neutrino energy is around $E_\nu \sim$ GeV it can undergo resonant pion production when scattering against a nucleon, through the excitation of baryonic resonances. This phenomenon dominates in the GeV energy range:

$$\begin{aligned} \textbf{CC:} &\quad \nu_\ell + N \to \ell' + N' + \pi \\ \textbf{NC:} &\quad \nu_\ell + n/p \to \nu_\ell + n/p + \pi \end{aligned}$$

Deep inelastic scattering

For $E_\nu \gg$GeV, neutrinos have a high enough energy to break nuclei and undergo deep inelastic scattering (DIS), producing an hadron shower along with the charged lepton from CC interaction:

$$\begin{aligned} \textbf{CC:} &\quad \nu_\ell + N \to \ell^- + X & \qquad \overline{\nu_\ell} + N \to \ell^+ + X \\ \textbf{NC:} &\quad \nu_\ell + N \to \nu_\ell + X & \qquad \overline{\nu_\ell} + N \to \overline{\nu_\ell} + X \end{aligned}$$

Electron scattering

Electron scattering is an interaction with no threshold energy in which a neutrino and an electron interact via weak current:

$$\nu_\ell + e^- \to \nu_\ell + e^-$$

For $\nu_{\mu,\tau}$ and $\overline{\nu}_{\mu,\tau}$, only NC interactions contribute to the cross section, while for ν_e and $\overline{\nu}_e$ CC interactions are also possible. The result is a redistribution of energy between the electron and the neutrino. Because the interaction is at a low energy, $\sqrt{s} \ll M_W, M_Z$ and we can use an EFT approximation:

$$\mathcal{L}_{\text{eff}}\left(\overset{(-)}{\nu}_e e^- \to \overset{(-)}{\nu}_e e^-\right) = -\frac{G_F}{\sqrt{2}}\left[\overline{\nu_e}\gamma^\rho(1-\gamma^5)\nu_e\right]\left[\overline{e}\gamma_\rho\left((1+g_V^l) - (1+g_A^l)\gamma^5\right)e\right] \tag{1.18}$$

$$\mathcal{L}_{\text{eff}}\left(\overset{(-)}{\nu}_{\alpha}e^{-}\to\overset{(-)}{\nu}_{\alpha}e^{-}\right)=-\frac{G_F}{\sqrt{2}}\left[\overline{\nu_\alpha}\gamma^{\rho}(1-\gamma^{5})\nu_\alpha\right]\left[\bar{e}\gamma_{\rho}\left(g_V^{l}-g_A^{l}\gamma^{5}\right)e\right]\quad(\alpha=\mu,\tau)\tag{1.19}$$

where G_F is the Fermi constant. Measurements for electron-neutrino cross sections at $\sqrt{s}\gg m_e$ are reported in Table 1.3; θ_W is the Weimberg angle. The different cross-section between electron neutrinos and the two other flavored neutrinos are what causes the MSW effect discussed before: ν_e interacts more often with matter electrons and thus their flux is dampened.

Process	**Total cross-section**
ν_e+e^-	$\left(\frac{G_F^2 s}{4\pi}\right)\left[\left(1+2\sin^2\vartheta_W\right)^2+\frac{4}{3}\sin^4\vartheta_W\right]\simeq 93\ \text{s/MeV}^2$
$\bar{\nu}_e+e^-$	$\left(\frac{G_F^2 s}{4\pi}\right)\left[\frac{1}{3}\left(1+2\sin^2\vartheta_W\right)^2+4\sin^4\vartheta_W\right]\simeq 39\ \text{s/MeV}^2$
$\nu_{\mu,\tau}+e^-$	$\left(\frac{G_F^2 s}{4\pi}\right)\left[\left(1-2\sin^2\vartheta_W\right)^2+\frac{4}{3}\sin^4\vartheta_W\right]\simeq 15\ \text{s/MeV}^2$
$\bar{\nu}_{\mu,\tau}+e^-$	$\left(\frac{G_F^2 s}{4\pi}\right)\left[\frac{1}{3}\left(1-2\sin^2\vartheta_W\right)^2+4\sin^4\vartheta_W\right]\simeq 13\ \text{s/MeV}^2$

Table 1.3: Total cross-sections for neutrino-electron scattering processes.

1.2 Neutrino beams

In the context of oscillation experiments, neutrino beams are essential tools for experimental setups, as they permit a good control on neutrino parameters, in particular their energy, their leptonic flavor, and the distance from detector at which they are produced.

A general neutrino beam structure is reported in Figure 1.3. To start neutrino production a proton beam, extracted from an accelerator, is sent against a light target, usually made of graphite, aluminum or beryllium. Protons from the beam interact with target nuclei, producing a secondary beam mainly made of mesons (π^+, K^+), but photons, $e^\pm$ and free baryons (p,n) are also present. The secondary beam passes through a momentum-charge filtering system, that selects charged mesons of required momentum and sends them into the decay tunnel. Both incoming proton energy and selected momentum are crucial parameters, as neutrinos cannot be focused or selected by their momentum, being chargeless particles.

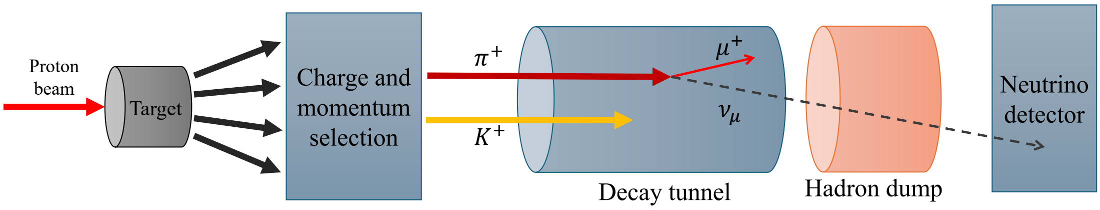

Figure 1.3: Neutrino beamline schematics

Historically, mesons momentum selection has been done using magnetic horns, producing so-called Wide Band Beams with high intensity but a wide momentum range. Magnetic horns however are sensible to overheating, so a more modern approach is using a combination of magnetic dipole, for momentum selection, ad quadrupoles, for beam focusing. This approach produces Narrow Band Beams, with small neutrino energy range, reduced backgrounds but lower fluxes.

The mesons beam is then sent in the decay tunnel, where they mainly decay into muons and muonic neutrinos, as reported in Table 1.4. The neutrino will thus be mainly made of muonic neutrinos, with a small fraction of electronic neutrinos from K^+ decays. At the end of the decay tunnel an hadron dump is placed to absorb all leftover mesons that haven't decayed and to prevent them from propagate further. Since mesons mainly decays into a $\mu^+ + \nu_\mu$ couple, after the beam dump we have only neutrinos and some leftover muons; usually muon detectors are placed after the hadron dump, in order to estimate the neutrino flux. Otherwise, the only way to estimate neutrino flux is from the primary beam rate and secondary production models, however this yields high uncertainties in total neutrino production.

Decay	**Branching ratio**	**Conf. level (MeV/c)**
$\pi^+ \to \mu^+\nu_\mu$	$(99.98770 \pm 0.00004) \times 10^2$	30
$\pi^+ \to e^+\nu_e$	$(1.230 \pm 0.004) \times 10^4$	30
$K^+ \to \mu^+\nu_\mu$	$(63.56 \pm 0.11) \times 10^2$	247
$K^+ \to e^+\pi_0\nu_e$	$(5.07 \pm 0.04) \times 10^2$	228
$K^+ \to \mu^+\pi_0\nu_\mu$	$(3.352 \pm 0.034) \times 10^2$	215

Table 1.4: Branching ratio of most common leptonic decays for π^+,K^+, from [8].

Decay tunnel length needs to be optimized such that most of mesons decay with little to no muon decays in the tunnel. Decay probability for a meson in the tunnel is $P = 1 - e^{-L/L_0}$, where L is the tunnel length and

$$L_0 = \beta\gamma\tau_M c = \frac{p_M}{m_M}\tau_M c = \begin{cases} 5.59 \text{ m} \cdot \frac{p_\pi}{\text{GeV}} & \text{for } \pi^+ \\ 7.51 \text{ m} \cdot \frac{p_K}{\text{GeV}} & \text{for } K^+ \end{cases} \tag{1.20}$$

is the meson decay length. We only expect a portion of mesons to decay into the tunnel.

Neutrino energy spectrum and angular distributions can be derived from the two-body kinematics of mesons decay [2]. Remembering that in the center-of-mass frame of reference

$$E_{\nu,cm} = \frac{m_M}{2}\left(1 - \frac{m_\mu^2}{m_M^2}\right)$$

which in the laboratory frame of reference, for small angle approximation, yields

$$E_\nu = \left(1 - \frac{m_\mu^2}{m_M^2}\right)\left(1 - \frac{E_M}{m_M}\right)^{-1}\frac{E_M}{\theta^2} \tag{1.21}$$

which means that for off-axis neutrinos energy have stronger dependence on angle than mesons energy. This can be used in off-axis experiment to have a monochromatic neutrino beams, although this also greatly reduces neutrino flux. In fact,

$\phi(\theta)$ can be calculated as

$$\phi(\theta) = \frac{dN}{d\cos\theta} \propto \left(\frac{2}{1 + \frac{E_M^2}{m_M^2}\theta^2} \right)^2 \frac{1}{z^2} \tag{1.22}$$

where z is the source-detector distance. One can see that $\phi(\theta) \propto \theta^{-4}$, so off-axis neutrino experiments requires very high beam fluxes at source. Energy distributions and flux suppression graphs are reported in Figure 1.4.

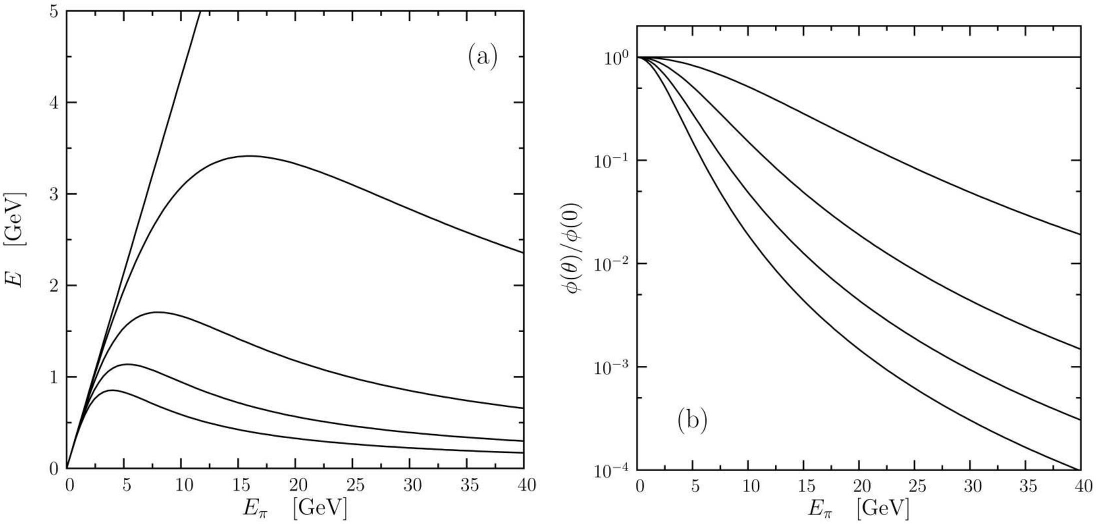

Figure 1.4: Left: Neutrino energy distribution as a function of E_M, for different angles. Right: flux suppression function $(\phi(0)/\phi(\theta))$ as a function of E_M. Curves corresponds to angles $\theta = 0.0°, 0.5°, 1.0°, 1.5°, 2.0°$. From [2].

Some neutrino beamlines used in oscillation experiments in the past are:

- The **K2K experiment** (KEK to Kamioka) was the first long baseline experiment. It was an on-beam experiment, with neutrinos energy in the $[1.0 - 1.5]$ GeV range. Neutrinos were produced by extracting 12 GeV protons from the KEK synchrotron and sending the against an aluminum target [9]. The beamline focused pions using two magnetic horns, and employed both a pion and a muon monitor [10]. Data was taken from 1999 to 2004 and confirmed ν_μ disappearance and oscillation parameters estimation from SuperKamiokande atmospheric neutrinos data [9].
- **NuMI** beam is located at the Fermi National Accelerator Laboratory and it was initially constructed primarily for the MINOS experiment. Protons from the Main Injector (MI) accelerator with a momentum of 120 GeV/c are used for the production of neutrinos and antineutrinos with an average momentum of 3 GeV/c. The beamline was designed to be flexible in parameters, with the possibility of switching between ν_μ and $\overline{\nu}_\mu$ production depending on horns polarizations [10]. Data acquisition started in 2005 and ended in 2012, resulting in the first set of precise oscillation parameters for antineutrinos [11].

  NuMI beam is nowadays being used for the **NoνA** experiment, this time with an average neutrino momentum of 2 GeV/c on an off-axis beam. Its main objective will be putting hard constraints on mass hierarchy models and precisely estimating δ_{CP} [12].

- **CNGS** beam was built between 2000 and 2006 for usage in the **OPERA** experiment at Gran Sasso Laboratory and was used from 2006 to 2012 in the same experiment. Neutrinos are produced by 400 GeV/c protons fast extracted from the SPS beam and sent against a segmented graphite target [10]. Data gathered from the OPERA detector at Gran Sasso Laboratory has proven that the atmospheric oscillation happens through the appearance of ν_τs in a ν_μ beam by explicitly reconstructing the decays of τ leptons from charged current interactions [13]. Formerly only the disappearance of $\nu_m u$ had been studied.

1.3 The ENUBET project

1.3.1 Motivations

Neutrino cross-sections can be calculated from neutrino interactions experiments, however cross-section estimations remains challenging, both in theoretical computations, as PDF model of target nucleons must be taken into account, and in experimental measurements, as proper reconstruction can only be done for charged leptons and are otherwise very biased in their energy reconstructions. For all of this reasons, and on top of that the limited precision on neutrino fluxes ($\sim 10\%$), state-of-the-art measurements cannot achieve better than 30% agreement with experimental data for most inclusive, single, and double-differential cross-sections [14].

Currently, neutrino beam experiments are focused on four main objectives:

- **$\delta_{\mathbf{CP}}$ measurements:** indication of CP symmetry violations in neutrinos oscillation has been observed by the T2K collaboration [15], but strong constraints on δ_{CP} value are still missing. In a neutrino beamline experiment, the related observable is

$$A^{CP}_{\mu e} \equiv \frac{P(\nu_\mu \to \nu_e) - P(\overline{\nu}_\mu \to \overline{\nu}_e)}{P(\nu_\mu \to \nu_e) + P(\overline{\nu}_\mu \to \overline{\nu}_e)} \tag{1.23}$$

  and is related to δ_{CP}. Since beamline experiments can measure both $P(\nu_\mu \to \nu_e)$ and $P(\overline{\nu}_\mu \to \overline{\nu}_e)$, they are powerful tools to study CP violations. Hyper-Kamiokande is set to establish a first measurements of δ_{CP} [16].

- **Neutrino mass hierarchy determination:** neutrino mass ordering is still an open question in neutrino physics. To determine which hierarchy is the correct one, sign(Δm^2_{23}) is measured: for the Normal Hierarchy (NH), sign(Δm^2_{23}) $= +1$, for the Inverted Hierarchy (IH) sign(Δm^2_{23}) $= -1$. Neutrinos oscillation in vacuum depends on $\sin^2(\Delta m^2_{23})$ and are not dependent on sign(Δm^2_{23}), however neutrinos oscillations in matter are and thus it can be measured in long-baseline beamline experiments. DUNE and Hyper-Kamiokande are set to estimate sign(Δm^2_{23}).

- **Precise oscillation parameters estimations:** estimation of these parameters comes from neutrino events rate in experiments. Systematics errors are mainly due to three factors: detector efficiency, interaction cross-section and neutrino flux. In beamline experiments, ν_e and ν_μ fluxes are typically estimated from meson production, transport and decay simulations, and validated by external data; the uncertainties on such values depend on the production of mesons and their transport, that have non-negligible systematics, and for this reason neutrino fluxes uncertainties are usually on the order of 10-20% [17].

- **Probing the "sterile neutrino" hypothesis:** this theory proposes the existence of one or more neutrino flavor, so-called sterile, which does not interact via weak currents. The theory aims to explain the so called *reactor antineutrino anomaly*, a deficit in $\overline{\nu}_e$ counts from reactor based neutrino experiments with respect to theoretical predictions [18, 19]. Sterile neutrino theories predicts also the existence of a fourth neutrino mass eigenstate ν_4, thus a whole new set of parameters should be measured if this theory is proven true. Short baseline experiments at FNAL (ICARUS, SND, MicroBooNE) aim to find proofs of sterile neutrinos existence and eventually give a first measure of four neutrino theory oscillation parameters [20].

All those measurements require high precision experiment that can estimate those quantities with very high precision. The main contributions to the uncertainties in beamline experiments are mainly two: low statistic counts in neutrino interactions, and systematics cross-section uncertainties. Next generation experiments, such as DUNE and Hyper-Kamiokande, will employ very large detector masses and high neutrino fluxes beamlines, sharply reducing all statistical error contributions; systematics contributions due to cross-section uncertainties, particularly at GeV scale, are thus the main obstacle in precise oscillation parameters estimations [14].

Initial proposal for ENUBET aimed at tackling low precision in neutrino flux monitoring, producing a narrow-band neutrino beam whose electron neutrino flux is known with an unprecedented precision of 1%. During years of development, another big step forward was taken: ENUTAG beamline design was finalized, and its momentum selection for mesons was made via magnetic dipoles rather than magnetic horns. This means that the beamline can take long proton extraction bursts (up to seconds), reducing the instantaneous rate of charged leptons in the decay tunnel by several orders of magnitude; this allows for conventional detectors to be used for monitoring, lowering costs and allowing for granularity in detectors. The construction of an entire calorimeter instrumenting the decay tunnel was thus possible. Moreover, because of the long extraction cycles, integration of such apparatus with NuTag is also possible.

1.3.2 Beamline and instrumented decay tunnel

The ENUBET (Enhanced NeUtrino BEams from kaon Tagging) apparatus consist of a CNGS-like beam that transfers pions and kaons at 8.5 GeV/c momentum in a 40 m long decay tunnel. This design favors K_{e3} decays, i.e. $K^+ \rightarrow e^+\pi^0\nu_e$ in the decay tunnel, so that $\sim$ 97% of the total ν_e flux comes from K_{e3} decays; the decay tunnel calorimeter tags large angle ($\sim$ 100 mrad) e^+, which are directly liked to ν_e production and thus gives a precise neutrino count and flux estimation. Muons detectors beyond the hadron dump enables ENUTAG to detect large angle muons from $K_{2\mu}$ ($K^+ \rightarrow \mu^+\nu_\mu$), $K_{3\mu}$ ($K^+ \rightarrow \mu^+\pi^0\nu_\mu$) and π^+ decay ($\pi^+ \rightarrow \mu^+\nu_\mu$). Setup sketch of decay tunnel instrumentation is reported in Figure 1.5.

For a high precision cross-section measurements, ENUBET will be built as a Nar-

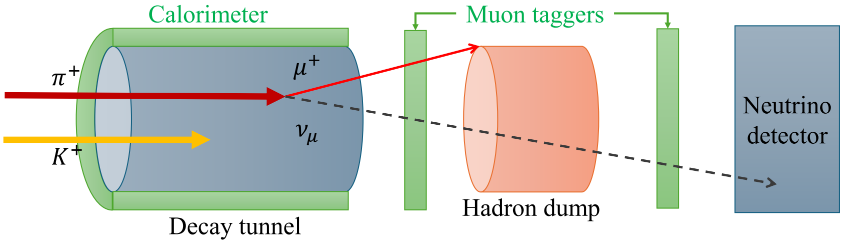

Figure 1.5: ENUTAG sketch. Main apparatuses are shown in green.

row Band Beam (NBB) experiment, in order to reduce mesons momentum spread and background noises; this allows accurate measurements on neutrino energy on an event-by-event basis via the Narrow Band Off-Axis (NBOA) techniques, that measure ν_μ energy from their incoming angle in the neutrino detector, and thus the distance from beam axis and point of interaction gives a precise indirect measure for neutrino energy [14]. This comes from the two-body kinematics of mesons decay, meaning that for a precise energy reconstruction a fine estimation of mesons momentum is needed; that explains the need for a NBB. In practice, this means that the downstream neutrino detector can be virtually subdivided in radial slices, each 20 cm thick and with its expected neutrino flux and energy distribution. Total and radial fluxes are graphed in Figure 1.6.

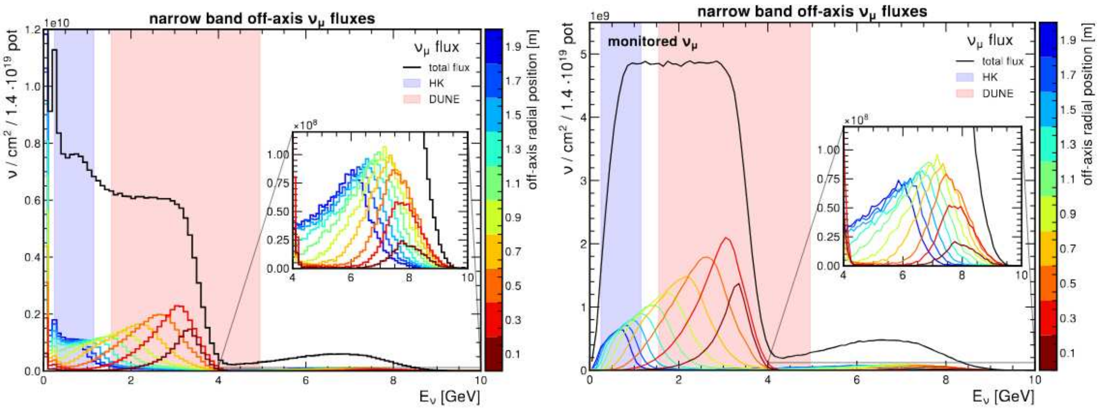

Figure 1.6: ν_μ narrow band off-axis fluxes at different radial distances on the detector surface. The black line shows the total flux and the colored lines the fluxes incident on different radial positions. Left graph shows the breakdown for all incoming neutrinos, right graph only for the monitored neutrinos. From [14]

.

Beamline setup is crucial for a precise momentum selection on mesons, so that NBOA is viable. ENUBET beamline presents seven different quadrupole, two double dipoles for momentum selection, and a series of tungsten collimators and drift, besides of course the proton target and the decay tunnel. The whole beamline schematics is reported in Figure 1.7; it also includes the NuTag spectrometers, that will be talked about in Subsection 1.3.4.

Decay tunnel instrumentation has been developed and studied for years; the final design is an iron/scintillator sampling calorimeter, comprised of 3×3 cm^2 section, 0.7 cm thick plastic scintillator interleaved with 1.5 cm thick iron plates arranged

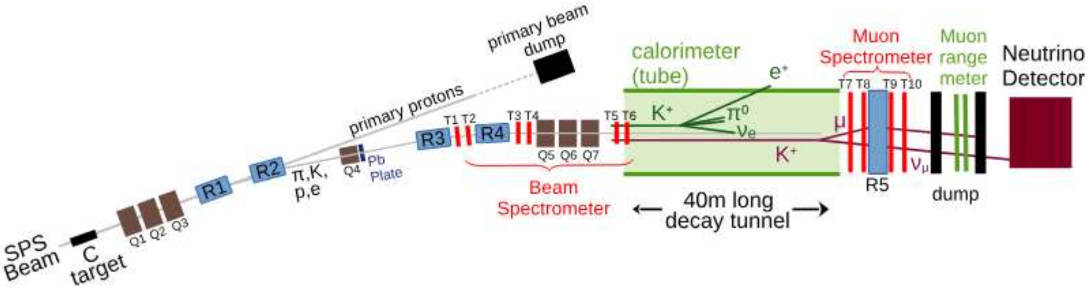

Figure 1.7: ENUBET beamline complete schematics. From [21].

in modules made of 5 scintillators and 5 iron plates each [22, 23]. The inner part of the decay tunnel is covered with another set of scintillators, placed perpendicularly with respect to the beam axis, and are used as a veto layer (called t_0 layer) to discriminate $e/\mu/\pi$ events from γ/π^0 events. Each module is read out by WLS fibers that carry the scintillating light to Silicon Photo-multipliers set in Geiger mode [22].

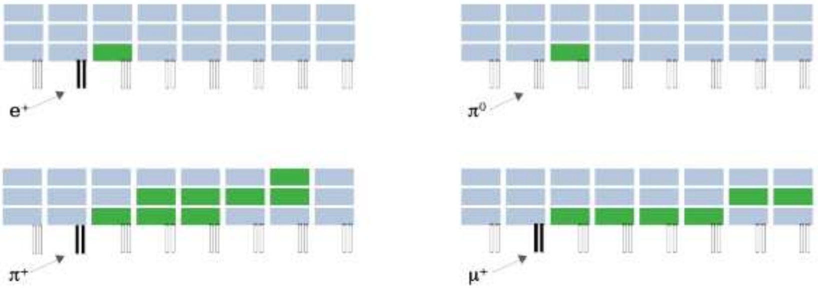

Figure 1.8: Event topologies for different particles. t_0 layer functionality is shown. From [22]

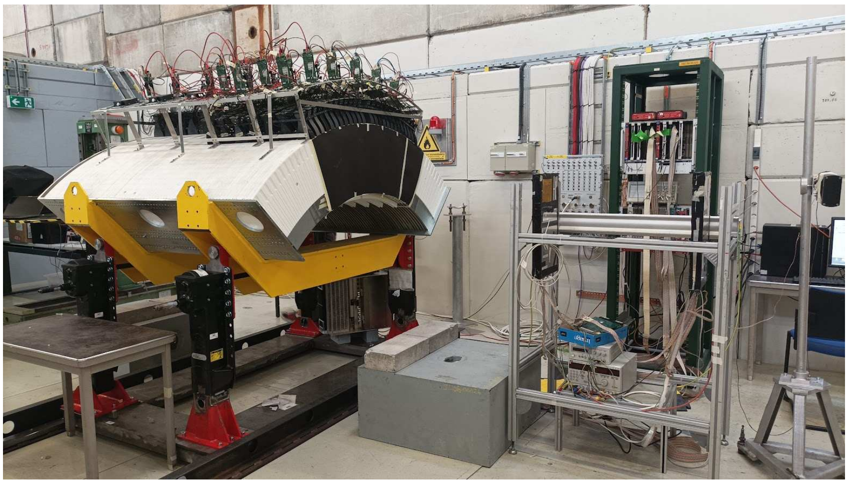

Figure 1.9: The ENUBET demonstrator (1.65 m length, 3.5 t mass). From [23].

1.3.3 Events tagging and background discrimination

Main focus of ENUBET will be K_{3e} event tagging, however that is not the only decay happening in the tunnel, as there is background signals coming mainly from $K \to \pi$ and muons decay. All signals and background decays events in ENUBET are reported in Table 1.5. Discrimination is possible thanks to tunnel instrumentation and calorimetric techniques.

Decay	**BR (%)**	**Type of signal**
$\pi^+ \to \mu^+\nu_\mu$	~ 100	muon stations (hadron dump)
$K^+ \to \mu^+\nu_\mu$	63.55	tagged in the tunnel
$K^+ \to \pi^+\pi^0$	20.66	background
$K^+ \to \pi^+\pi^+\pi^-$	5.59	background
$K^+ \to e^+\pi^0\nu_e$	5.07	tagged in the tunnel
$K^+ \to \mu^+\pi^0\nu_\mu$	3.35	tagged in the tunnel
$K^+ \to \pi^+\pi^0\pi^0$	1.76	background
$\mu^+ \to e^+\bar{\nu}_\mu\nu_e$	~ 100	background

Table 1.5: Signals and backgrounds in the ENUBET decay tunnel. From [22].

Event reconstruction is done via neural networks algorithms based on the TMVA toolkit [24]. Background discrimination via NN uses energy deposition, track isolation and topology data and allows to achieve a positron recognition efficiency of $\sim 22\%$ and an S/N ratio of ~ 2. For large angle muons, efficiency rises to $\sim 34\%$ and S/N to ~ 6 [25].

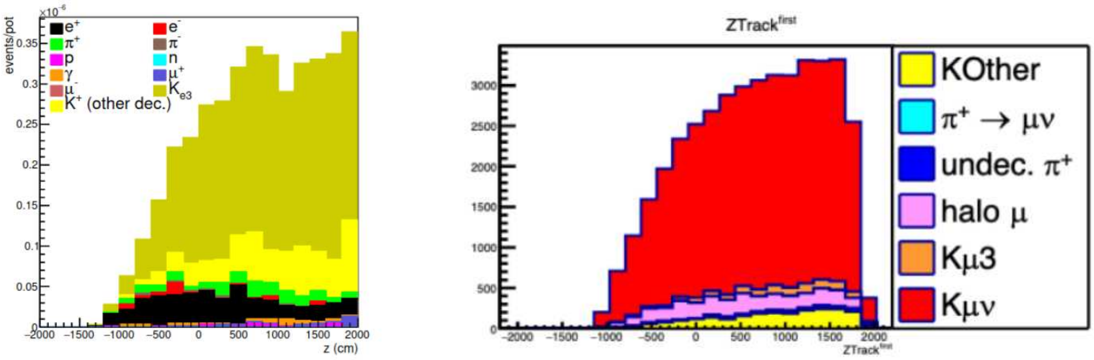

Figure 1.10: Example of signal identification after the NN discrimination: e^+ (left) and μ^+ (right) production in the decay tunnel. From [25].

1.3.4 NuTag integration

Neutrino tagging technique (NuTag) can be used to further improve reconstruction accuracy on neutrino events by directly measuring π, K momenta in the beamline. [26]. Measuring mesons momentum and position along the beamline, and combining those data with ENUTAG event reconstruction and neutrino data, it is possible to achieve a complete event reconstruction, and even select neutrino events based on mesons energy. Moreover, based on time and angular coincidence, each neutrino interacting in the detector could be associated with a single tagged neutrino [27].

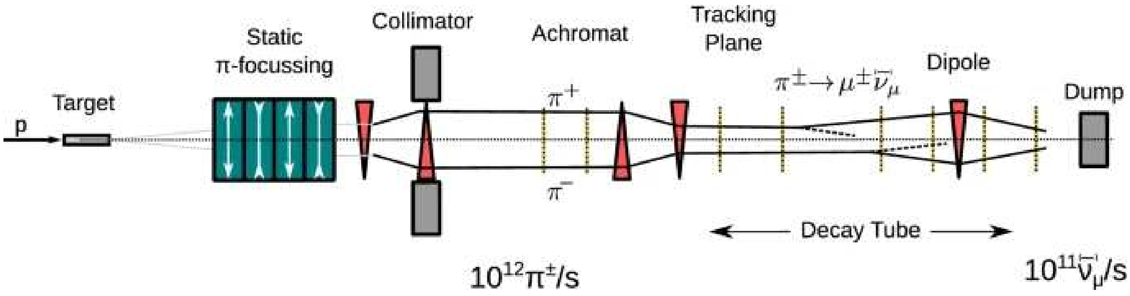

Figure 1.11: Hypothetical NuTag beamline setup. From [27].

NuTag is a system of mesons tracking in the beamline made of fast-tracking silicon detectors placed along particle trajectory. Such detectors are capable of tracking mesons or leptons produced by their decays, thus extending ENUBET's capabilities in two ways: firstly, lepton monitoring in NuTag can significantly improve neutrino flux estimations by increasing the number of monitored neutrinos and enhancing the spectral characterization of the flux, eliminating all neutrino flux estimations dependencies on MonteCarlo simulations; secondly, if the neutrino detector possesses sufficient time resolution (< 1 ns), each observed neutrino can be uniquely correlated with its parent meson and associated charged lepton. This operation mode is called *tagged neutrino beam*, and has been a long-standing goal in accelerator neutrino physics.

Chapter 2

Beamline simulation

The design of the ENUBET test beamline has been already tested on `bdsim`, a software based on Geant4 code. The main limitation of that implementation is the separation between particle production simulation at target, and subsequent particle evolution. The first part is handled, in `bdsim` code, using FLUKA, and then the produced event is used as input for the beamline simulation block. This does not allow for full event reconstruction, and so the link between a simulated meson and its generating proton-on-target event (PoT) is lost. In addition the implementation of the beamline in GEANT4 allows having an output where each neutrino is linked to its chain of parents. In this way this information can be used as an input to the framework that has been developed by the ENUBET collaboration to evaluate how lepton monitoring can reduce the systematic uncertainty on the flux.

For this reason, a whole reconstruction of the beamline design in a pure Geant4 code simulation has been done: the entire project has been transposed starting from `bdsim` code and saved parameters, and the whole beamline, from target to hadron dump and near neutrino detector, has been reconstructed and simulated in a single block in pure Geant4 code. While Geant4 has its cons and some approximations had to be done to transpose the code from `bdsim`, a clear advantage of pure Geant4 code was detector construction flexibility; this was used to simulate all external structures, such as shielding, concrete walls, and underground bedrock, as this kind of element implementation was not possible on `bdsim` due to software limitations. That allowed for a preliminary shielding study on the beamline, aiming at minimizing low energy neutrino components in the near detector placed at the end of the beamline.

2.1 Beamline design considerations

As already discussed in Subsection 1.3.2, the ENUBET beamline aims to produce pions and kaons at $p = 8.5$ GeV/c, with a 10% tolerance. Instead of employing magnetic horn for mesons focusing and selection, a system of magnetic dipoles and quadrupoles is tuned to select particles in the required momentum range; this technique is reminiscent of narrow bend beamlines used in the '70s, however modern proton accelerators fluxes can be leveraged to achieve a high particle rate. All data regarding protons, pions, mesons, and overall beamline performances, are reported in Table 2.1.

Parameter	**Value**
Primary proton momentum [GeV/c]	400
Beamline meson momentum [GeV/c]	max. 8.5
Proton-beam spill duration	slow (4.8 s to 9.6 s)
Spill intensity [protons/spill]	1×10^{13}
Event rate [THz]	$1 - 2$
Instantaneous power on target [W]	$170 - 340$
(K^+, π^+) yield per proton	$1.3 \times 10^{-3}, \ 1.9 \times 10^{-2}$
(K^+, π^+) rate [GHz]	2.7, 40
Annual proton intensity [protons/year]	$2.1–3.2 \times 10^{18}$
Total proton requirement	1.4×10^{19}

Table 2.1: Beamline parameters and specification. Meson yields and rates refer to the location at the beginning of the decay tunnel. From [14].

The beamline is optimized using a multi-objective genetic algorithm (MOGA) called TRANSPORT that can optimize 26 parameters in total: fo those 7 refers to drift lengths upstream and downstream of quadrupoles, 18 refers to quadrupoles lengths, apertures and field intensities, and 3 are for target length, density and angle with respect to the beamline [21]. Optimization has been done considering an output pion momentum of 8.5 GeV/c and a 10% tolerance [28]. All block parameters have been reported in their respective sections.

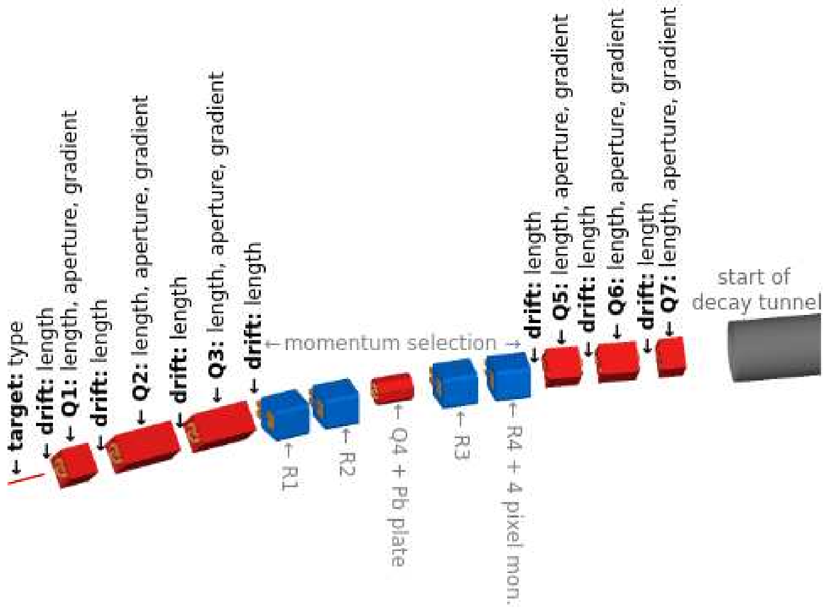

Figure 2.1: Beamline sketch with all component parameters.

Positron flux must also be reduced along the beamline, for two main reasons: to reduce signal frequency on NuTag silicon detector, keeping it under 100 MHz/mm^2, and to avoid e^+ noise in the decay tunnel that could compromise K_{e3} decays tagging. To reduce positrons traveling along the beamline, a small lead plate has been placed along the beamline. Positron fluxes and lead plate effects will be discussed in

Subsection 3.1.2.

2.2 Introduction to Geant4

`Geant4` is a is a free software package used in physics to simulate particle-matter interaction in a variety of situations. It provides the user of all the necessary tools to construct and simulate a system geometry, define its materials, and to define how particles interact with such geometry [29]. Using Geant4 users can construct stand-alone applications to simulate custom-made system; personalization can go as far as custom-made physics interactions, materials, and particles.

Geant4 is based on C++ object oriented programming: packages provide predefined base classes and functions from which the user can derive custom made classes; in this way is possible to maintain high customisability without compromising program runtime flow, defined by Geant4 hard-coded kernel. A type of classes, called Messengers, are dedicated to macro command handling, so that physical and simulation parameters can be changed during runtime by running Geant4 macro commands; in this way it is also possible to define custom macro commands.

Geant4 also supports ROOT data output, a functionality that has been extensively used during this project.

2.2.1 Main classes and functions

- **`main.cc`:** As the name suggest, this is the main source file. It is in this file that physics library is chosen, `runManager` is initialized and UI is called (if needed).

  The first thing the main function should do is call an instance of `G4RunManager`, which handles program flow and events loop. Detector construction, physics list and user defined actions are passed to the RunManager via `SetUserInitialization()` functions. Three classes must be called by the `main.cc` function: a *physics list*, a *detector constructor*, and a *particle gun*. Without those classes declarations a Geant4 program cannot work properly.

  Multithreading can be implemented for machines that supports it; number of threads is given by an external macro by the `/run/numberOfThreads` command. To handle program flow and events loop in multithread mode, `G4MTRunManager` has to be called instead of the regular RunManager, that works on a single thread. Attention is also needed when handling multithreading with `.root` file outputs, as the output from each thread would be different and file merging must be setup. Multi-thread has been implemented in this work to speed up simulation time.

  In this work a random seed generator was also implemented in the main function, to ensure simulation randomization; to provide a different seed at each run start, seed is set as system time, taken by `ctime` C++ library.

- **Physics list:** is on of the three mandatory user classes in Geant4 and must be defined for proper program execution. For this work `FTFP_BERT` has been used. `FTFP_BERT` is the recommended physics list for High Energy Physics as it contains all standard electro-magnetic processes, and can handle hadron-nucleon reactions using *Bertini cascade model* which is valid in the 100 MeV-10 GeV C.o.M. energy range. For higher energies, Fritiof Model is preferred [30]: this model assumes that only one or two quark-gluon strings are produced in elementary interactions; from this assumption, the model can handle elastic scatterings, binary reactions, diffractive events and baryon/anti-baryon annihilation up to $E_{CoM} = 1000$ GeV. For this work, $E_{CoM} \sim 95$ GeV for PoT events, thus proton-carbon interactions are modeled by Fritiof Model.

- `G4VUserDetectorConstruction`: is the class dedicated to physical definition of simulation objects, and the second mandatory class to define; the usual approach is to define a custom class that derives from it, and build the detector inside of this daughter class; this is how has been done in this work. All physical objects composing the beamline and detectors are then defined in the `Construct()` function.

  Each physical elements is defined in three steps:

  1. **Solid object:** shape and dimension of the object are firstly defined. To determine shape, so called Constructed Solid Geometry (CSG) primitives are called: for each shape, a different CSG class is usable, each defined by a minimal set of parameters. Using `G4UnionSolid` and `G4SubtractionSolid` is also possible to combine different solid classes to create custom made solids. A set of the most common CSG used in Geant4 is in Figure 2.2.
  2. **Logical object:** a `G4LogicalVolume` takes a physical volume and it applies a `G4Material` to it; materials can be user defined or imported from standard Geant4 libraries. In the object is a field volume or a detector, this is the stage at which such attributes are added. Logical level is also accessed from external macro for cosmetic options (e.g. color).
  3. **Physical volume:** the `G4PVPlacement` functions defines a `G4PhysicalVolume` from a logical object. In this phase, coordinates and rotation of the object are defined for the final placing in the world block.

  The most important block in detector construction is the `world` block, defined following the three steps reported above; this volume will contain all other defined blocks, so common practice is defining it as a very big vacuum cube; this has been done for this work too. To handle multi-threading, all magnetic fields and detector volumes have been declared and assigned to logical volumes in a predefined function called `ConstructSDandField()`, from `G4VUserDetectorConstruction`.

  To streamline beamline modelisation, a function oriented approach has been used for complex objects (quadrupoles, dipoles, collimators): for each kind of element a function has been defined, that takes as input an index that identifies the single elements and selects appropriate parameters from a list; then, the volumes definition takes place.

- `G4UserPrimaryGeneratorAction`: this is the last of the three mandatory classes. It generates the so called ParticleGun, used to simulate sources behavior. In this work two different ParticleGun have been used: a proton gun placed before the graphite, used to simulate incoming protons from SPS, and a π^+ gun placed after the graphite rod, used for dipole and quadrupole testing. Parameters for both guns are reported in Table 2.2. To switch between

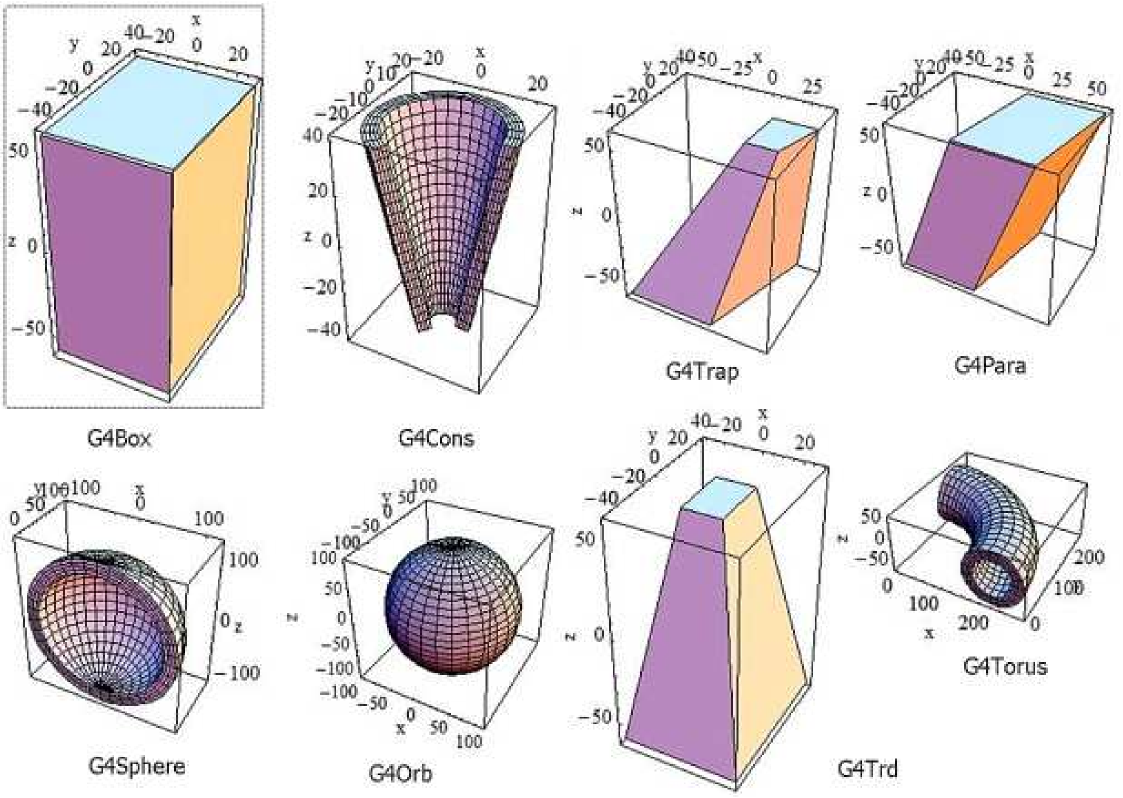

Figure 2.2: Representation of 8 of the most commonly used CSG in Geant4, alogn with their coordinate system of reference. From [31].

them a Messenger has been added, used to read the custom macro command `/ENUTAG/testMode`. This approach was useful for simulation debugging, since enabled to separate testings for particle production and propagation.

Gun	Part. energy [GeV]	Starting coord. [m]	Direction [mrad]
Proton	400	$(-0.65, 0, 0)$	8.726
π^+ test	8.5	$(+0.65, 0, 0)$	8.726

Table 2.2: ParticleGun parameters

- `G4VUserActionInitialisation`: default behavior for this class is not given, and instead user redefinition is mandatory. This class handles user defined event generators and actions.
- `G4VAnalysisManager`: handles data acquisition and saving. It is a singleton, which means that there is only one of this object per program start; its initialization is required for most of user-defined classes.
- `G4UserRunAction`: this class handles run start and end. For the scope of this project, this meant mainly ROOT file handling, creating a output file at run start and closing it at run end. ROOT file structure and data writing will be discussed in Subsection 2.5.
- `G4UserEventAction:` handles single events during runtime. For the scope of this project, it has only been used to produce a bash output with current

running event number, to keep track during runtime.

- `G4UserSteppingAction:` handles single particle steps options. In Geant4 a step is defined as a segment that carries “delta” information of the tracked particle (energy loss on the step, time-of-flight spent by the step, etc.) and of the start and end points, so that volume and material of passing are also known. It is also possible to track the transition of the particle between two volumes, a property exploited in detector simulation. Geant4 has methods to optimize step length, in order to reduce computational time; minimal step length is set at 1 mm, however user can redefine such parameter. User can also define extra condition for track killing via the `track -> SetTrackStatus(fStopAndKill)` method: if a required condition is met during stepping action, the track is killed and does not propagate further, which also means its data is canceled from memory; this can be used to reduce output file dimension and eliminate useless data. In this work, track killing has been imposed for particles that reach kinetic energy lower than 50 MeV, and also all neutron, antineutrons and photons are killed at first step, as they are not of interest for our analysis and their data only contributes to output file bloat.
- **Messengers:** those are user defined classes used to interface the source code with macro commands. In this work they have been used just for utilities (testing mode, output file naming, etc.).

2.2.2 Particle propagation

To understand properly how this simulation works, it is important to see how the program handles particle propagation. Geant4 is capable of describing and propagating particle in all kinds of electromagnetic, gravitational and user-defined fields. In order to propagate, the particle equation of motion is integrated, using one of many available Runge-Kutta based methods for ordinary differential equations; default method is a fourth-order Runge-Kutta, but more can be used for different kinds of field, depending on their regularity: for less smooth fields, a lower order stepper should be preferred. In case of very simple fields (e.g. uniform electric/-magnetic fields) analytical solutions are computed.

After calculating the particle trajectory, its curved path is segmented in a series of chords segments that closely approximate the trajectory. The chords are the used to determine whether the track has crossed a volume boundary [29]. How closely the set of chords approximate the curved track is determined by five parameters:

- δ_{miss} (also referred to as *miss distance*) is the maximum acceptable value for the sagitta, which is the distance between the real curved trajectory and the calculated chord. Tuning this parameters means tuning the precision of volume hitting. It is the most important parameter to minimize, however making it too small becomes very taxing for CPU computation.
- δ_{int} is the maximum distance allowed between the real intersection point of the track with a volume boundary and the chord intersection point with same boundary. If such distance is higher than the set parameter, chords are recalculated accordingly.
- $\delta_{OneChord}$ is the maximum accepted distance between real track endpoint and

chord endpoint. It refers only to steps completely contained in one logical volume.

- ε_{min} and ε_{Max} are two parameters that define the maximum accepted error on $\Delta p/p$ and $\Delta x/x$ for each step. ε_{Max} is referred to for large steps, while ε_{min} is the minimum value.

Geant4 thus splits each trajectory in chord of various lengths, chosen in such a way that the chord sagitta is always smaller than δ_{miss}, the error on the endpoint us always smaller than $\delta_{OneChord}$, and each volume boundary boxing has an error lower than $\delta_{OneChord}$. For the scope of this work, all parameters values are Geant4 standard values, reported in Table 2.3.

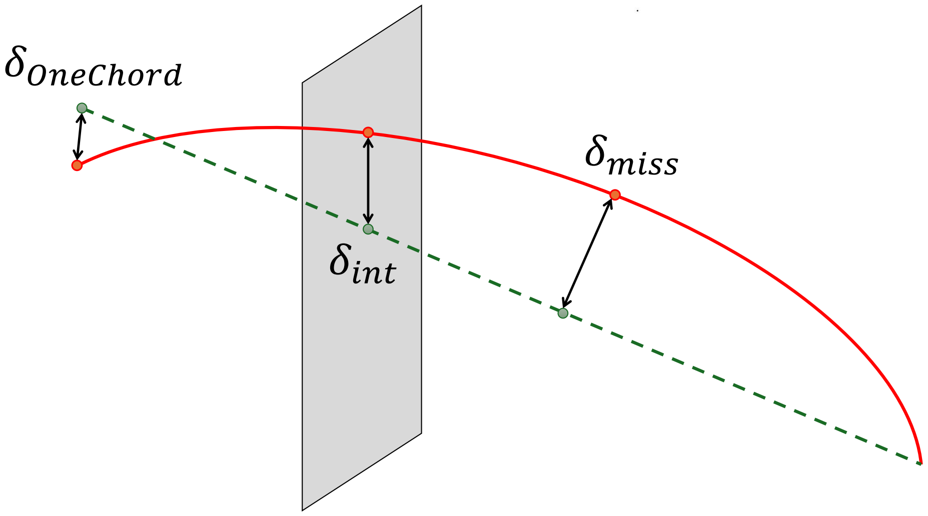

Figure 2.3: Recap of δ integration parameters.

Parameter	Default value
δ_{miss}	0.25 mm
δ_{int}	10 μm
$\delta_{OneChord}$	10 μm
ε_{Max}	0.01
ε_{min}	$5 \cdot 10^{-5}$

Table 2.3: Default Geant4 stepping parameters.

A step can be a union of more chords, and it is taken as the minimum element on which Geant4 computes physical interactions. Each step has two points, the `PreStepPoint`, which is the starting step point, and the `PostStepPoint`, which is the ending point; each point stores information about its containing volume, in particular its material. In case of a step that ends at a volume boundary, the `PostStepPoint` is placed on the boundary but is logically associated to the next volume: this is important because it allows the single step to gather information on both volumes, allowing Geant4 to simulate boundary processes (e.g. transition radiation). Each step also stores so called *delta* information of the particle, e.g. energy loss along step, time-of-flight, etc. [29, 32].

As already said, step stage is the one at which physics events are simulated. Each particle has its list of possible events to simulate, that can have one or more of the following attributes:

- `AtRest`: those events can happen if the particle is at rest, i.e. kinetic energy is at zero.
- `AlongStep`: continuous processes that are simulated along the step.
- `PostStep`: processes simulated at `PostStepPoint`. Also called discrete processes.

In case of competition between events, the one with the shortest proposed (i.e. randomly generated) path length is chosen. This does not apply for `AlongStep` events, as they all happen at the same time and are cumulative.

To move a particle, the `G4SteppingManager` method `Stepping()` is invoked; its algorithm produce a step for the particle of interest and it updates its trajectory. `Stepping()` algorithm must follow a series of action:

1. Check if particle kinetic energy is zero. If so, invoke an `AtRest` event.
2. Estimate step length from processes information.
3. Check distance from nearest boundary. If is less than step length, update step length.
4. Apply all `AlongStep` processes and update the kinetic energy.
5. Apply `PostStep` and check if the event terminated the trajectory.
6. Update trajectory and go to next step.

2.2.3 From BDSIM to Geant4

`bdsim` is a software that builds upon Geant4 toolkit to easily construct and simulate particle beamlines and accelerators. Its packages contains predefined beamline modules schematics that can be imported in the program, needing only few parameters to be defined (e.g. length, aperture size, etc.).

Beamline modelization had been already done in `bdsim`, however there were some limitations due to how `bdsim` beamline model is setup. In particular, there was no way of tracking each neutrino up to its original PoT event, thus a complete conversion in pure Geant4 code has been decided.

There are some key differences between `bdsim` and Geant4 that defined work approach on this project:

- **Coordinate system:** Geant4 is based on standard cartesian coordinates, with the frame of reference usually centered at `world` center. On the other hand, `bdsim` implements a particular set of coordinates called *curvilinear coordinates* in which, instead of x axis, the s axis is defined, which follows the main beamline along its curves, and thus is not a linear axis. While this is more convenient for beamline construction, as the program just needs the module sequence from source to end, it can be tricky to insert shielding and other objects outside the pipeline; in such cases, one can take a beamline module as a coordinate reference.

In this work, to adapt from `bdsim` placement, a *parametric approach* has been used for module coordinate calculations: all blocks parameters have been declared before CSG declarations, and those parameters where used to calculate modules coordinate placements, in such a way that a beamline object coordinates depend on the previous inline block coordinates and current block dimensions. For inline elements, that meant placing taking the previous beamline element coordinates as reference, while for external elements (concrete, shielding, soil blocks) inline elements have been used as coordinate and dimension references; this gives the code flexibility, making easy to modify, add or remove inline elements, as all other object move accordingly without user intervention.

- **Modules definition:** `bdsim` pre-saved are quite detailed in their composition; for example, in a `bdsim` quadrupole both the external steel casing and copper wire coils are modeled, in order to come as close as possible to the real life counterpart. Such level of detail was not achievable in `Geant4`, as there are no such pre-saved element libraries, and instead everything has been modeled "by hand". Each element is an approximation of the real, physical elements present in the beamline; to give an idea, the same quadrupole has been approximated by only a holed steel cylinder and the generated quadrupole field. For the scope of this work, those approximations were more than enough to study particle production and transport. Every beamline block modeling will be discussed in detail in its own section.

First ENUBET beamline model was made in `bdsim` [14], and overall performances were already tested in this model. However, as already said at beginning of this chapter, `bdsim` limited what structures could be implemented properly, and thus the whole model was transferred in pure Geant4 code for further analysis and shielding tests.

2.3 Beamline modeling

The main focus of this work was transposing the ENUTAG beamline project from the `bdsim` code in Geant4 as closely as possible. As already discussed, due to software and time limitations blocks definitions lacks the detailing of `bdsim` predefined blocks, but it is unimportant for this work main focus. Each simulated beamline component will be discussed in its own section. The final result is reported in Figure 2.4 and 2.5.

Each element implementation will now be discussed in details.

2.3.1 Target

ENUBET target design is inspired by CNGS target, since both targets are designed to receive a constant flux of 400 GeV protons. TRANSPORT algorithms have been used to optimize this block too, and thus the final prototype is a 1.3 m long cylindrical rod of graphite, 6 mm in diameter; the estimated graphite optimized density of 2.26 g/cm^3 was considered too high to be achievable, and thus reduced to a more realistic 1.85 g/cm^3. To optimize pion production, the graphite rod is at a small angle with respect to the ENUTAG beamline axis, $\theta_{trg} = 8.726$ mrad. Incident proton beam is in axis with the target.

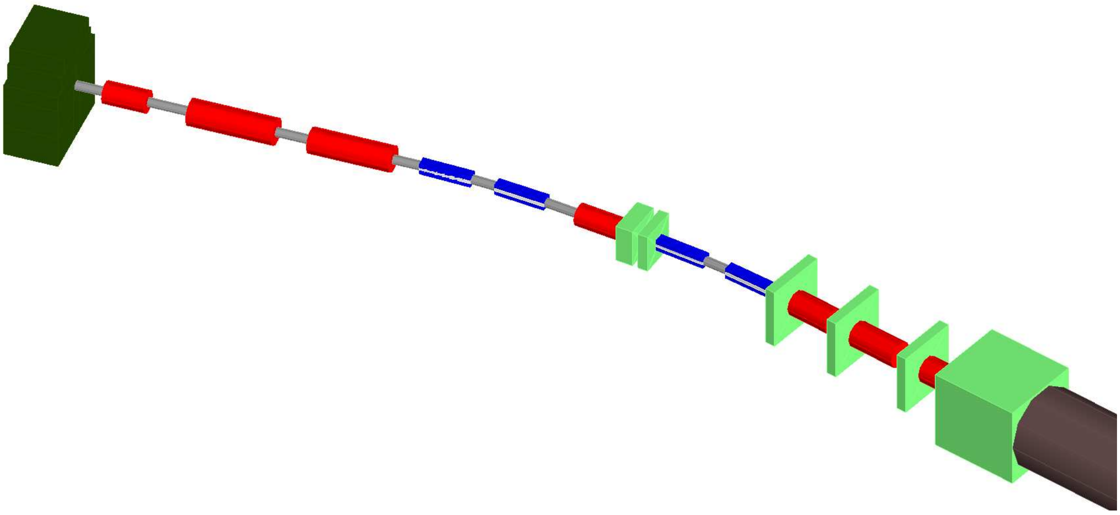

Figure 2.4: ENUBET beamline model in Geant4. Recognizable elements in this schematics are: target shielding (dark green); all beamline elements, dipoles (blue), quadrupoles (red), drift pipes (light gray) and collimators (light green).

Figure 2.5: Wide view on ENUBET beamline. ENUBET decay tunnel (brown) and hadron dump (shades of gray) are visible in the right side; part of the concrete casing (dark gray) is also present.

2.3.2 Dipoles

ENUBET beamline has two magnetic dipoles that are used for momentum selection on particles. Each dipole in actually two smaller dipole segments connected by a drift tube, each measuring 1.25 m in length (along s) and with a rectangular opening of dimensions 25×8 cm; the drift tube in-between the two dipole is 60 cm for the first dipole, 61 cm for the second, both at 24 cm of diameter. In Geant4 modelization, each dipole segment is made of three `G4Tubs` segments, covering an arch of $4.5045°$ degrees each: the middle one is vacuum and is the magnetic field volume, while the upper and lower ones are 20 cm thick copper plates that functions as placeholders for the dipoles wire coils. All dipoles parameters are reported in Table 2.4. Each dipole block introduce a deviation of $\theta = 9.09°$ in the beam axis.

Magnetic dipole field strength has been recomputed for the scope of this work, starting from what was known about dipole dimensions and particle momentum requirements. Pions curvature radius has been calculated from $\ell = R\theta$, with ℓ the dipole segment length of 1.25 m; this gives a curvature radius of $\rho = 15.90$ m. To then calculate $|B|$ the following formula can be used:

$$|B|\ [\mathrm{T}] = \frac{p\ [\mathrm{GeV}]}{0.3 \cdot \rho\ [\mathrm{m}]} = 1.799\ \mathrm{T} \tag{2.1}$$

and then $\vec{B} = |B|\hat{u}_y$.

Length [m]	**Width [cm]**	**Aper. height [cm]**	**|B| [T]**	**Angle [°]**	**Curv. radius [m]**
1.25	25	8	1.799	4.545	15.90

Table 2.4: Dipole segment parameters

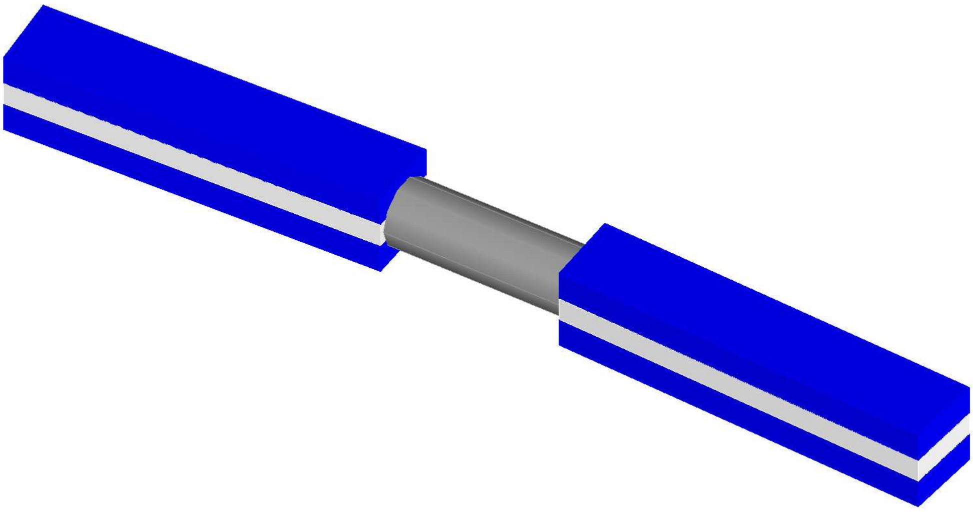

Figure 2.6: Dipole schematics in Geant4.

2.3.3 Quadrupoles

Magnetic quadrupoles on ENUBET are designed to focus positively charged particles, in order to improve beamline performances. In Geant4, each has been modeled as a hollowed steel cylinder that approximates for quadrupole outside shell and wire coils, and a vacuum-filled cylinder, in which particles travel and the quadrupole magnetic field is applied. Each quadrupole has been defined with its own parameter, all reported in Table 2.5. All quadrupole steel casings are 22 cm thick, a value estimated from `bdsim` models. In order, from upstream to the decay tunnel, quadrupoles ids are: 1, 2, 3, 5, 6, 8, 9.

All quadrupole magnetic fields have been implemented using the `G4QuadrupoleMagField` method, that automatically defines a quadrupole magnetic field given the magnetic gradient $\frac{dB_y}{dx}$ and the volume reference. However, `bdsim` defines quadrupole field strength using as parameter the *field strength* k_2, defined as

$$k_2 = \frac{1}{R}\frac{dB_y}{dx} \tag{2.2}$$

where $R = B\rho$ is magnetic rigidity of particles of interest and has unit of measure m^{-2}. Calculations yields

$$R\ [\mathrm{Tm}] = B\rho = \frac{p}{q} \simeq 3.3356 \cdot pc\ [\mathrm{GeV}] \tag{2.3}$$

if $q = e$ [33]. For 8.5 GeV pions it results $R = 28.3526$ T·m. All quadrupole fields parameters, both k_2 and $\frac{dB_y}{dx}$, are reported in Table 2.5. A positive k_2 sign indicates horizontal focusing quadrupole, negative is for vertical focusing.

ID	**Aperture radius [cm]**	**Length [m]**	$\mathbf{k_2}$ **[m^{-2}]**	**Field gradient [T/m]**
1	5.173	1.027721	-0.692447	-19.63267
2	10.499	2.063079	0.311347	8.82750
3	9.53	1.976843	-0.194342	-5.51010
5	5	1.2	0.639267	18.12488
6	9.12	1.080413	0.458804	13.0083
8	10.049	1.240500	-0.419312	-11.88859
9	10.476	0.800253	0.305695	8.66725

Table 2.5: Quadrupoles parameters.

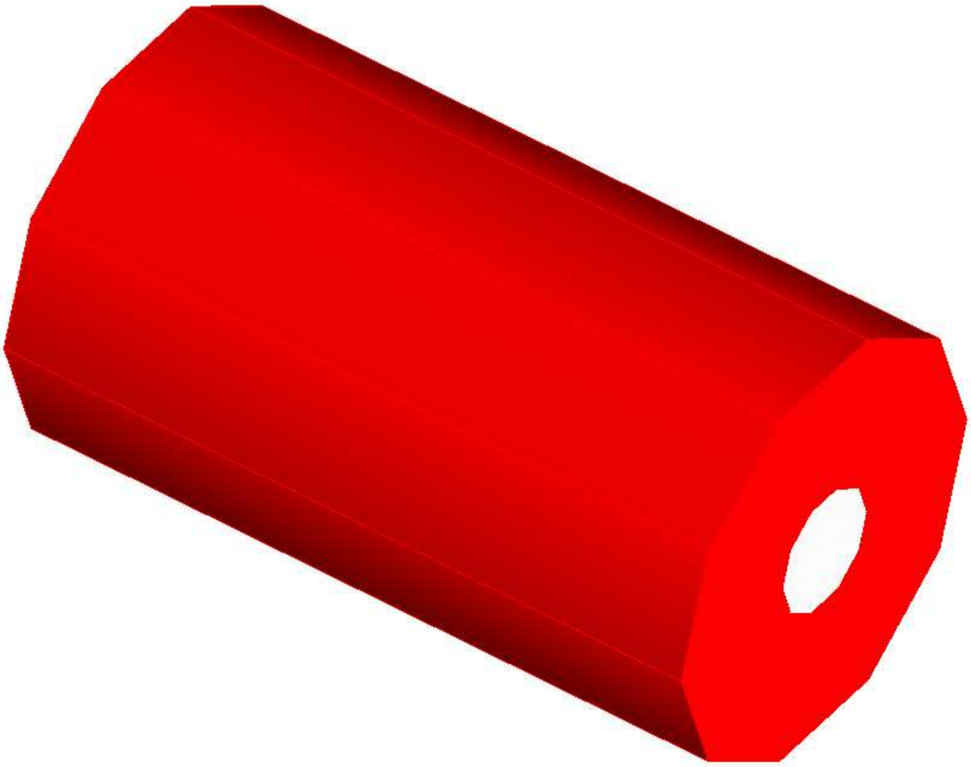

Figure 2.7: Quadrupole model in Geant4 simulation.

2.3.4 Collimators

Elliptical collimators (EC for short) are placed along the beamline to further focus particles in the beamline, absorbing particles traveling too far away from beamline axis. They are also designed to function as shielding, in order to reduce outgoing particles that could produce background noise in a near detector.

Each collimator is constructed as a `G4Box` parallelepiped with square side perpendicular to beamline axis; the hole is a `G4EllipticalTube` removed using the `G4SubtractionSolid`. Each collimator is labeled from 1 to 6 depending on its beamline position (1 is first from target, 6 is last) and has its measures, reported in Table 2.6. All collimators are made out of tungsten. Collimator images are reported in Figure 2.8.

Collimator	**Thickness [m]**	**Side length [m]**	**Hole width [mm]**	**Hole height [mm]**
EC1	0.45	0.98	90	100
EC2	0.25	0.98	100	100
EC3	0.25	1.55	100	100
EC4	0.25	1.55	100	100
EC5	0.25	1.55	100	100
EC6	2.20	2.04	130	110

Table 2.6: Collimators parameters.

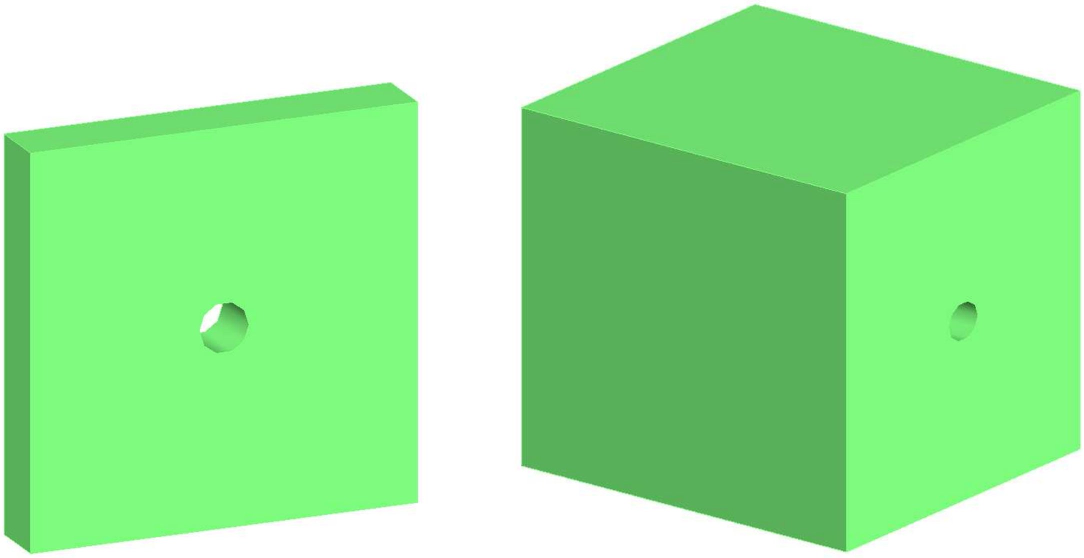

Figure 2.8: EC3 (left) and EC6 (right) schematics as they appear in Geant4 simulation.

2.3.5 Decay tunnel

Decay tunnel is the last beamline element, in which mesons decay into neutrinos. It is a 40 meter long, 2 meter wide cylindrical tube kept at vacuum conditions. To monitor particle budget at entrance and end of the tunnel during simulation, two virtual detector (DSVD 1 and 2) have been put at entrance and exit of the tunnel, covering the whole section.

To close the decay tunnel, a hadron dump is placed at the end of the beamline, 2.5 m from the end of the decay tunnel. It is a cylinder 3 m long and 2.4 m in diameter, made of three different material layers: a 40 cm diameter inner graphite core, a 60 cm middle layer made of aluminum, and an outer steel shell 40 cm thick. Its design is reported in Figure 2.9.

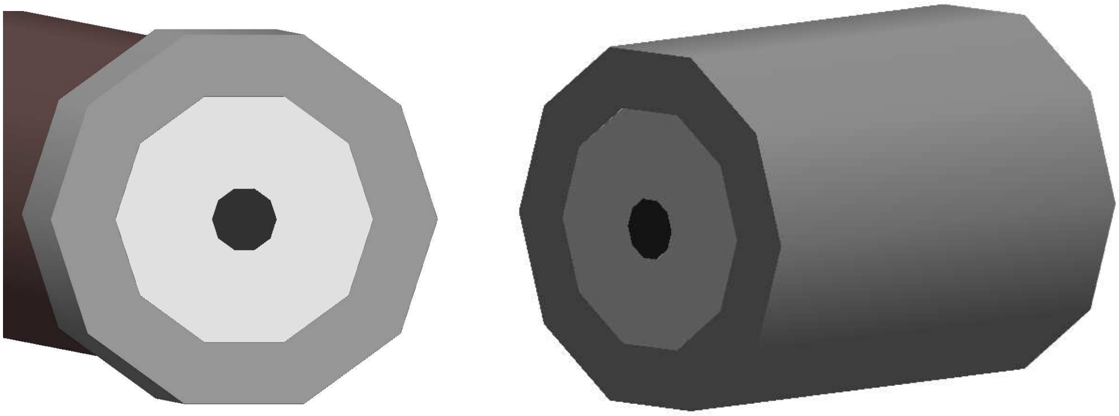

Figure 2.9: Front (left) and side (right) view of the hadron dump.

2.3.6 Outer elements

To properly simulate particle behavior, outside elements like shielding blocks, concrete structures and underground rock have been simulated. Shielding analysis and optimizations are one of the main focus of this work and thus will be discussed in depth in Section 3.2.

A concrete layer has been build all around the target structure and the beamline to simulate all facility structures. Concrete definition has been taken from the Geant4 material library; its composition and relevant quantities are reported in Table 2.7. For the target room, blueprint taken from [34] (reported in Figure 3.14) has been used as reference; the final design is reported in Figure 2.11 and is made of two main blocks: a `G4UnionSolid` made of a `G4Box` of dimensions $1.3 \times 0.5 \times 2.25$ m and a `G4Tubs` 2.25 m thick for the upper round roof; and a 70 cm thick, 5.75 m circular concrete wall, cut out near its center using the `G4SubtractionSolid` method to accommodate for the tungsten cap mentioned before.

Concrete along the beamline is made of a series of blocks, either `G4Box` for the line segments or `G4Tubs` for dipole sections, that makes up roof, floor and walls, all maintained at a constant thickness along the whole line up to the last region, where the last three quadrupoles and EC6 are accommodates. In this section walls are made thinner, in order to accommodate for EC6 large dimensions. All concrete measures for both sections are reported in Figure 2.10. Concrete definition was taken from Geant4 standard libraries.

Bedrock present around the whole structure has also been simulated. Since ENUBET will be tested at CERN facilities, bedrock material definition is based on swiss alpine molasses. Molasses is a sedimentary rock made of conglomerates and sandstones typical of mountain-side basins like the Geneva region. Because of CERN underground constructions and operations, plenty of data has been acquired on the geological and chemical composition of this rock; as reference for this work [35]

Element	Mass Percentage (%)
Hydrogen	1.000
Carbon	0.100
Oxygen	52.911
Sodium	1.600
Magnesium	0.200
Aluminum	3.387
Silicon	33.702
Potassium	1.300
Calcium	4.400
Iron	1.400

Table 2.7: Composition of G4_CONCRETE (Density: 2.3 g/cm^3).

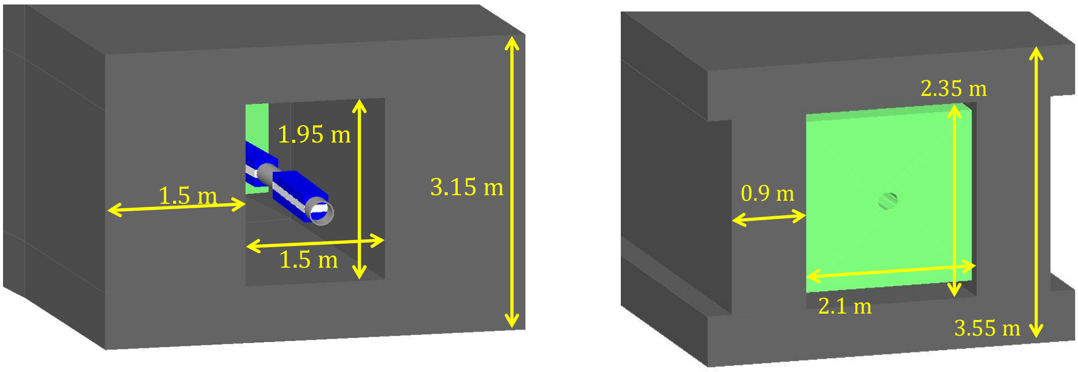

Figure 2.10: Concrete structure measurements. Left is encasing structure up to second dipole, right is the structure that confines the last quadrupoles section.

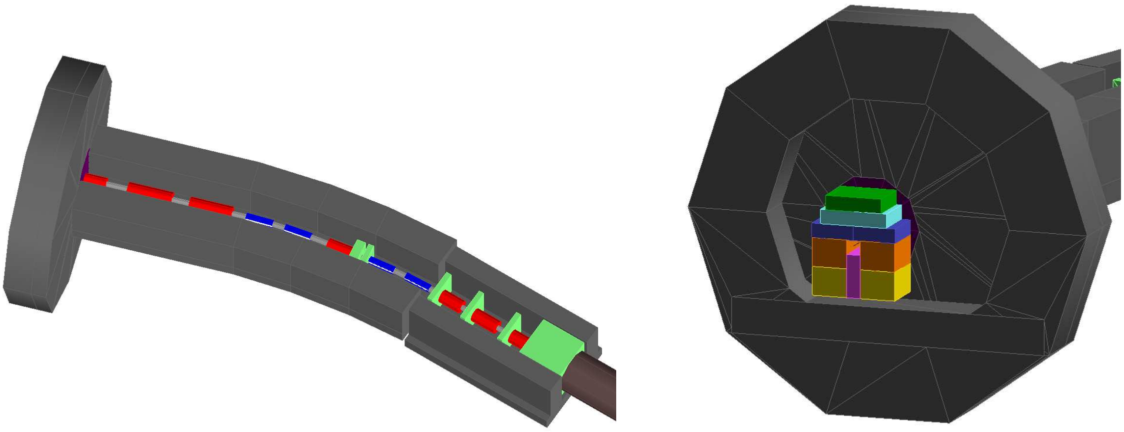

Figure 2.11: Left: concrete structure (dark grey) around the ENUBET beamline. Right: detail of target concrete room.

was used: in this analysis bedrock chemical composition has been studied using X-ray fluorescence spectroscopy (XRF) at four different depths to compute chemical composition and via Inductively coupled plasma mass spectrometry (ICP-MS) to assess rare materials (Ni, Cr) concentrations; the latter analysis is not of interest for the scope of this work. XRF results are reported in Figure 2.12. It also of notice that molasses density does vary with depths, as shown in Figure 2.13; that is an important data to take into account for the material definition in Geant4.

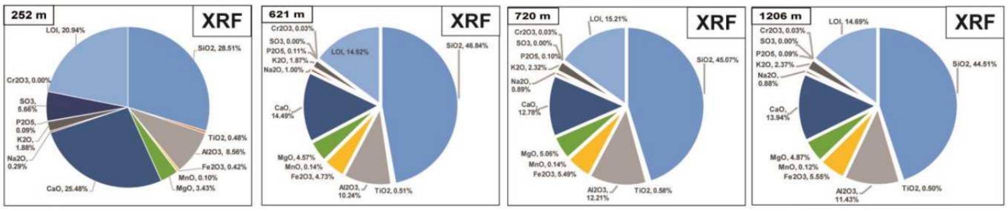

Figure 2.12: XRF analysis results for rock samples taken at 4 different depths. LOI refers to Loss On Ignition material. From [35].

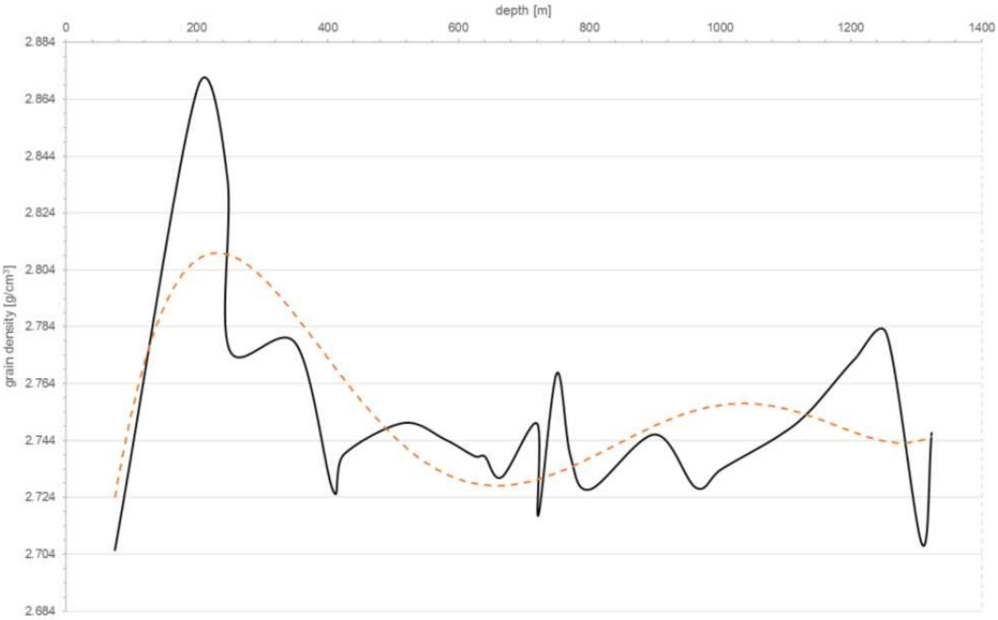

Figure 2.13: Density data points (black line) and trends (orange dotted lines) for molasses density, as a function of depth. From [35].

Beamline depth was assumed at $\sim$ 250 m, and from above data the estimated density at this depth is $\rho = 2.87$ g/cm^3. For the chemical composition the XFR taken for the 252 m depth sample has been taken, re-normalizing mass percentages to account for LOI (Loss On Ignition) material and for chemical compounds present in traces ($\lesssim 1\%$ mass percentage), which have been ignored for material definition. XFR data and final Geant4 mass percentages are reported in Table 2.8.

In total 16 different soil blocks has been defined to completely cover the whole beamline and decay tunnel, and to simulate soil between the hadron dump and the near neutrino detector. On average, soil blocks thickness around beamline, starting from where concrete ends, is $\sim$ 15 m. Soil thickness between hadron dump and neutrino detector is 8.25 m.

Compound	Real mass perc. (%)	Geant4 mass perc. (%)
SiO_2	28.51	38.79
CaO	25.48	34.66
Al_2O_3	8.56	11.64
SO_3	5.66	7.70
MgO	3.43	4.67
K_2O	1.88	2.56
Others	5.54	—
LOI	20.94	—

Table 2.8: Comparison of compound mass percentages from [35] and the Geant4 simulation (transposed).

2.4 Detectors simulation

Sensitive detectors are placed along the beamline to gather data about passing particles. Detector simulation is handled by `G4VSensitiveDetector` class, which is user defined; this allows user to save just the data of interest. Each detector is defined as a separate logical block, and at each of those logical volume an instance of the custom `G4VSensitiveDetector` class is implemented; all detectors assignments are handled in the `ConstructSDandField()` method in the detector constructor.

When a physical step intersect a detector, `G4VHit` class is called to handle detector hit and output all step data; hits calling is handled by `G4VSensitiveDetector` class. Alternatively, detector collision and data gathering can be handled directly by the `G4VStep` function. For this work, the former approach has been used, in order to improve performances. All exact positions of all detectors, as a function of s as defined in `bdsim`, are reported in Table 2.9 and Figure 2.14.

To streamline detectors placing, their thickness has been kept equal at $\Delta s = 1$ mm, the expected thickness of NuTag detectors; since virtual detectors are made out of vacuum and thus do not influence particles evolution, their thickness is an unimportant parameters that can be set at will.

2.4.1 NuTag detectors

Five silicon detectors are placed in the last part of the beamline; those are placeholders for the real NuTag inline detectors. They are a simple disk of pure silicon, 1 mm thick and 10 cm of radius, the same as the drift tube containing it, in order to track the whole particle flux in the beamline.

Since they are made of a dense material, they may impact particle evolution. Pion interaction length is $\lambda_\pi = 59.14$ cm $\gg \Delta s$, so their impact on particle fluxes is irrelevant. Deposited energy dE is saved as useful data in output root file, and is in the order of ~ 0.1 MeV $\ll 8.5$ GeV, thus energy loss in those detectors is irrelevant in final meson energy calculations.

2.4.2 Virtual detectors

Data gathered in NuTag detector was not enough for the scope of this analysis; in particular, they were not placed near points of interest, like the target or the

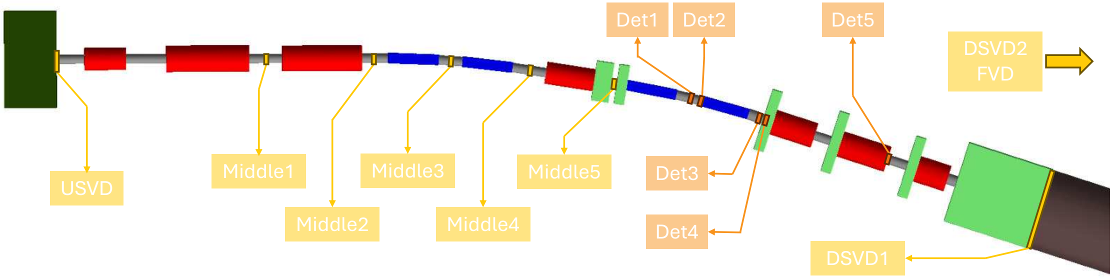

Figure 2.14: Detectors placement along beamline.

Detector name	s [m]
USVD	1.500
Middle1	6.711
Middle2	9.432
Middle3	11.313
Middle4	12.990
Middle5	15.139
Det1	17.071
Det2	17.321
Det3	18.821
Det4	19.096
Det5	23.785
DSVD1	26.235
DSVD2	66.235
FVD	91.235

Table 2.9: Positions of detectors along the beamline, expressed in s coordinates.

entrance of the decay tunnel. To compensate, a series of virtual detectors have been placed along the beamline; their position in the beamline is reported in Figure 2.14.

Each kind of virtual detector is named differently depending on its position:

- USVD (Up-Stream Virtual Detector) is placed directly on the target tip towards the beamline; it has same dimensions of NuTag detectors, and is used to monitor particle production at target.
- Middle (1 to 5) also the same dimensions of NuTag detectors, and are placed in the region between target and second dipole. They are used to monitor particle evolution, in particular to study dipoles particle selection and positron cut due to lead plating (Subsection 3.1.2). Their positions are reported in Figure 2.14.
- DSVD (Down-Stream Virtual Detector) 1 and 2 are placed respectively at the entrance and at the end of the decay tunnel. They are used to monitor particle budget in the decay tunnel, and final pions and kaons yields. To cover the whole tunnel section, theirs radius has been increased to 1 m.
- FVD (Far Virtual Detector) is placed 25 m after decay tunnel end, and is a placeholder for a near neutrino detector.

Those detectors will not be present in the real beamline, so to avoid unwanted interactions or energy losses with those detectors, theirs material is set as *vacuum*.

ENUTAG beamline should send neutrinos towards a near neutrino detector; design of such detector is not of interest for this work, so a detailed modelization is not needed. Neutrino flux received by such detector, along with background noise due to neutrino produced outside the decay tunnel, and an estimation of its ideal position, are instead all data of interest for this work, and they can be estimated using a very simple and minimalist implementation of such detector; in particular, neutrino background from production at target can be used as a metric for shielding efficiency, as will be discussed in Section 3.2. Final implementation fo the Far Virtual Detector (FVD) consist of a simple 20 m × 20 m plane, 1 mm thick as all detectors and made of vacuum, placed at the end of the beamline 25 m from decay tunnel end with its face perpendicular to the beam's axis; all space between hadron dump and FVD is filled with molasses, to properly simulate bedrock particle absorption.

2.5 Simulation and data handling

After modeling the beamline, a series of simulations with different shielding setups have been done. To minimize statistical errors, each simulation required a high enough PoT events, but a too high proton count would produce files too big in size to be properly handled, and would also sharply slow down simulation processes. Geant4 simulations are in fact very computationally heavy, since every particle produced must be simulated and evolved, each step checking boundaries and updating data; in the end it was decided that each simulation run would consist of 10^8 PoT events, which in turns means a relative statistical error of $\epsilon = 10^{-4}$, deemed acceptable. Due to time restrictions, some simulation had a lower PoT count (10^7) to speed up analysis.

To speed up process, each simulation has been run on available resources at the CC-IN2P3 center [36], using the batch-queuing system SLURM; each 10^8 PoT run was split in smaller 5×10^4 PoT runs, sent in the SLURS system 2000 at a time in parallel runs. Each run will produce a `runOut.root` containing all all required data. Each run output file handling is done by the `G4UserRunAction` user defined class. Each detector data is saved in an n-tuple inside the file, and for each particle hit position (both in detector F.o.R., `x` and `y`, and absolute F.o.R., `absx`, `absy` and `absz`) and time `t`, momentum components (`px,py,pz`), energy `E`, PDG (Geant4 particle identifier string) and its ID in the run is saved; for NuTag detectors, also energy lost by the particle in the silicon detector, called `dE`, is saved. An extra ntpule called *neutrinos* is used to save extra data regarding neutrinos impacting FVD is saved; in particular, neutrino energy (`nu_E`, PDG, hit coordinates in FVD F.o.R. (`nu_ix`, `nu_iy`), and origin coordinates (`nu_x`, `nu_y`, `nu_z`) are saved. `runOut.root` file structure is reported in Figure 2.15.

Raw data gathered in `runOut.root` files must be analyzed, and all results from parallel runs merged. Data processing is done in two phases: each `runOut.root` is preprocessed, passing it in a ROOT macro that from raw data produced a series of histograms and calculates mesons yields. Then, another ROOT macro is called to merge all preprocessed data into the final output, and all final yields, S/N ratios, and fluxes graphs used in this thesis are prepared.

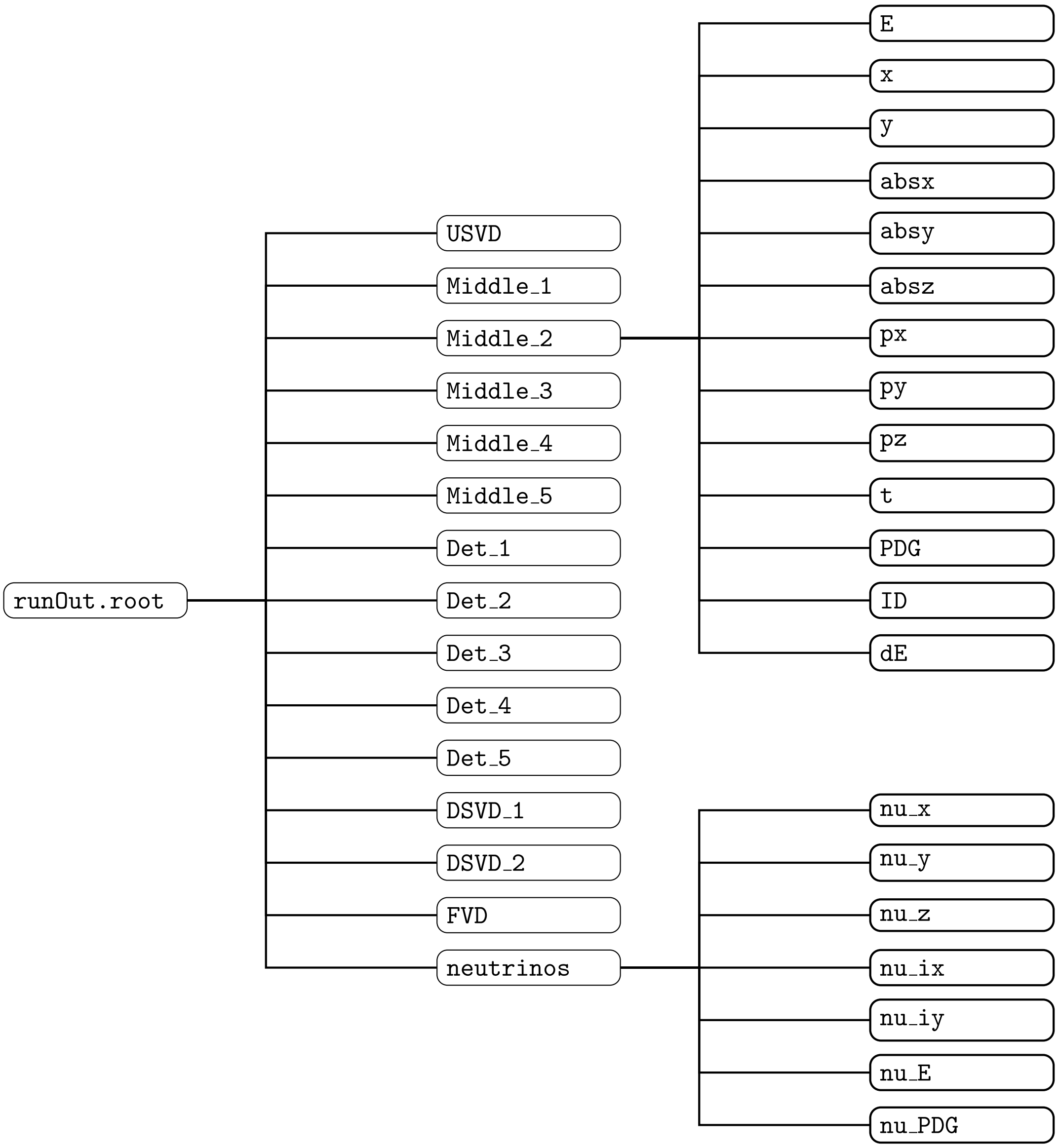

Figure 2.15: `runOut.root` file structure with data labels, as defined in `G4UserRunAction`.

Chapter 3

Simulation results

3.1 Particle budget

The first part of data analysis focused on understanding particle production and propagation in the ENUBET beamline. Data gathered in all detectors is used to estimate particles fluxes, rates and the overall yield of the beamline.

To make data more readable, each of the most common particle species have been color coded in histograms and graphs. Color coding is reported in Table 3.1.

Particle	**Color**	**TColor definition**
Neutrino	⬜	kGray
Anti-neutrino	⬜	kGray+1
Photon	🟨	kYellow
Neutron	🟩	kGreen
Antineutron	🟩	kGreen+1
π^+	🟥	kRed
π^-	🟦	kBlue
K^+	🟧	kOrange
K^-	🟦	kCyan
K^0	⬛	kBlack
Proton	🟪	kMagenta
e^-	🟦	kBlue+2
e^+	🟥	kRed+2

Table 3.1: Particle color coding for graphs.

3.1.1 Particle production at target

The USVD virtual detector is placed right at the tip of the target and covers a 10 cm radius region centered at target, and as such it can track almost all particle production in the target. It is thus possible to reconstruct the initial particle budget and how each particle type propagates in the beamline.

As discussed in Subsection 2.2.1, low energy particles, photons and neutrons are killed at first step, so photons and neutrons production is heavily underestimates;

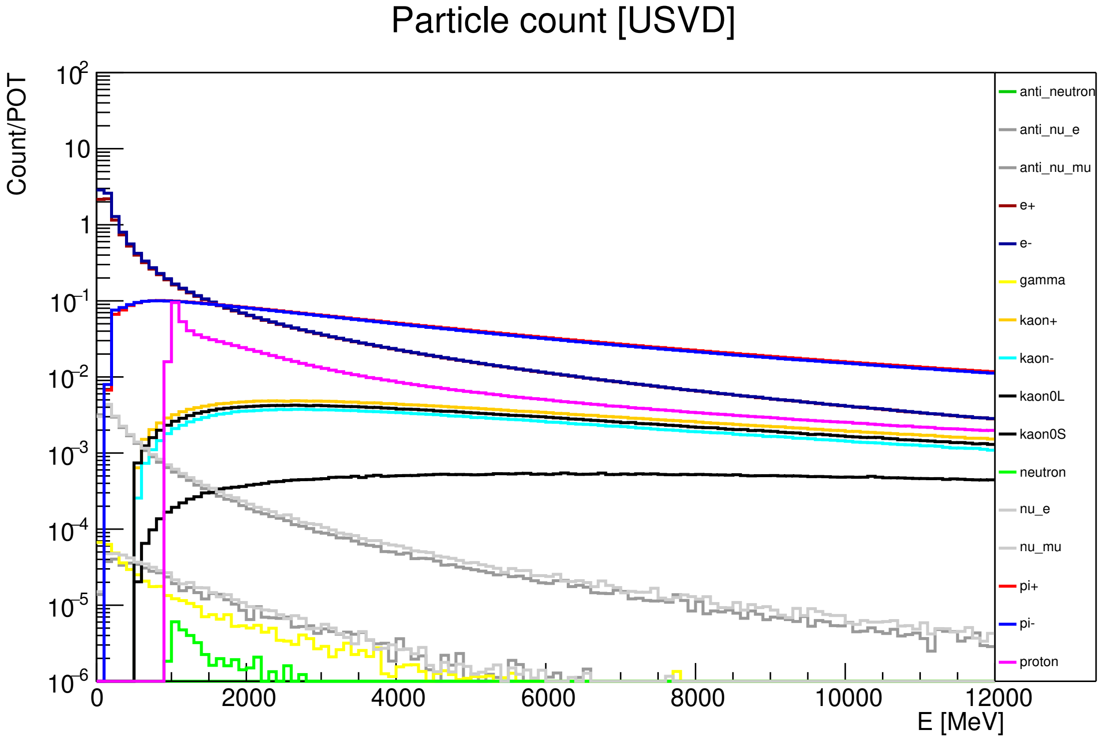

Figure 3.1: Particle budget at the start of the tunnel, from data taken by USVD detector.

that is however irrelevant for this work, as all those particle are not expected to contribute significantly to the rates in the tagger or change the observed neutrino fluxes. On the other hand this has to be kept in mind when considering particle rates at detectors or the stress on them due to ionizing and not-ionizing irradiation that would be underestimated.

The total particle count at USVD, as a function of particle energy, is reported in Figure 3.1. Protons collide non-elastically with carbon nuclei in the target producing all kinds of hadrons, mainly $\pi^{\pm}$, $K^{\pm}$, K^0, p, n. Electromagnetic interactions also produces a cascade of high energy photons, that undergo pair production, and thus contributes to the $e^{\pm}$ flux. Recoil from proton-nuclei collision expels heavy ions from the target, however their number is minimal and are thus ignored.

Electronic and muonic neutrinos and antineutrinos are also produced; these neutrinos are a background source as they cannot be tagged by NuTag or ENUBET instrumentation, since they are not produced by decaying mesons in the active region. These neutrinos arise from early decays in flight in the proximity of the target or from decay at rest. They tend to be of low energy and thus very suppressed by the cross section. Furthermore they have a broad angular distribution pointing in the proton direction. On the contrary the monitored neutrinos, that are produced at about 18 degrees off axis, point, by construction in the direction of the neutrino detector. Nevertheless as I will show later it is very important to try and reduce as much as possible this contribution of “not monitorable” neutrinos. This does not however means that neutrinos coming from interactions and decay in the target region cannot produce signals in the near detector, since all particles produced in a decay will have an angle with respect to target axis due to decay kinematics. In fact, plotting neutrinos starting coordinates as in Figure 3.2 shows that a significant portion of neutrinos are produced in the target region. More about this category of neutrino "background" will be discussed in Section 3.1.4.

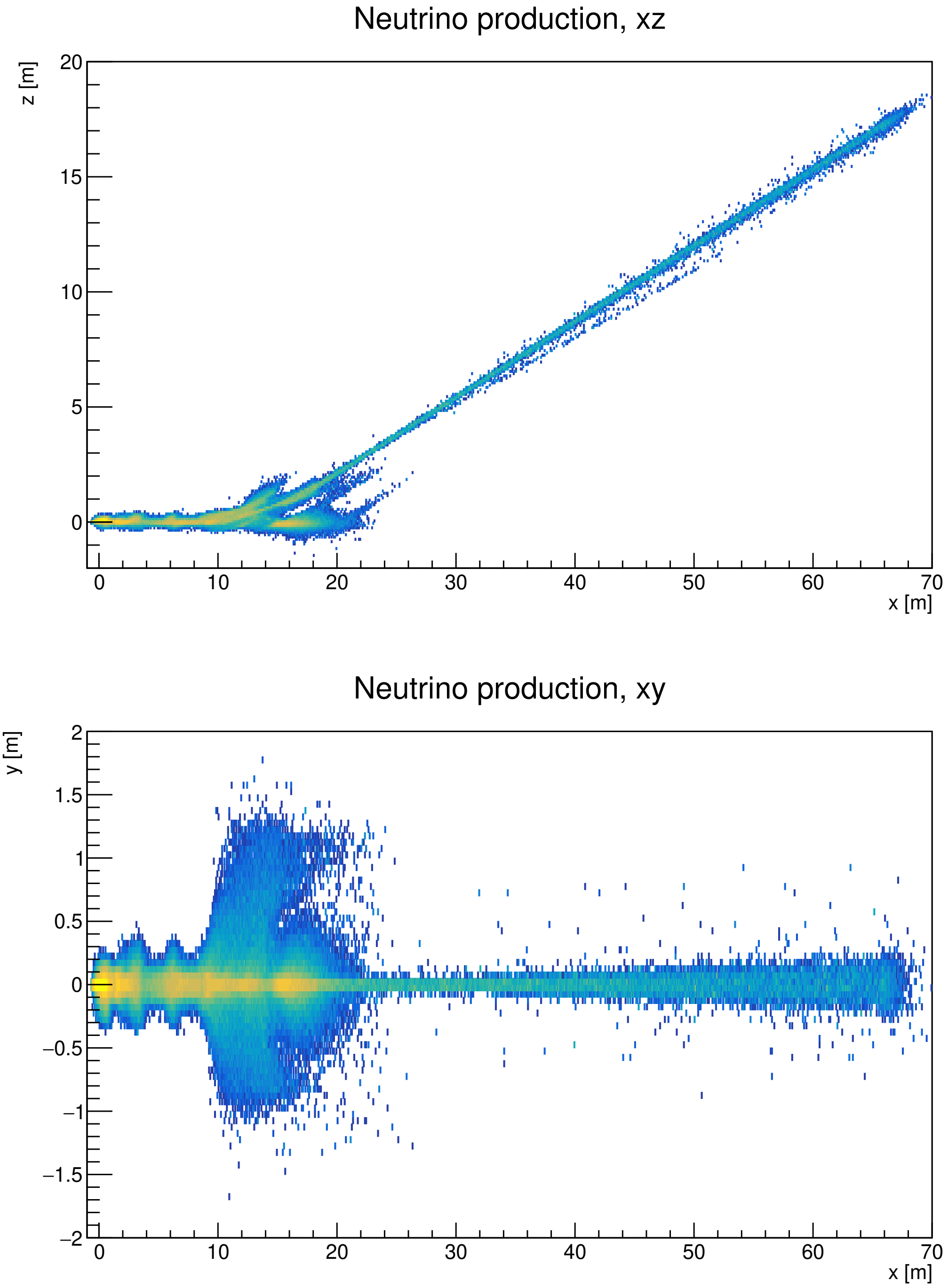
Neutrino production, xz

Neutrino production, xy

Figure 3.2: Neutrino production heatmaps in beamline coordinates, weighted on produced neutrinos energy. Up: projection on xz plane. Down: projection on xy plane

Because of protons high energy, we expect most of particle production to be directed forward towards beamline entrance. Interaction probability of a proton with target is given by the following equation:

$$P_{int} = 1 - e^{\frac{x}{\lambda}} \tag{3.1}$$

in which $\lambda = 38.89$ cm is proton interaction length in carbon and $x = 1.3$ m is the target length. The equation gives a 96.47% interaction probability; this means that $\sim 4\%$ of accelerated protons actually enter the beamline, and may interact along the beamline generating more particles.

3.1.2 Positron reduction

Positron counts reduction in particle budget along the beamline is an important step in incrementing beamline and detector performances. Since ENUBET tags K_{e3} events, reducing positron background from other sources is very important; while positron background comes from antimuons decays ($\mu^+ \rightarrow e^+\nu_e$), it can also come from the electromagnetic component of hadronic interactions in the passive elements of the beamline (collimators, magnets). Most of these positrons are well collimated and do not pose a problem when tagging positrons from K_{e3}; still the fraction of these falling at high angles and low momenta create an irreducible background that needs to be removed at source.

A reduction of the positron rates is also important to maintain particle rates on NuTag detectors in the operating region, which is below 100 MHz/mm^2 and is the maximum read-out rate for fast tracking silicon detectors.

Accounting for all this, to reduce positron propagation along the beamline, at the exit of Quadrupole5 I placed placed lead plate, 12 mm thick and 16 cm in diameter, to absorb positrons before they could reach the tagger. This Lead thickness is equivalent to $0.06\lambda_\pi$, where λ_π is the pion interaction length, and $2.14X_0$, with X_0 being the Lead radiation length; a very small pion and kaons absorption is hence expected while keeping a good positron absorption.

To measure lead plate effects on particle propagation, data gathered by `Middle4` and `Middle5` detectors have been compared; in particular, e^+, π^+ and K^+ counts and fluxes have been studied in order to see the effect on the two components that need to be preserved or removed. It should be noted that the two detectors are not exactly upstream and downstream of the lead absorber: `Middle4` is placed before Quadrupole5, thus also the impact of the quadrupole field and structure is accounted for in this analysis; however, quadrupole impact on positron cut is expected to be minimal and its presence does not alter the interpretation of the effect of the absorber.

Positron counts in `Middle4` and `Middle5` are shown in Figure 3.3, and flux quantities are reported in Table 3.2. While positron count is not significantly reduced in absolute terms, energy loss is significant, and in the selection region for dipoles (also denoted as "momentum bite", [7.5, 9.5] GeV/c) positron count is sharply reduced. This means that positrons still traveling in the beamline will be dumped aside by the next dipole. As we will show later in the chapter (Figure 3.7) at tunnel entrance, only a small fraction of e^+ actually survives.

The insertion of the Lead absorber has however an impact on all particles passing through the beamline, including pions and kaons; they can interact with lead, impacting on nuclei and lowering the total particle flux, or lose energy while traveling

Figure 3.3: Positron count before and after lead cup.

Det. name	**Total count [/PoT]**	**"Momentum bite" count [/PoT]**
Middle4	0.1733	0.0906
Middle5	0.1487	$1.635 \cdot 10^{-5}$

Table 3.2: Positron count before (Middle4) and after (Middle5) lead plating. Counts are normalised for PoT events.

into the material. From the Bethe-Bloch formula, the expected energy loss for a pion or a kaon passing through a 12 mm lead plate is, respectively, 24 and 183 MeV; both are small enough with respect to the particles energy and hence the effect is minimal. This means that particles that had a slighly higher momenta enter the momentum bite while other exit, in approximately equal amounts. Interaction probability is instead defined in Equation 3.1: given $x = 1.2$ cm is the lead thickness and $\lambda = 19.90$ cm the interaction length for pions and kaons, the mesons interaction probability is 5.85%, which in turn means a particle flux is reduced of the same quantity. Pions and kaons counts at Middle4 and Middle5 have been also computed to check flux reduction and energy losses, and they are reported in Figure 3.4; particle rates are reported in Table 3.3.

As it can be seen inside the momentum bite pions and kaons are reduced to an very small, extent compatible with the absorption effect that we just estimated. Outside of the momentum bite a significant absorption is observed. This is due to the presence of the quadrupole that absorbes particles that fall out of its acceptance. In this case it is safe to assume that the count reduction is mainly due to particle absorption in the quadrupole structure and de-focusing of unwanted particles due to quadrupole magnetic field, as particle counts are reduced significantly more than the expected 5%.

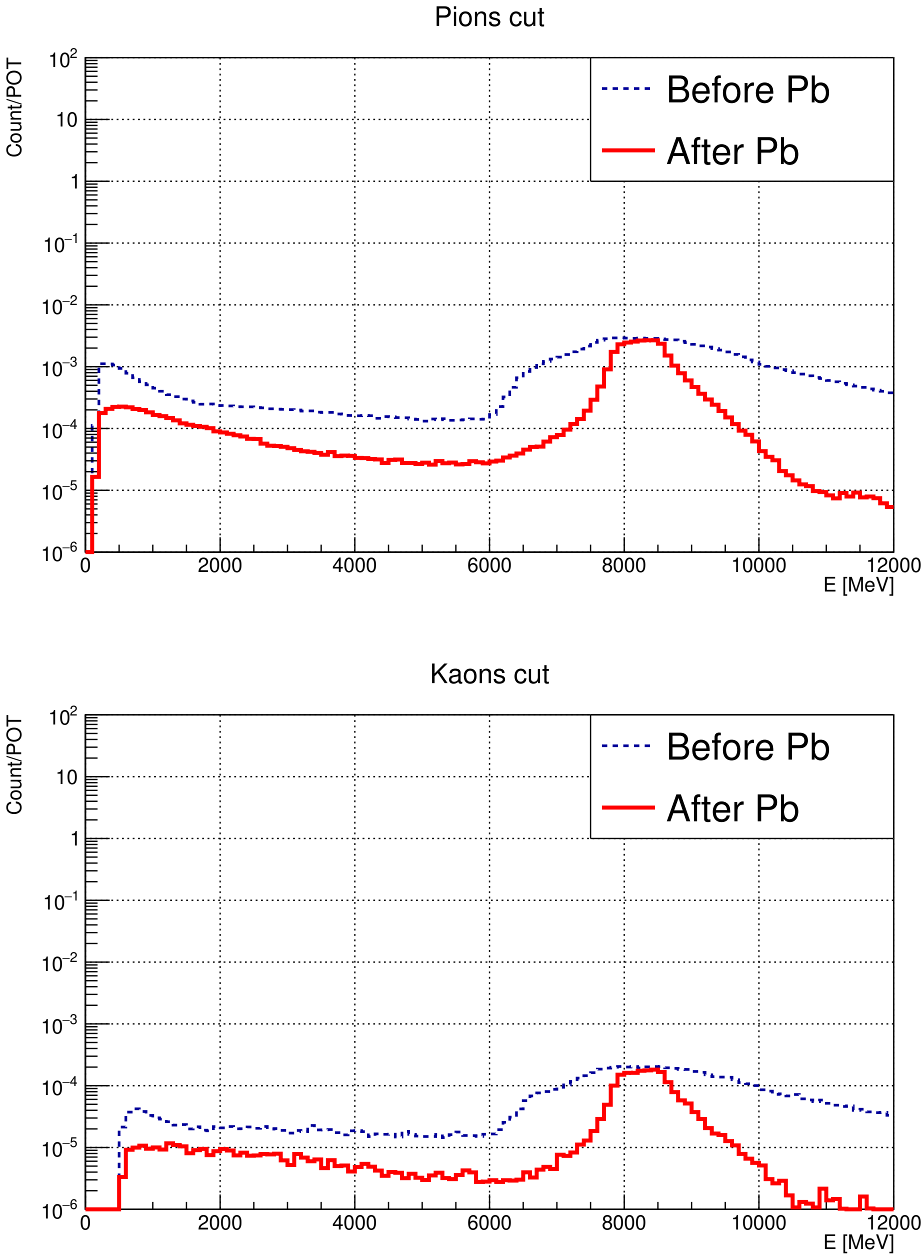

Figure 3.4: Pions (up) and kaons (down) counts before and after the lead absorber. Counts are normalized to PoT.

3.1.3 Beamline yield

As discussed in Section 2.1, the beamline has been optimized for pion and kaon transports up to the decay tunnel. Optimization algorithms for aperture and length parameters of all components have been used to maximize mesons yield at the decay tunnel entrance.

To estimate how well the beamline performs, pions and kaons yields are computed as number of pions and kaons, normalized to proton-on-target (PoT) count. To keep track of meson transport along the whole beamline, this number has been

Particle	**Det. name**	**Total count [/PoT]**	**“Momentum bite” count [/PoT]**
π^+	Middle4	0.1054	0.0330
	Middle5	0.0541	0.0268
K^+ ($\times 10^{-3}$)	Middle4	7.58	2.30
	Middle5	3.81	1.81

Table 3.3: Pions and kaons counts before and after the lead shielding. Normalized to PoT. Momentum bite particles are in the [7.5, 9.5] GeV energy region.

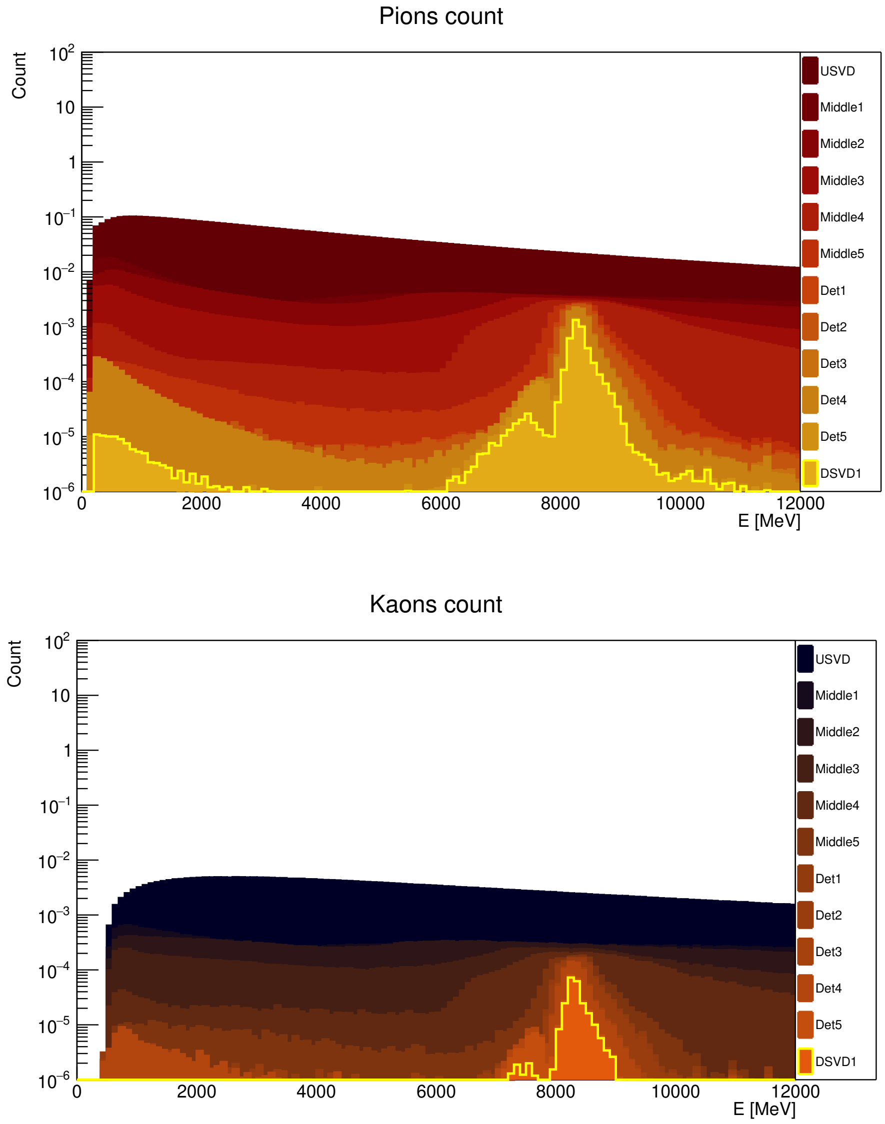
Pions count

Kaons count

Figure 3.5: Pions (up) and kaons (down) energy distribution evolution along the beamline. Brighter colors means a detector closer to the decay tunnel. DSVD1 data is highlighted in yellow.

calculated for all detectors inline, as shown in Figure 3.6. The most important parameter is the pions and kaons yield at tunnel entrance, i.e. the yield calculated at DSVD1. Final calculation gives, for pions, $Y_\pi = 4.66 \cdot 10^{-3}\text{PoT}^{-1}$, and for kaons

$Y_K = 2.68 \cdot 10^{-4}\text{PoT}^{-1}$. The differences in the pion and kaon yields reflect the different production rates at the target that favor pions.

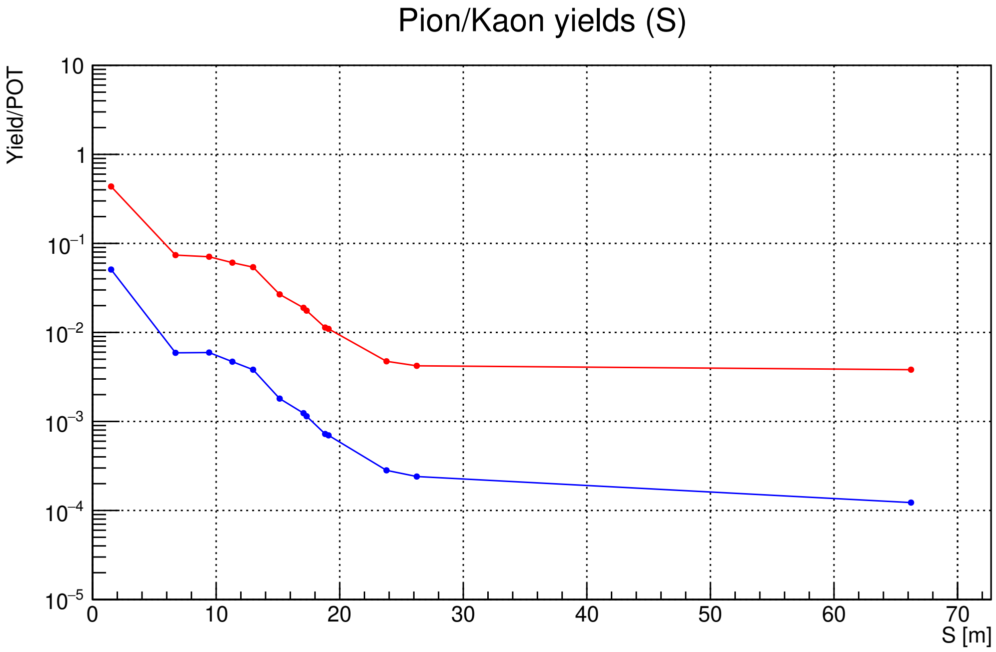

Figure 3.6: Pion (red) and kaons (blue) yield as a function of s.

Detector	**s [m]**	π^+ **count [/PoT]**	K^+ **count [/PoT]**
USVD	1.50000	0.48172	0.05620
Middle1	6.71097	0.08166	0.00652
Middle2	9.43188	0.07827	0.00657
Middle3	11.31275	0.06715	0.00518
Middle4	12.99025	0.05975	0.00421
Middle5	15.13925	0.02956	0.00200
Det1	17.07075	0.02089	0.00137
Det2	17.32075	0.01940	0.00127
Det3	18.82075	0.01253	0.00080
Det4	19.09641	0.01211	0.00077
Det5	23.78540	0.00524	0.00031
DSVD1	26.23540	0.00466	0.00027
DSVD2	66.23540	0.00422	0.00014

Table 3.4: Measurements of π^+ and K^+ across detectors, with corresponding s values (rounded to 5 decimal digits).

The momentum distribution of pions and kaons at the decay tunnel entrance is also checked; their average energy is expected to be 8.5 GeV, with a tolerance of 10%. To check if final mesons energies respect those given parameters, pions and kaons graphs from Figure 3.7 have been fitted with a gaussian function, to find average energy and deviation. The curves are reported in Figure 3.8, with all relative data in Table 3.5. Even tough the gaussian model is evidently not satisfactory, the 3σ confidence interval for both pions and kaons are well into the momentum bite

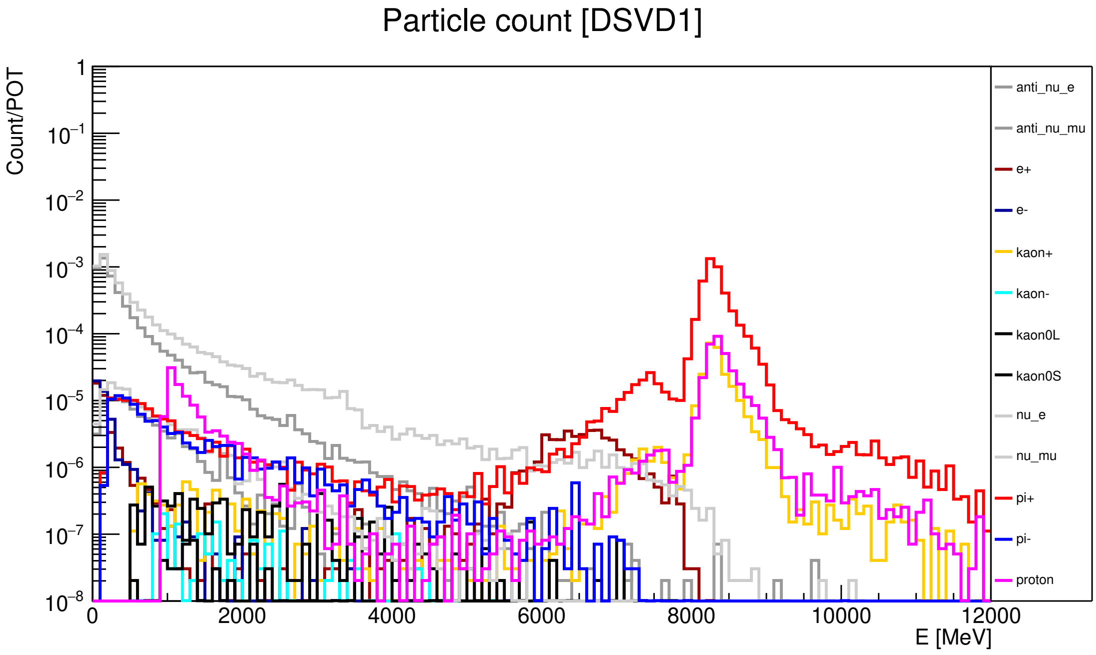

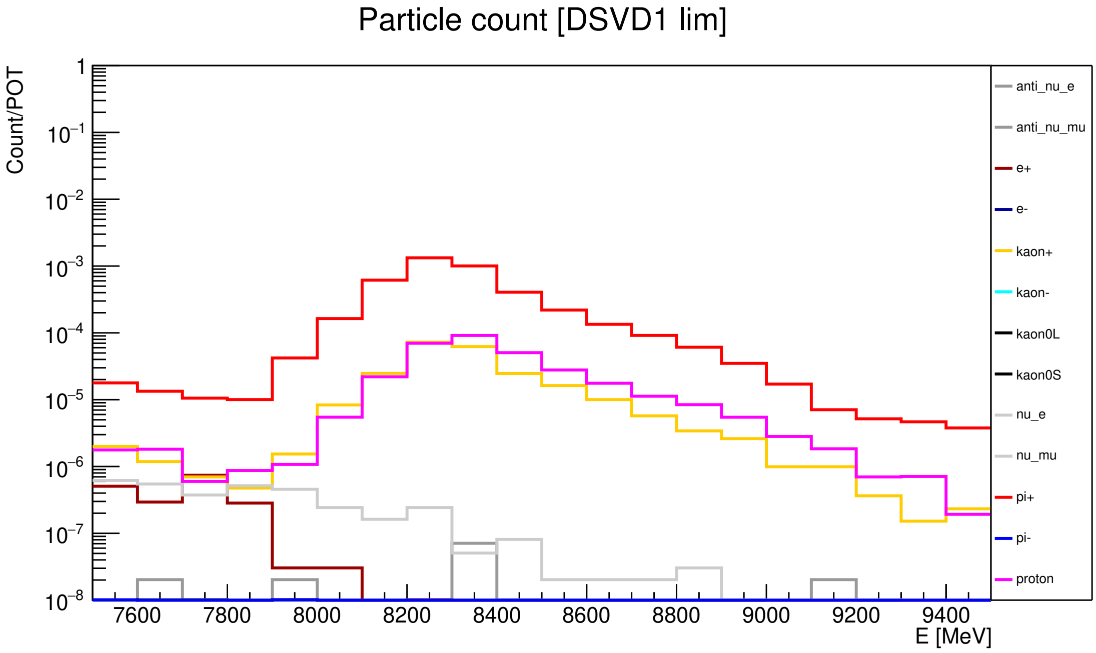

Figure 3.7: Up: particle budget at tunnel entrance, from data taken by DSVD1 detector. Down: zoom on [7.5, 9.5] GeV energy region.

tolerance required for the beamline. As it can be seen in Fig. 3.7 the distribution has a structure at about 7.8 GeV/c which has not been completely understood yet and will deserve further scrutiny. This might be due to some issue in the geometry. In addition a further indication of a problem is given by the absolute yield of pions and kaons that is about a factor 4 smaller that the one of the original BDSIM simulation. Keeping in mind this caveat, we can use the developed simulation to study optimizations of the setup as in this case we only need to perform relative comparisons.

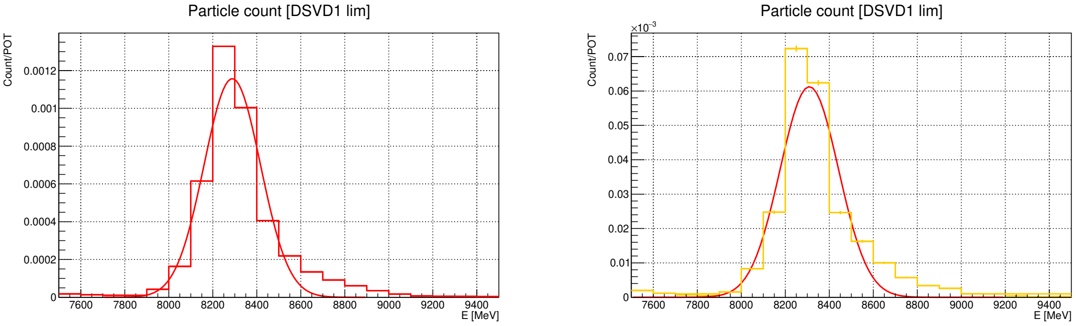

Figure 3.8: Energy fit for pions (left) and kaons (right) at decay tunnel entrance; data is taken from DSVD1 detector.

Parameter	**Pions**	**Kaons**
Constant	$(1.157 \pm 0.003) \times 10^{-3}$	$(6.132 \pm 0.007) \times 10^{-5}$
Mean [MeV]	8288.7 ± 0.2	8309 ± 1
Sigma [MeV]	128.1 ± 0.2	133 ± 1
3σ Interval [MeV]	$[7904.4,\ 8673.0]$	$[7910,\ 8708]$

Table 3.5: Gaussian fit results for pions and kaons.

3.1.4 Neutrinos budget

Neutrinos crossing the FVD detector can be used to estimate the impact of shielding on the low energy neutrino component reaching the neutrino detector; this will be discussed in details in Section 3.2. Another important aspect is to estimate the near detector size. The FVD scoring plane has been kept much larger than a realistic near detector in order to optimize its size. In the current design [14], one of the proposed neutrino detectors is a 4×4 m^2 section, 22.3 m long LArTPC placed 25 m from the end of the end of the instrumented decay tunnel. Its coverage can be verified using neutrinos data gathered at the FVD scoring plane in this new simulation.

Neutrinos weighted rate is plotted as a function of hit coordinates in the FVD F.o.R. (Frame of Reference); using particle rates weighted on their energy instead of particle count is useful to isolate high energy neutrino production from decay tunnel from low energy neutrinos that are originated outside of the instrumented decay region. The $x - y$ distribution, weighted with energy for neutrinos of all flavors, is shown in Figure 3.9. There is a clear separation between high energy, beamline produced neutrinos, which all hit the detector in a small region roughly 2×2 meters around FVD center, and all low energy background neutrino, concentrated on right side of FVD in the [2, 10] m x region.

A simple check for the LArTPC relative position to the beamline can be done from a projection of Figure 3.10 onto the x axis of the $y \in [-2, 2]$ m region, and fitting with a gaussian-like function of equation

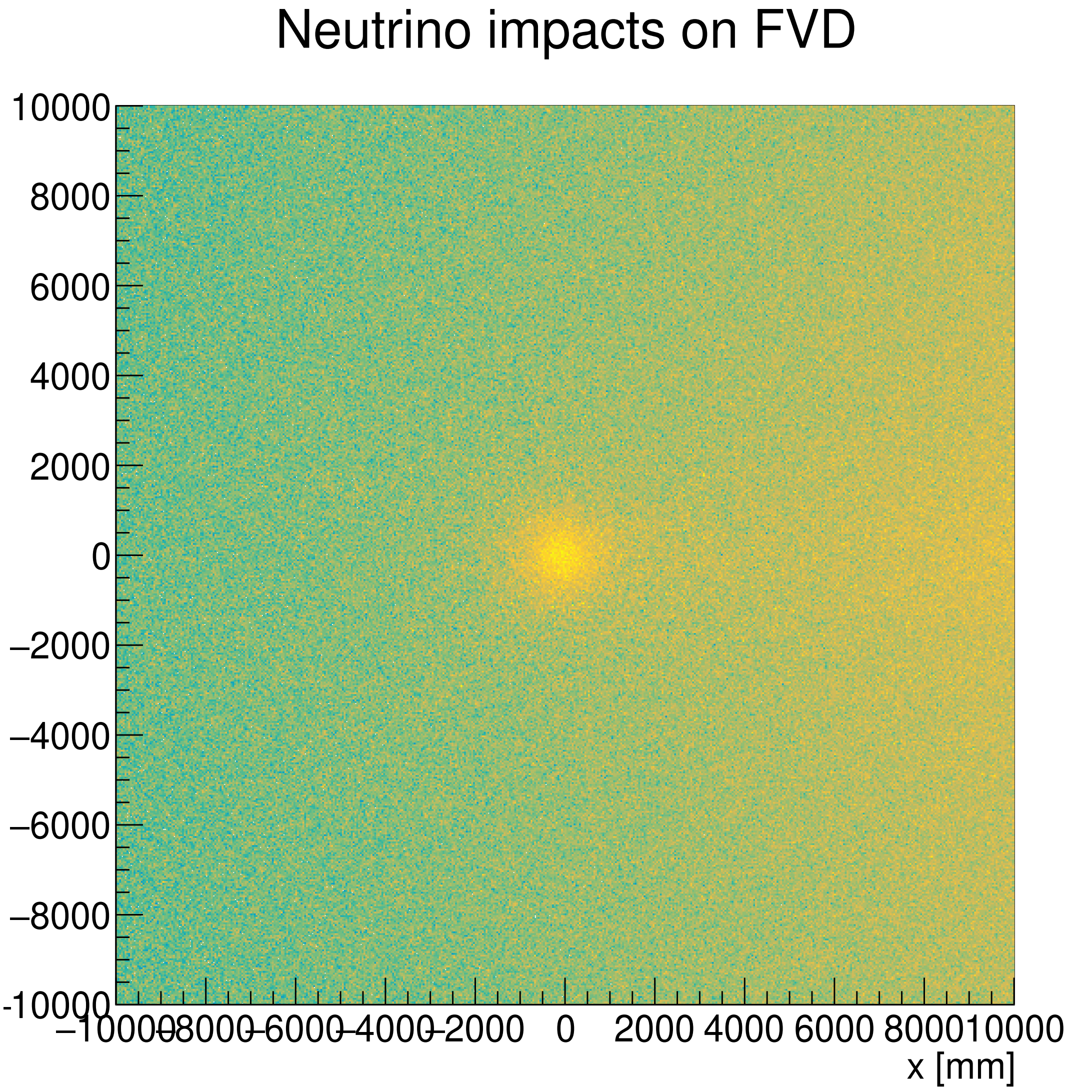

Figure 3.9: Distribution of the hit points of neutrinos at the FVD scoring plane weighed with neutrino energy.

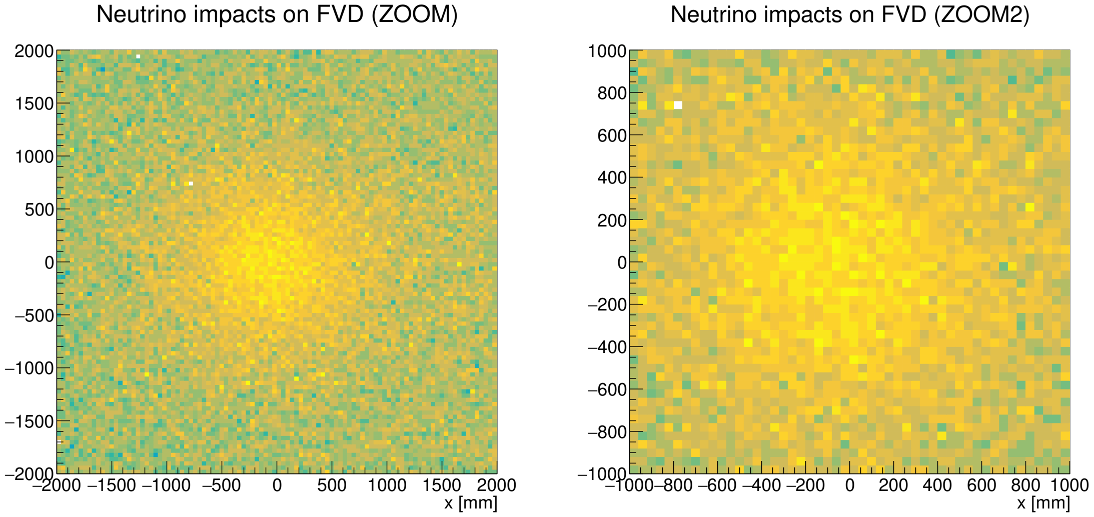

Figure 3.10: Left: FVD neutrinos energy fluxes in the 4 × 4 meters central region, covered by the LArTPC.

$$\mathrm{Fit}(x) = A \exp\left(-\frac{(x-\overline{x})^2}{2\sigma^2}\right) + mx + b \tag{3.2}$$

Fit parameters results are reported in Table 3.6. Final position is estimated as $\overline{x} = -52 \pm 6$ mm; considering the relative distance between detector and estimated fiducial volume section with respect to the real volume section, the LArTPC can be placed along the beamline axis without losing any significant neutrino flux produced from the beamline[1].

Parameter	**Value**
A	0.0256 ± 0.0004 MeV
$\overline{x}$	-52 ± 6 mm
σ	370 ± 8 mm
m	$(2.9 \pm 0.3) \times 10^{-6}$ MeV/mm
b	0.03086 ± 0.0003 MeV

Table 3.6: Fit parameters for FVD position analysis.

The neutrino energy spectrum inside or outside of the 4×4 m^2 fiducial volume is also studied; the neutrino energy spectrum is plotted, both for the inner and right regions, in Figure 3.12; with *inner* region, we refer to the FVD section in which the near detector will be placed and corresponds to the fiducial volume section ($x, y \in [-2, 2]$ m range), while with *right* region we refer to the FVD region contained in the $x \in [2,\ 10]$ m range, along the whole y axis. Inner region spectrum clearly shows the expected features of beamline produced neutrinos, as the pions produced flux (up to ∼ 3.5 GeV) and the kaons produced flux (up to ∼ 8.5 GeV); some low energy background neutrinos are however still visible.

---

[1] It should be noted that the scoring plane is perpendicular to the decay region axis.

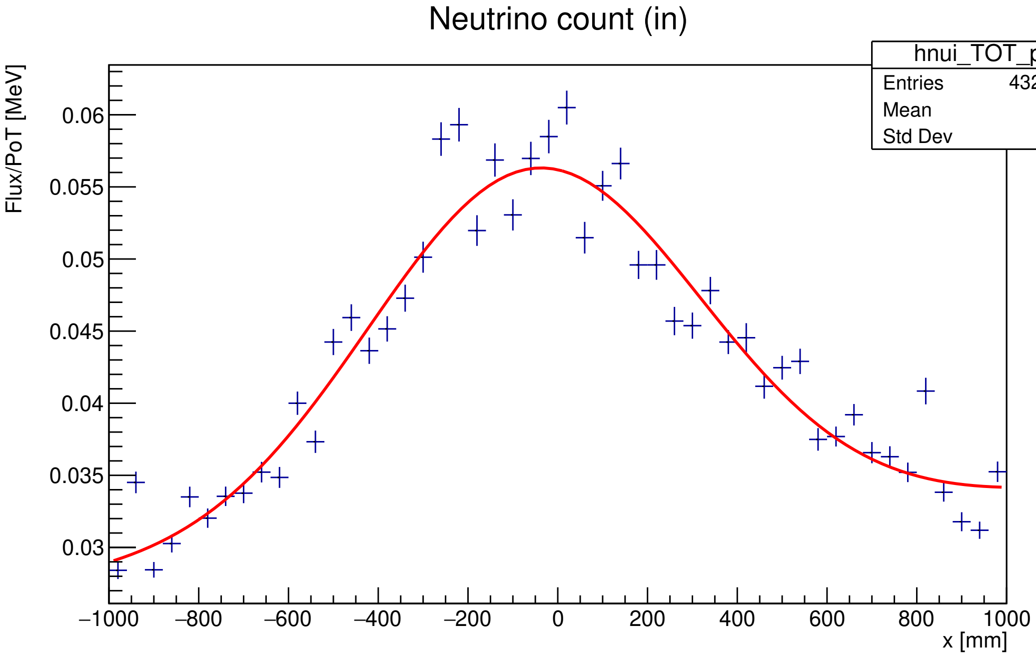

Figure 3.11: x projection of Figure 3.10 and relative gaussian-like fit.

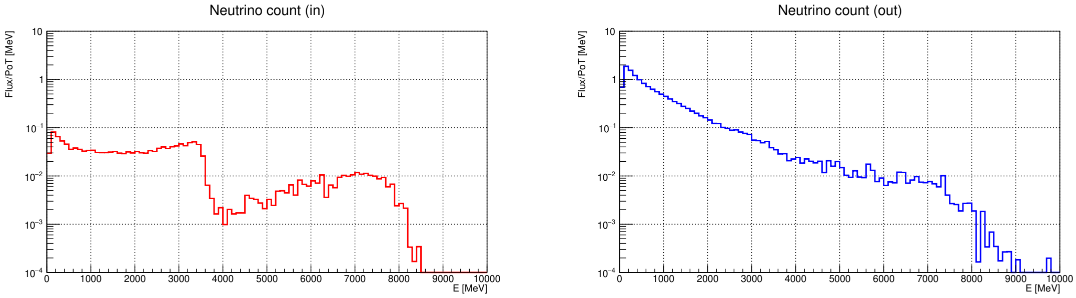

Figure 3.12: Inner region (left) and "noisy" right region (right) neutrinos energy fluxes, as a function of energy.

The neutrino budget in all different flavors is also important to study. Most neutrinos are expected to be muonic flavour neutrinos (ν_μ, $\overline{\nu}_\mu$) from $\pi^+ \rightarrow \mu^+\nu_\mu$ and $K^+ \rightarrow \mu^+\nu_\mu$ decays, with a presence of electronic neutrinos coming from muon and K_{e3} decays; some antineutrinos are expected, from decays of negative mesons produced in proton-graphite interactions in the target, as seen in Subsection 3.1.1.

All neutrinos counts in the fiducial volume, as a function of energy are reported in Figure 3.13; as expected, ν_μ follow the expected mesons-decay spectrum with a clear pion and kaon component, while all other neutrino flavors counts are significantly reduced at high energies. The high energy component of ν_e is the one from K_{e3} decays.

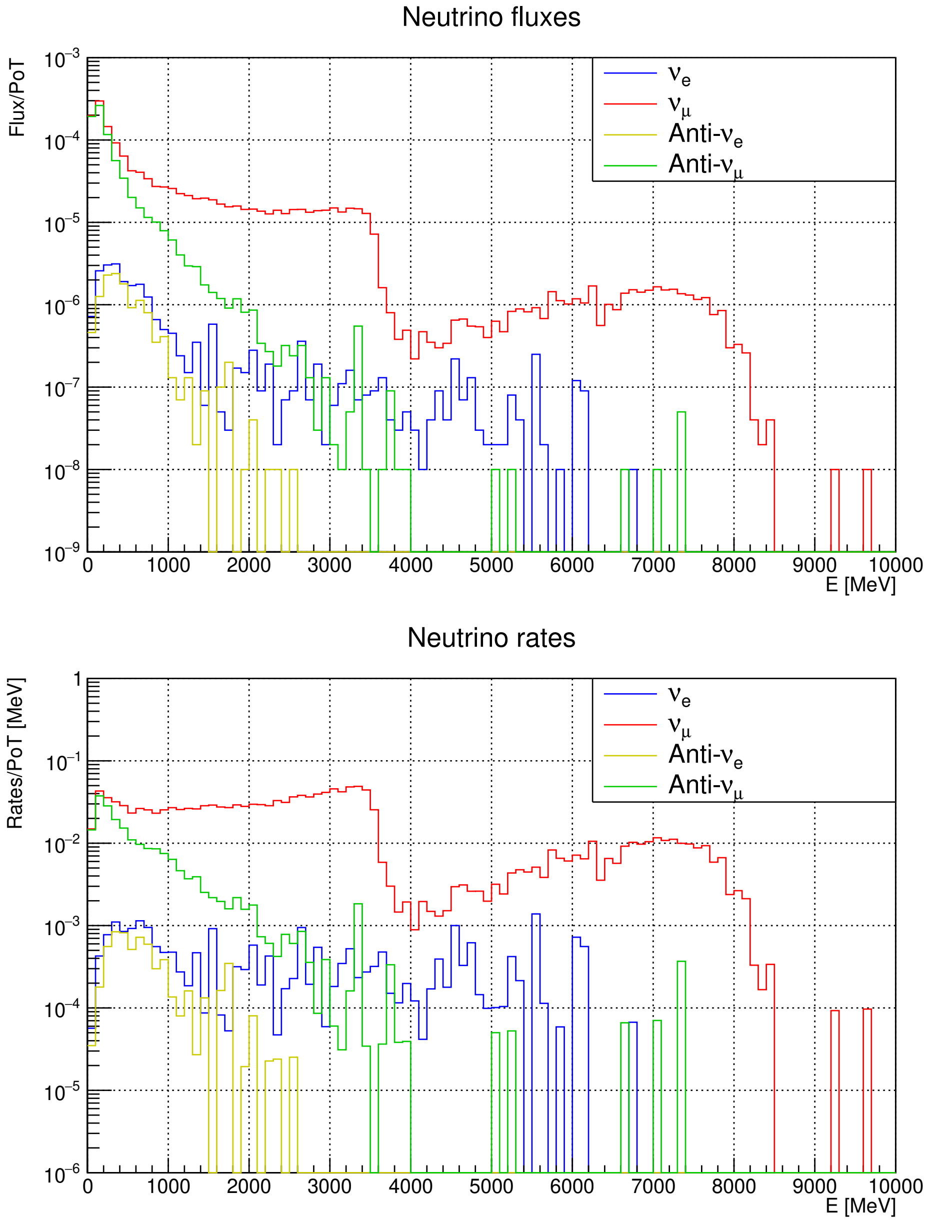

Figure 3.13: Neutrino fluxes (top) and rates (bottom, weighted by neutrino energy) as a function of energy for "prototype" model simulations, divided by neutrino flavor.

3.2 Shielding optimization studies

Beamline shielding is an important part of the design, both for radioprotection reasons and to reduce the low energy neutrino flux on the detector. While shielding on the last segment of the beamline is given by collimators blocks, the beamline before and along dipoles is not shielded in the original BDSIM implementation. For this upstream section, the first beamline shielding that I have introduced ("prototype") uses a heavy tungsten shielding; it is a rather extreme design to see the bulk of the effect and construction or costing considerations have note been addressed. It is composed of two main sections:

- a hollow tube of tungsten, 40 cm thick, and a inner section radius equal to quadrupole outer radius, covering the first section of the beamline from the first quadrupole up to first dipole;

- a series of tungsten plates 18.75 cm thick, placed near the concrete wall in the first dipole section.

A shielding around the target had not been specified in the `bdsim` beamline simulation, but we wanted to study its impact on shielding performances. For first shielding implementation, the CNGS target structure blueprint, reported in Figure 3.14, was then taken as a reference [34] for the target shielding that I implemented: it is a structure comprised of 7 steel and 2 iron blocks, as reported in Figure 3.14. To further improve on this scheme, the slabs have been thickened, leaving only roughly 30 cm of free space around the graphite target in each direction; this has been done taking into consideration a target container similar to the one used in CNGS, 60 cm in diameter [34]. The whole target shielding amounts to a total of $\sim$ 60 cm shielding in all directions; iron and steel have also been replaced with tungsten. All block specifications are reported in Table 3.7; all block depths have been set at 130 cm, the same length as the graphite target; the whole target structure is placed 15 cm above the concrete ground of the target tunnel, as specified in CNGS blueprints.

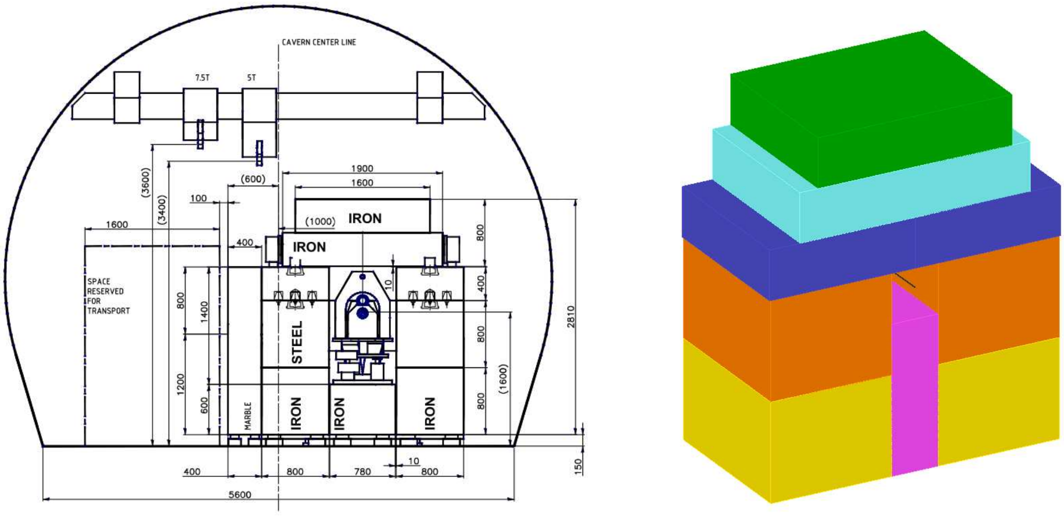

Figure 3.14: Left: CNGS target shielding schematics, from [34]. Right: first implementation of ENUBET target shielding, colored to distinct all blocks.

Block name	Ref. colour	Height [cm]	Width [cm]	Depth [cm]
Base	Pink	90	38	130
Middle blocks	Yellow	80	90	130
Lower blocks	Yellow	80	90	130
Uppers	Blue	40	110	130
Roof	Cyan	40	190	130
Topper	Green	40	160	130

Table 3.7: Final shielding block dimensions in “prototype” model.

A second layer of tungsten shielding, placed in front of the target, has been placed to provide additional absorption of the particles produced at the target. It consist of tungsten disc 70 cm thick and 1.45 m in radius, with a hole 25 cm below its center to accommodate for the drift tube cut using the `G4SubtractionSolid` method. Its Geant4 implementation is in Figure 3.15.

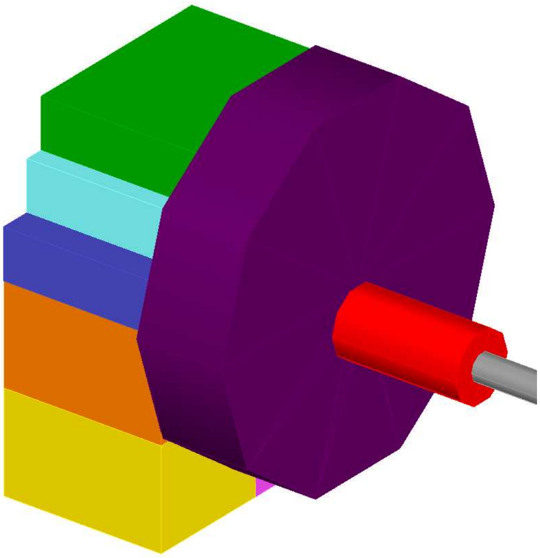

Figure 3.15: Tungsten cap (purple) in its beamline placement. In red, the Quadrupole1 outer structure.

This prototype has been used for all preliminary studies regarding particle propagation along the beamline (Section 3.1) in order to minimize background noise from stray particle and to estimate the best achievable performances. In this section I will discuss a new design for the beamline shielding, compromising between economical cost and actual shielding functionality.

Shielding is not expected to have an impact on final mesons yields, but, as it has already been said it can have an impact on neutrino fluxes on far detectors; mesons produced by proton interactions at large angles are sent outside of the beamline, but can still decay into muons and neutrinos, the latter being possibly detected by neutrino far detectors. Stopping those stray mesons in a thick materials prevents them from decaying into neutrinos and adding to background noise in the near detector.

3.2.1 Benchmark designs

Alternative shieldings have been studied, trying to find a compromise between feasibility and shielding effectiveness.

To have a comparison benchmark, two unshielded beamline models have been tested, along with the prototype previously used for beamline yield studies: the first, referred to as "unshielded", is removed of all beamline shieldings from the prototype, but maintaining all shielding around the target (its structure will be discussed in 3.2.2. The second model, referred to as the "naked" beamline, is removed of all shieldings, both around the target and along the beamline. The idea beyond those designs was to have a reference frame to study real shielding designs; the "prototype" beamline, with all its heavy shieldings, gives a plausible upper limits for particle absorptions, while “unshielded” and “naked” designs give a lower bound for shielding performances. Comparing real shielding designs with those benchmarks can give a proper idea of their performance. All beamline benchmark designs have been reported in Figure 3.16.

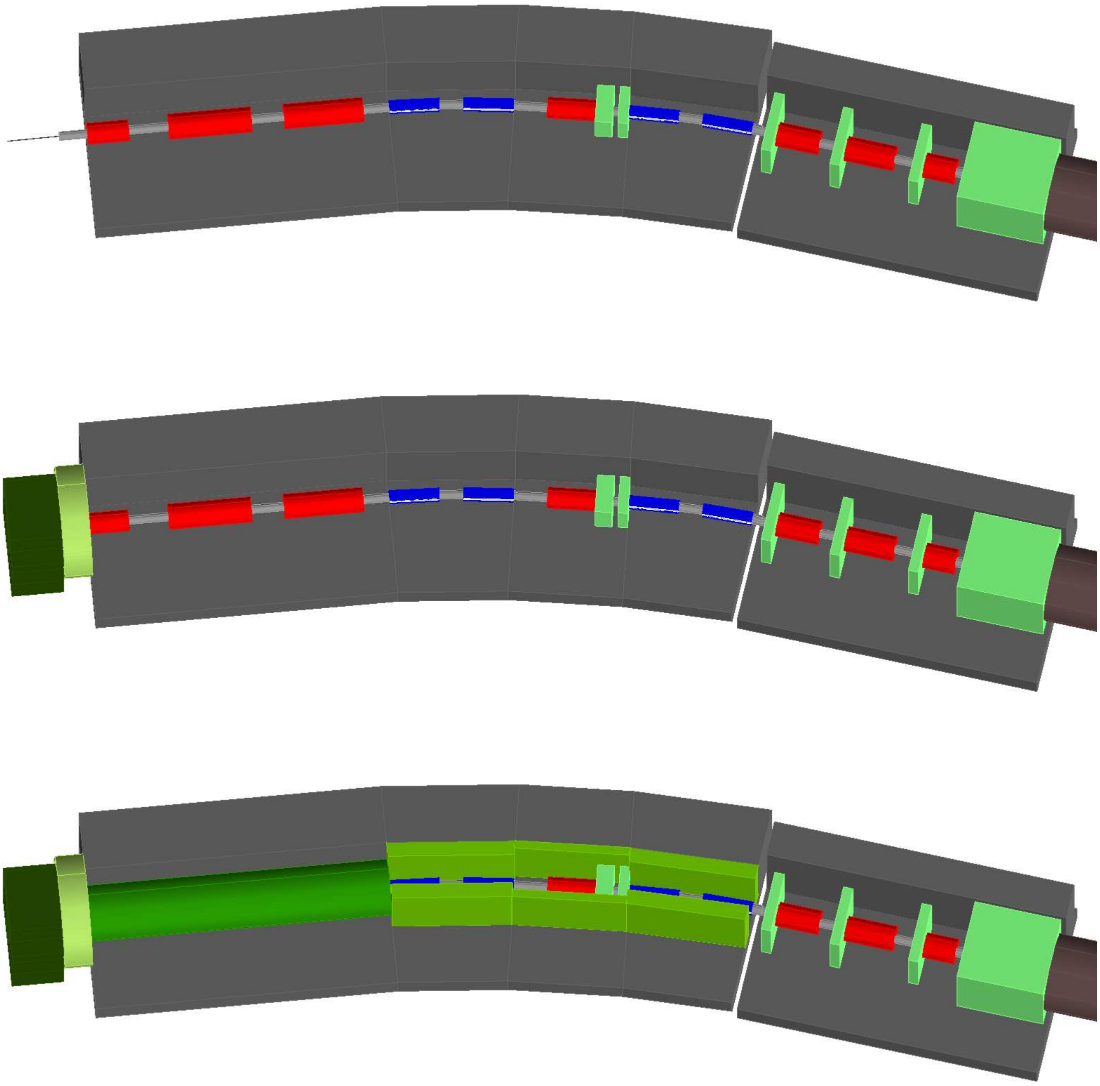

Figure 3.16: Benchmark designs implementation in Geant4. From top to bottom: “naked”, “unshielded” and “prototype” design.

To check that shieldings do not affect beamline yields, pions and kaons count at DVSD1 are reported in Table 3.8.

Data shows that mesons yields do not vary changing the shielding design; this is the expected behavior, as all selected mesons evolve inside the beamline through the whole flight and do not interact with shielding blocks. The only exception is the “naked” design that transports about 7% more pions. This is probably due to stray mesons stopped by the extra shielding present in unshielded and prototype, likely at the target level. Shield design thus do not impact mesons yields and will not be further be calculated for other designs.

Design	π^+ **count [%/PoT]**	K^+ **count [%/PoT]**
Naked	0.495	0.0306
Unshielded	0.460	0.0264
Prototype	0.466	0.0228

Table 3.8: Mesons yields at DSVD1 for all benchmark designs

To better understand the distribution of neutrinos hits and the impact of shielding, the 2D hits histogram in Figure 3.9 is cut in the $y \in [-2, 2]$ m region to isolate the LArTPC section, and is then projected on the x axis; this transformation helps distinguish particle flux features. The signal-to-noise ratio S/N in the LArTPC x region has been calculated for all beamline design, starting from the above-mentioned axis projection: histogram have been fitted in the [-2, 2] m region with Equation 3.2. To estimate background I used the trapezoid formula:

$$\begin{aligned} \text{Background} =& \frac{1}{2}(y_2 + y_1)\Delta x = \\ &= \frac{1}{2}(mx_1 + b + mx_2 + b)\Delta x \\ &\overset{x_1=-x_2}{=} b\Delta x \end{aligned} \tag{3.3}$$

while signal is calculated as *total integral - noise*. The S/N ratio inside the LArTPC detector will be used as a reference metric, in order to quantitatively assess the effectiveness of the beamline shielding designs. It is also an important figure to estimate the total setup performances. It is however important to point out that in this analysis each neutrino entry has been weighted by its energy to simulate the rates which are the real observable.

Comparisons between “prototype”, “unshielded” and “naked” beamline models are reported in Figure 3.17 and Table 3.9. The heavily shielded “prototype” has, unsurprisingly, the best S/N ratio of all. The “naked” beamline S/N ratio is also way smaller than other benchmarks, indicating the importance of good target shielding. As it can be seen in Table 3.9 the S/N ratio for the “unshielded” design is 39.8% higher than the “naked” design S/N, while for the “prototype” design the S/N increase is 61.0%.

Design	**Signal [MeV/PoT]**	**Background [MeV/PoT]**	**S/N**
Naked	0.8530	1.5792	0.5402
Unshielded	0.8643	1.1447	0.7550
Prototype	0.7742	0.8904	0.8696

Table 3.9: S/N ratios data for benchmark designs.

Another approach for background studies is analyzing the low energy neutrino component reaching the LArTPC section. Electron neutrinos, produced in muon or untagged decays of charged and neutral kaons, dominate the low energy region ($\lesssim$ 1000 MeV), but also a muonic neutrino component is present, coming from $K^+ \to \mu^+\pi^0\nu_\mu$ and tertiary decays [22]. It has been already established that high energy neutrinos are the expected neutrinos from tagged decays, while low energy

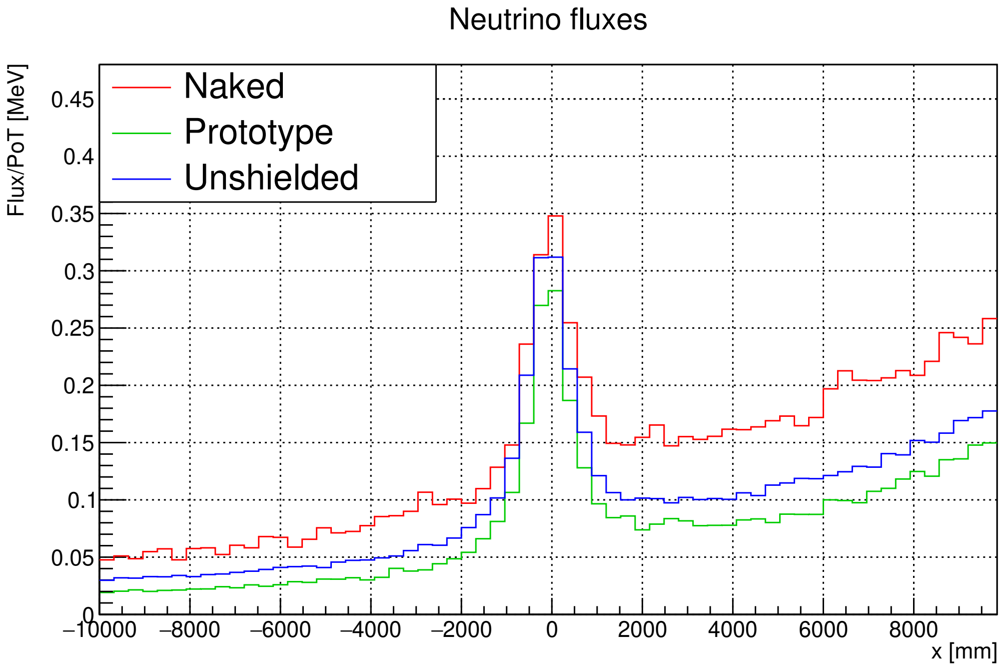

Figure 3.17: Neutrinos hit x position on the FVD. It is obtained from the xy heatmap, cut at $y \in [-2, 2]$ m and projected on x detector axis, for the "benchmark" designs.

causes background signals that needs to be removed; a good shielding thus needs to left untouched the high energy neutrino counts while cutting the low energy counts. The neutrino energy spectrum are shown in Figure 3.18, while neutrino counts are reported in Table 3.10.

Design	ν_e **(low)**	ν_e **(high)**	ν_μ **(low)**	ν_μ **(high)**
Naked	4.070×10^{-5}	10.50×10^{-6}	22.18×10^{-4}	5.321×10^{-4}
Unshielded	2.488×10^{-5}	6.792×10^{-6}	14.71×10^{-4}	5.041×10^{-4}
Prototype	1.686×10^{-5}	5.387×10^{-6}	9.542×10^{-4}	4.196×10^{-4}

Table 3.10: Neutrino counts, separated by energy range and leptonic flavor, for all benchmarks designs. Low energy count refer to neutrinos of energy < 1 GeV, high energy count for > 1 GeV. Counts are normalized on PoT event count.

Table 3.10 shows that low energy neutrinos can in fact be reduced by proper shielding, up to a factor of ~ 10 for ν_μ, while high energy ν_μ fluxes are dampened by $\sim 20\%$;

All data gathered and analyzed in this section will be used for comparison to other, more realistic designs: this so called "benchmark" designs will provide useful data to fully understand how changing shielding design impacts neutrinos counts; in particular, S/N ratios and low energy neutrino counts will be the main comparison parameters.

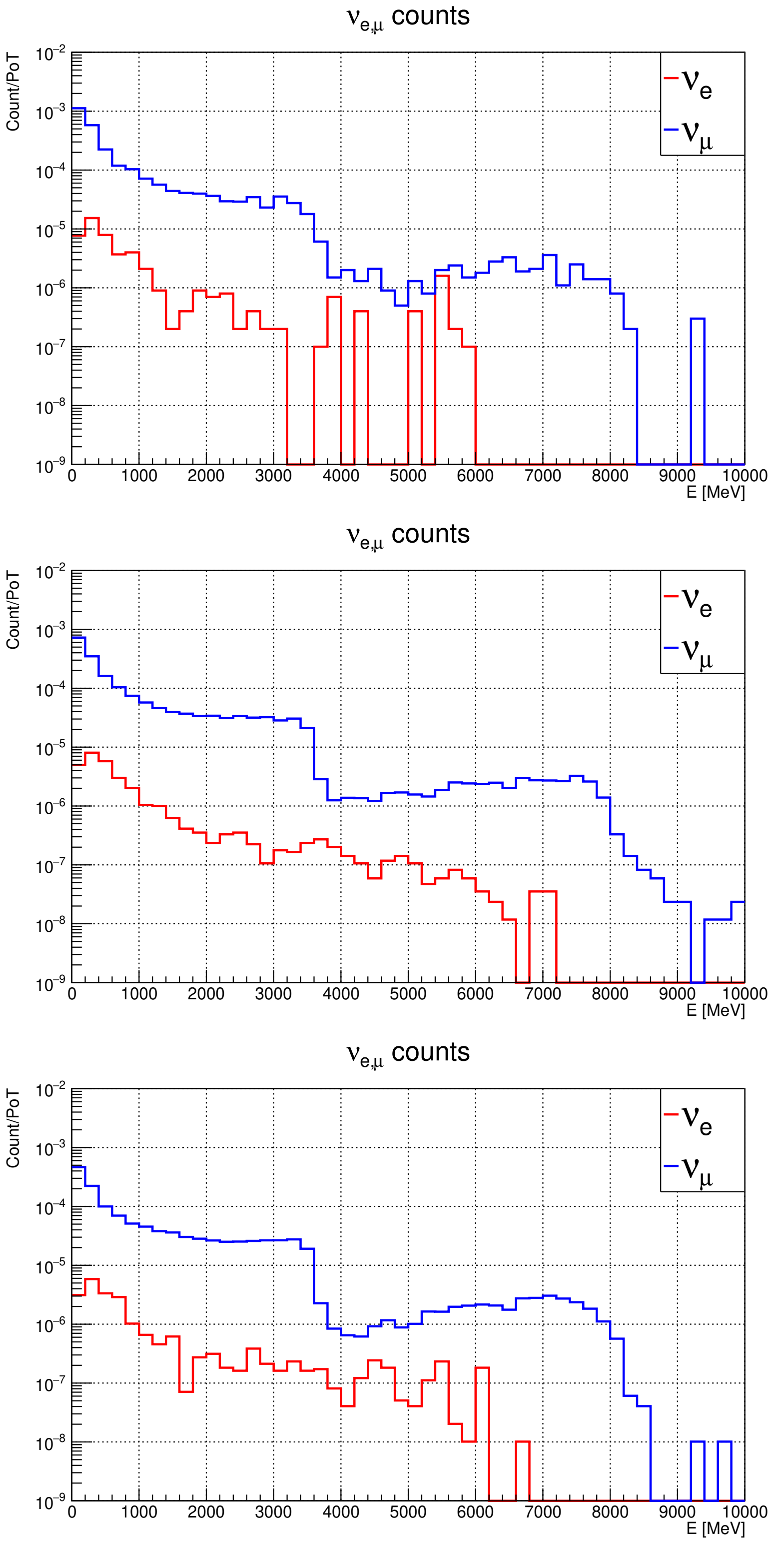

Figure 3.18: Neutrino energy fluxes on FVD, cut at the LArTPC section. From top to bottom: "naked", "unshielded" and "prototype" designs.

3.2.2 Additional target shielding studies

A first study was done on the target shielding structure. Particles produced at target are expected to be the biggest source of background low-energy neutrinos in the FVD, since most of particles are produced at an angle with respect to beamline axis and expelled outside the entrance section. Ideally, all outgoing particles should be stopped by radiation shieldings before any decay can occur, in order to reduce the low-energy component of the neutrino spectrum seen by the near LArTPC detector.

As already mentioned at the beginning of Section 3.2, initial target shielding designs were based on CNGS target schematics, since we expect a similar outgoing particle flux, as target and proton beam parameters are similar to CNGS. With respect to the original blueprints, the lateral shielding was thickened and material was changed from steel to tungsten; this was done to reduce background as much as possible, however there may be a more feasible solution, with lighter and more affordable materials and thinner shieldings. For this reason, the target shielding was modified to match the original CNGS design. The new shielding measures are reported in Table 3.11. Different materials have been tested too.

Block name	**Height [cm]**	**Width [cm]**	**Depth [cm]**
Base	60	78	130
Middle blocks	80	80	130
Lower blocks	80	80	130
Uppers	40	110	130
Roof	40	190	130
Topper	40	160	130

Table 3.11: Final shielding block dimensions in new target design testings.

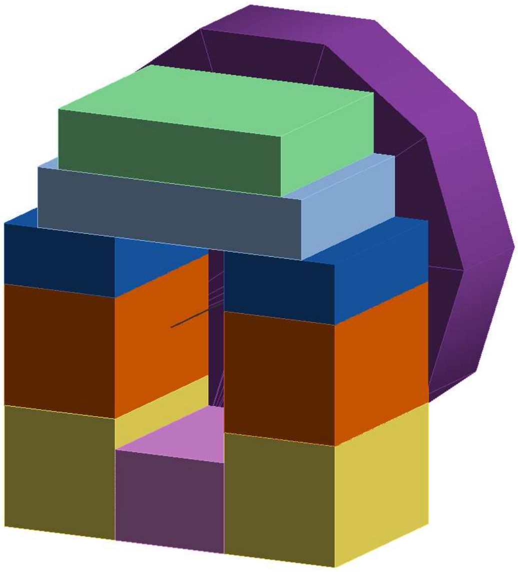

Figure 3.19: Final target shielding and cap designs in its Geant4 implementation, colored to separate all blocks.

Target shielding in "prototype" design also presents, as seen in Figure 3.15, a round cap closing the front of the target region; this extra shielding helps lowering particle backgrounds inside the beamline structure, so it is important its functioning properly. In "prototype" design, this cap is made of tungsten; in following runs, different materials have been tested for this block too.

In total, 3 different target shielding designs have been tested:

- **"Concrete" design:** round cap material is set to concrete;
- **"Steel" design:** round cap is made of steel instead;
- **"Lead"[2] design:** both target shielding and round cap are made of lead.

To study their impact on background reduction, an analysis similar to the one done for benchmark designs in Subsection 3.2.1 has been done; S/N ratio, neutrino counts have been studied and analyzed for all designs to estimate shielding impact. Again, x axis projection of the $y \in [-2000, 2000]$ mm cut, taken from FVD heatmap, have been plotted and fitted with Equation 3.2 to estimate signal and noise intensity. Projections are reported in Figure 3.20, along with "Naked" and "Unshielded" projection graphs (the same plotted in Figure 3.17); S/N data is reported in Table 3.12. S/N ratio increases noticeably as material density grows, as expected since thicker materials stops particle better; in particular, the "lead" design seems to be the best performing shielding, with an S/N increase of 43.2% with respect to the "naked" design, comparable to the thick tungsten "unshielded" design.

To double check if this shielding design is in fact impactful, neutrino fluxes on FVD have been studied, again in the same way as done in Subsection 3.2.1.

Design	**Signal [MeV/PoT]**	**Background [MeV/PoT]**	**S/N**
Concrete	0.9030	1.3484	0.6697
Steel	0.8089	1.3122	0.6165
Lead	0.9429	1.2190	0.7735
Naked (ref.)	0.8530	1.5792	0.5402
Unshielded (ref.)	0.8643	1.1447	0.7550

Table 3.12: Signal and background data for target shielding models and their reference benchmark designs. All designs are variations of the "Unshielded" benchmark design.

---

[2] We have not considered here possible drawbacks of Lead in terms of thermo-mechanical response.

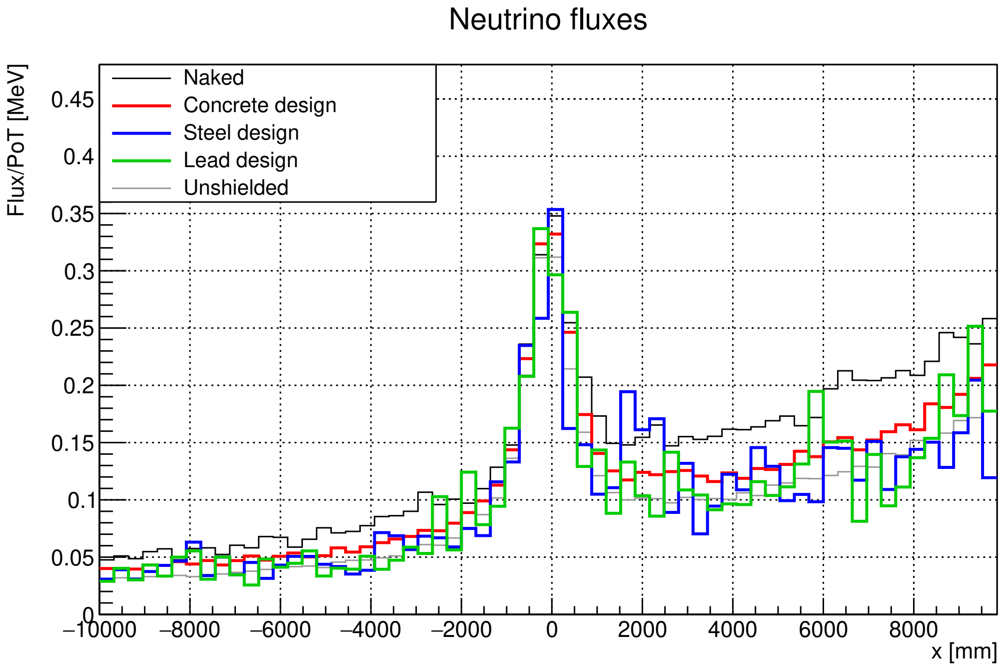

Figure 3.20: x-axis projection of the neutrino FVD heatmap, cut at $y \in [2000, 2000]$ mm, for the target shield tests and their benchmark references

Neutrino counts shows some significant fluctuations, mainly due to statistical uncertainties. All those runs were done on a low statistic regime (10^7 PoT events/run), so it is possible that statistical errors from run data are high enough to produce significant fluctuations.

Design	ν_e **(low)**	ν_e **(high)**	ν_μ **(low)**	ν_μ **(high)**
Concrete	3.615×10^{-5}	6.580×10^{-6}	18.29×10^{-4}	5.268×10^{-4}
Steel	3.170×10^{-5}	13.70×10^{-6}	16.19×10^{-4}	4.966×10^{-4}
Lead	4.779×10^{-5}	2.305×10^{-6}	16.71×10^{-4}	5.397×10^{-4}
Naked (ref.)	4.070×10^{-5}	10.50×10^{-6}	22.18×10^{-4}	5.321×10^{-4}
Prototype (ref.)	1.686×10^{-5}	5.387×10^{-6}	9.542×10^{-4}	4.196×10^{-4}

Table 3.13: Neutrino counts, divided by energy range and leptonic flavor, for all benchmarks designs. Low energy count refer to neutrinos of energy < 1 GeV, high energy count for > 1 GeV. Counts are normalized on PoT event count.

Neutrino counts analysis are thus deemed inconclusive. To decide what is the best design, only S/N ratios have been taken into account; from Table 3.12 the best S/N ratio appears to be one calculated in the “lead” shielding run, so this will be the design used for the final design.

3.2.3 Additional studies on the shielding along the beamline

The second test was done on the shielding around first section of the beamline. In this section there are three quadrupoles, placed for particle focusing; their magnetic fields can deviate some particles, that can travel outside the beamline and decay into

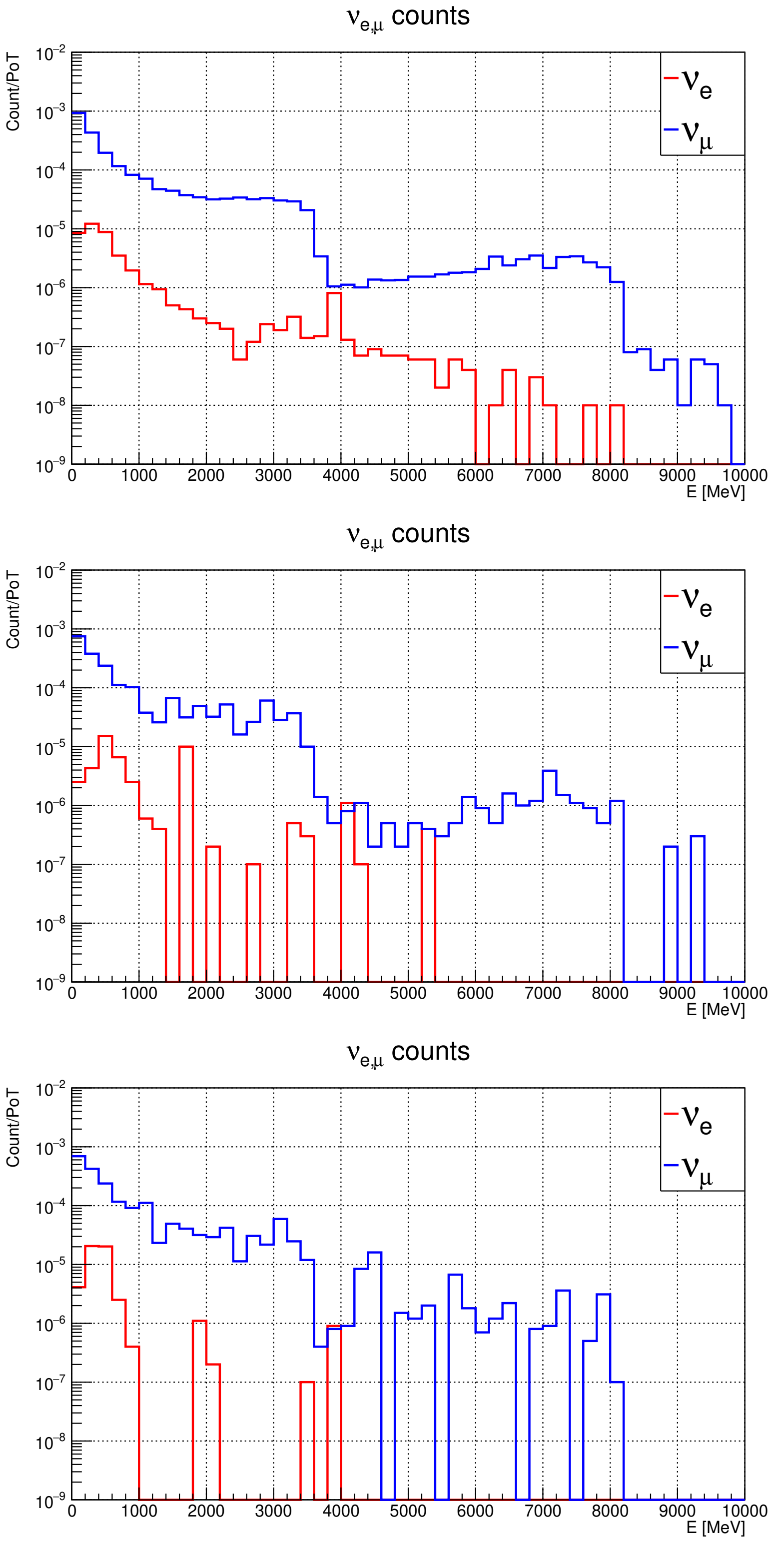

Figure 3.21: From top to bottom: neutrino counts, divided by their flavor, for "Concrete", "Steel" and "Lead" target shielding designs.

neutrinos. Figure 3.2 shows a significant neutrino production in the first beamline segment. This production can be traced back to mesons exiting the beamline, or deflected by quadrupoles, either by their structures or their magnetic fields, are also to be taken into consideration. The final beamline shielding model is reported in Figure 3.23. Taking into account the beamline layout, it is safe to assume that no shielding is needed on the beam left side, since the right bending at dipole section means that particle going on the left side should not contribute to neutrino low-energy background at the FVD. Thus only the right side of beamline has been shielded; the final design is composed of just one big block of lead, 7.563 m long, 1.95 m high and 40 cm thick, occupying almost all free space between beamline structure and right side concrete wall. Its placement in the beamline structure is reported in Figure 3.23. This setup will be referred to as the "lateral shielding" design.

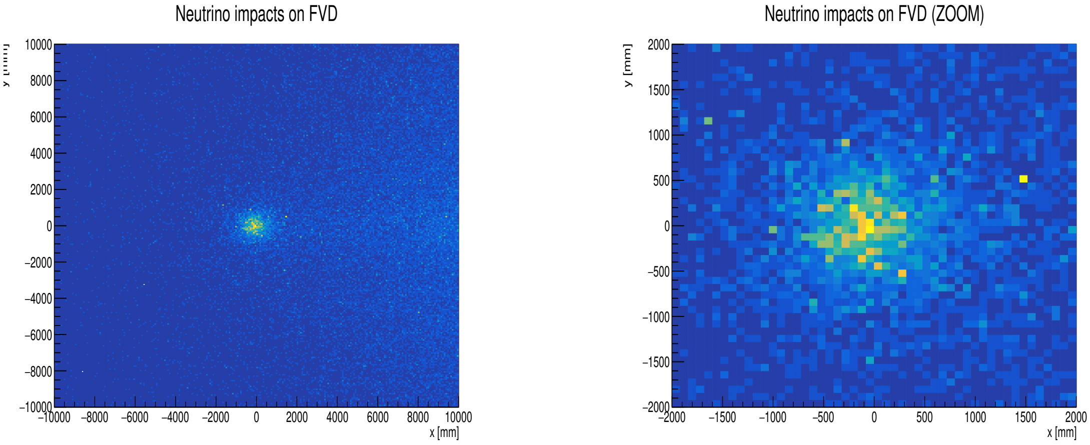

Figure 3.22: Left: Full FVD heatmap of neutrino hits on FVD, weighted on energy. Right: heatmap zoomed on LArTPC region.

As done before for target designs tests, same procedure used in Subsection 3.2.1: x axis projection of the FVD neutrino heatmap, cut at $y \in [-2000, 2000]$ mm, was plotted and fitted with Equation 3.2. S/N ratios and neutrino counts, have been studied and analyzed for all designs to estimate the impact of this shielding.

Projections are reported in Figure 3.24, along with "Naked" and "Unshielded" projection graph plotted in Figure 3.17; S/N data is reported in Table 3.14. S/N ratio appear to slightly improve with respect to the unshielded design, a total of a 2% increase.

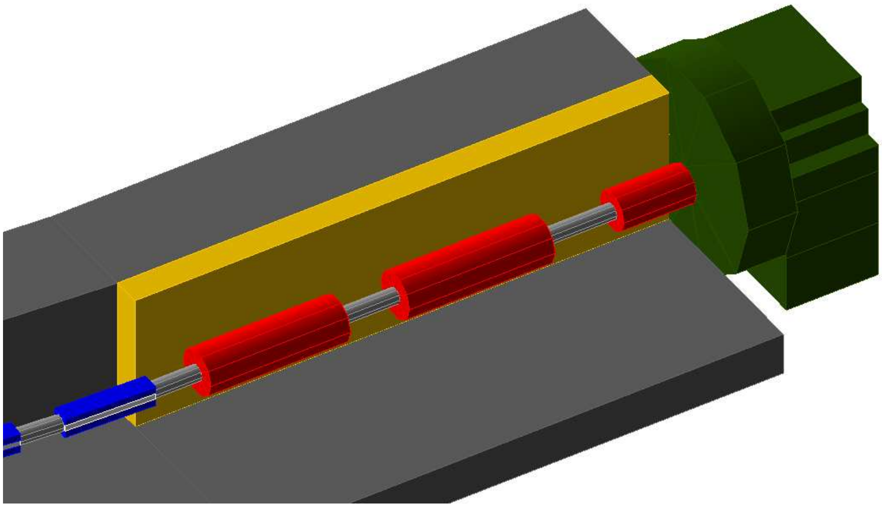

Figure 3.23: Lateral beamline lead shielding, in place in the Geant4 simulation.

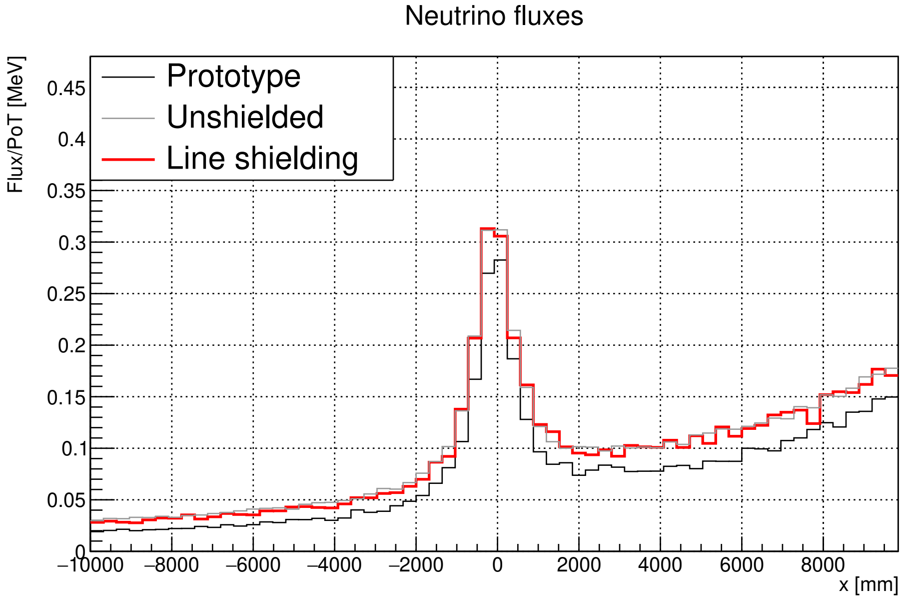

Figure 3.24: x axis projection of the neutrino FVD heatmap, cut at $y \in [-2000, 2000]$ mm, for the Line shielding tests and its benchmark references. "Line shielding" model is a variation on the 'Unshielded" model.

Design	**Signal [MeV/PoT]**	**Background [MeV/PoT]**	**S/N**
Lateral shielding	0.8680	1.9948	0.7704
Unshielded (ref.)	0.8643	1.1447	0.7550
Prototype (ref.)	0.7742	0.8904	0.8696

Table 3.14: Signal and background data for lateral shielding model and its reference benchmark designs.

Neutrino counts, divided by flavor, are reported in Figure 3.25; relative neutrino count data is reported in Table 3.15. Low energy neutrino data show a 3.3% reduction in electron neutrino background, and a 4.4% reduction in low energy muonic neutrino counts. Reductions are very small, however they are statistically significant: as explained in Section 2.5, each run simulates 10^8 proton-on-target events, 10^7 for the lower statistic ones; all detectors gives exact numbers and counts, since detector real response has not been simulated. Because of this, statistical uncertainties are the main error contribution. Relative error given by statistics is estimated as $\epsilon = N^{-1/2}$, with N the PoT count for each simulation; this gives $\epsilon_{low} = 10^{-4}$ for high statistics runs ($N = 10^8$), $\epsilon_{low} = 3.2 \times 10^{-4}$ for low statistics runs ($N = 10^7$). Both values are way below low energy counts reduction calculated above, thus it is safe to assume that those reductions are not statistical fluctuations.

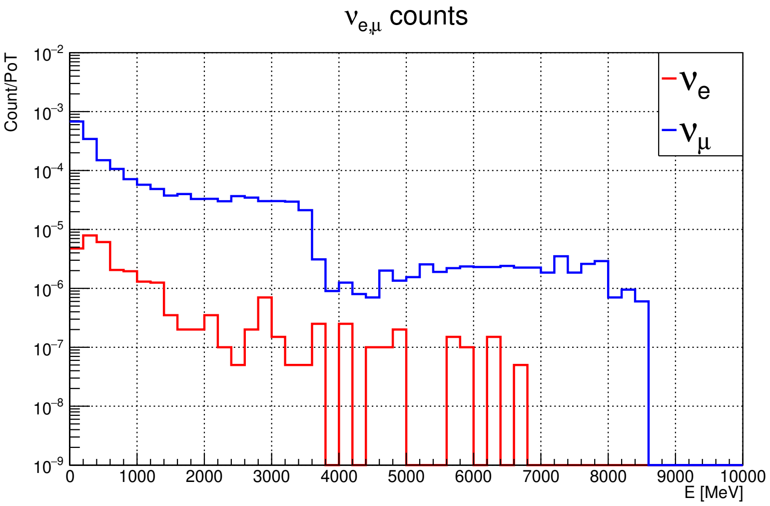

Figure 3.25: Neutrino counts in LArTPC region of FVD, reported as a function of energy, for the "lateral shielding" design. Data regarding electronic (red) and muonic (blue) neutrinos have been reported separately.

Design	ν_e **(low)**	ν_e **(high)**	ν_μ **(low)**	ν_μ **(high)**
Lat. shielding	2.407×10^{-5}	6.306×10^{-6}	14.07×10^{-4}	5.095×10^{-4}
Unshielded (ref.)	2.488×10^{-5}	6.792×10^{-6}	14.71×10^{-4}	5.041×10^{-4}
Prototype (ref.)	1.686×10^{-5}	5.387×10^{-6}	9.542×10^{-4}	4.196×10^{-4}

Table 3.15: Neutrino counts, divided by energy range and leptonic flavor, for lateral shielding design and its reference designs. Low energy count refer to neutrinos of energy < 1 GeV, high energy count for > 1 GeV. Counts are normalized on PoT event count.

Given all gathered data on this design, it is clear that its impact is minimal, considering also the significant quantity of material used for such a big shield: given $\rho_{Pb} = 11340$ kg/m^3, a total of ~ 67 ton of lead should be placed for a mere 3% reduction on low-energy noise. As such, this shielding will not be implemented for further shielding designs and is discarded as a viable shielding for the ENUBET beamline.

3.2.4 Dipole shieldings studies

A third batch of studies was done on shielding in the dipoles region. By design, dipoles' magnetic fields bend particles out of beamline trajectory if their momentum is outside the "momentum bite" region (8.5 GeV/c, with a ±10% tolerance). It is thus expected, that in this region, a consistently large flux of particle travel outside of the beamline axis. Positive particles with momentum lower than selected one are over-bent and sent to the right, towards the FVD side; all other negative particles will instead be sent towards left side of the beamline: positive particle with high momentum will be under-bent, while negatively charged particles will be bent in the opposite direction and towards right side of the beamline. Neutral particles produced at target can be ignored since their occurrence at this point in the beamline is close to zero. To give an idea of particle budget entering dipole section, particle count at `Middle2` detector is shown in Figure 3.26.

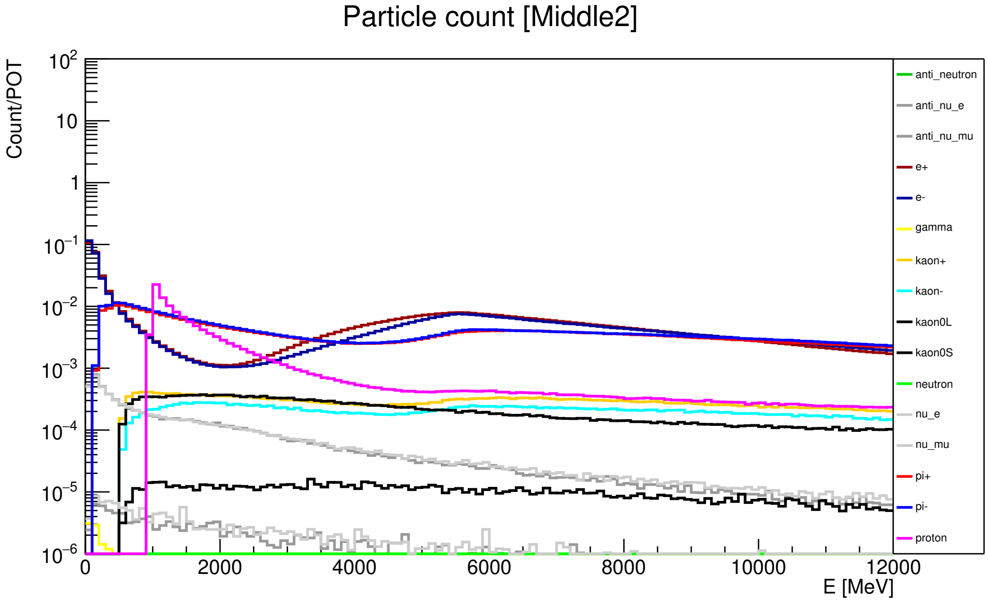

Figure 3.26: Particle budget at entrance of first dipole, from `Middle2` detector.

Because of high particle fluxes exiting from the beamline, it was chosen to shield both sides of the dipoles to maximize particle absorption. To test how much shielding is needed in this region, four different designs have been implemented:

- **"Light" design:** as the name suggest, is the lightest shielding of the three, and is made out of 4 steel plates, each 37.5 cm thick and 1.95 m high, placed on concrete wall in correspondence of first dipole sections. Those plates will cover both dipoles sections. To cover the slightly bent concrete wall, the plates bend too, following concrete curvature.
- **"Heavy" design:** it is a design based on "Light" shielding, at which 2 extra steel plates are added in between the already placed shielding plates. New plates are 20 cm thick, 2.648 m long and again 1.95 m high. Those extra plates will cover the region in between the two dipoles, where Quadrupole5 is placed.

- **"Lead" design:** plates setup is the same as "Heavy" design, but lead is used instead of steel.
- **"Tungsten" design:** as for "Lead" shielding, same design from "Heavy" has been kept but material was swapped to tungsten.

Schematics of shielding designs are reported in Figure 3.27. For all designs reported above, original target shielding design (taken from "Unshielded" benchmark design) was kept, and no inline shield plating was present.

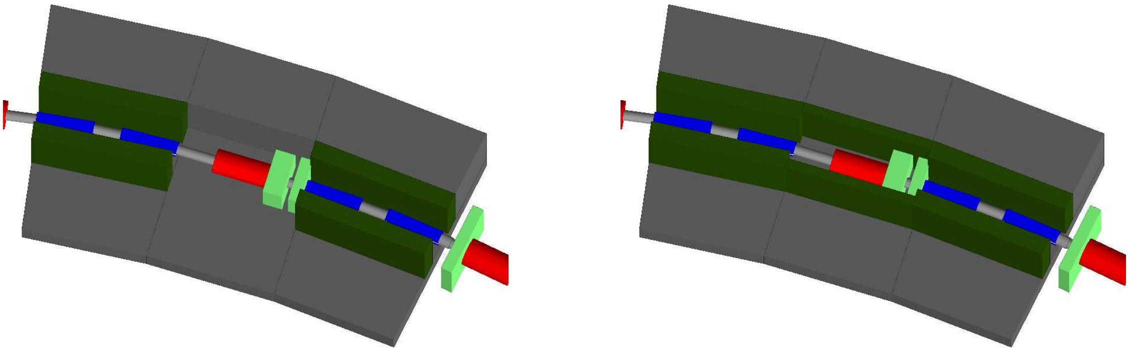

Figure 3.27: Left: light shielding setup. Right: heavy shielding setups. Shielding plates are dark green, concrete structure in grey.

To compare design performances, the same approach used for target and inline shielding testing has been used: following the procedure followed in Subsection 3.2.1, S/N ratios and low energy neutrino counts have been compared between designs, using "Unshielded" and "Prototype" as benchmark designs. First, x axis projection of FVD heatmap, cut at $y \in [2, 2]$ m, has been studied. Its graph is reported in Figure 3.28, and its relative data in Table 3.16. Data shows a significative increase in S/N ratio for all dipole shielding designs with respect to the "Unshielded model", in particular lead and heavy shieldings increases S/N ratio by 24% with respect to the unshielded design, and are even better than tungsten prototype, with a 7.3% increase in S/N; this indicates lead and steel are preferable shielding materials than tungsten.

Design	**Signal [MeV/PoT]**	**Background [MeV/PoT]**	**S/N**
Light shielding	0.8614	1.0356	0.8318
Heavy shielding	0.9054	0.9701	0.9333
Lead shielding	0.8804	0.9439	0.9327
Tungsten shielding	0.8652	0.9748	0.8876
Unshielded (ref.)	0.8643	1.1447	0.7550
Prototype (ref.)	0.7742	0.8904	0.8696

Table 3.16: Signal and background data for dipole shielding models and their reference benchmark designs.

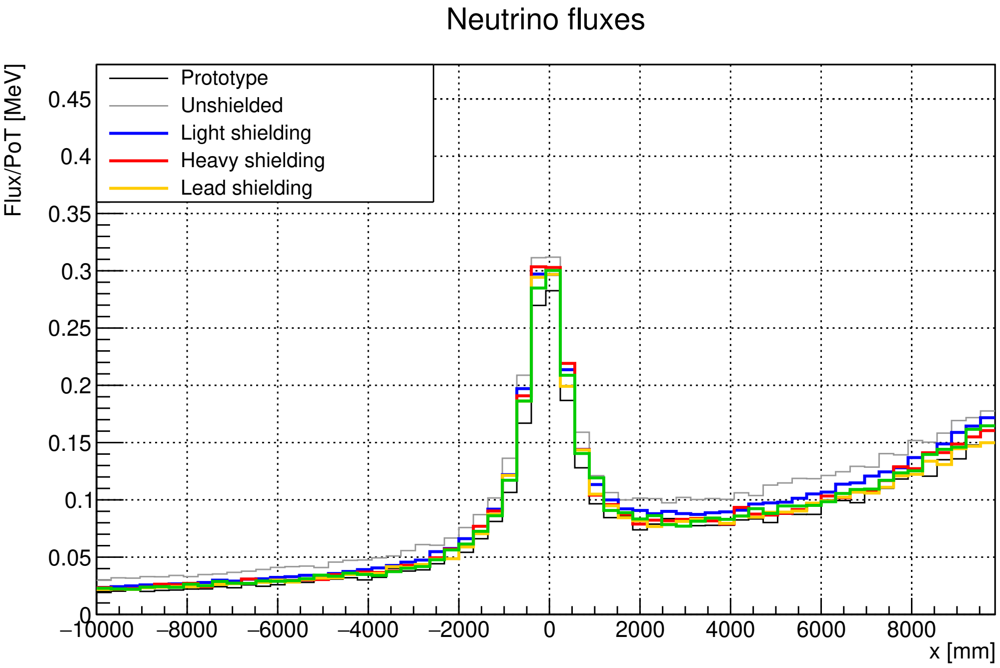

Figure 3.28: Graph of FVD neutrino hits heatmap projected on x axis, cut at $y \in [-2000, 2000]$ mm. Benchmark designs are also reported.

Low energy neutrinos counts are also analysed to double check S/N ratios results. All relative plots are reported in Figure 3.29, with all relative data reported in Table 3.17. Numerical analysis on neutrino counts confirm what has already been seen in S/N ratios analysis: heavy and lead shieldings are best choices, in particular low energy neutrino counts in lead shielding testing are reduced by 29.7% for electronic neutrinos and 38.9% for muonic neutrinos, while for heavy steel shielding same reductions are 17.6% for electronic neutrinos and 23.3% for muonic neutrinos; tungsten shielding has results similar to steel shielding, with a 15.7% reduction of low energy electron neutrinos count and 24.2% low energy muonic neutrinos reductions. In total, data indicates lead as best material for dipole shieldings.

Design	ν_e **(low)**	ν_e **(high)**	ν_μ **(low)**	ν_μ **(high)**
Light sh.	2.293×10^{-5}	6.296×10^{-6}	12.05×10^{-4}	4.918×10^{-4}
Heavy sh.	2.049×10^{-5}	6.875×10^{-6}	11.28×10^{-4}	4.940×10^{-4}
Lead sh.	1.749×10^{-5}	6.230×10^{-6}	9.204×10^{-4}	4.064×10^{-4}
Tungsten sh.	2.098×10^{-5}	5.340×10^{-6}	10.87×10^{-4}	4.913×10^{-4}
Unshielded (ref.)	2.488×10^{-5}	6.792×10^{-6}	14.71×10^{-4}	5.041×10^{-4}
Prototype (ref.)	1.686×10^{-5}	5.387×10^{-6}	9.542×10^{-4}	4.196×10^{-4}

Table 3.17: Neutrino counts, divided by energy range and leptonic flavor, for dipole shielding designs and their reference designs. Low energy count refer to neutrinos of energy < 1 GeV, high energy count for > 1 GeV. Counts are normalized on PoT event count.

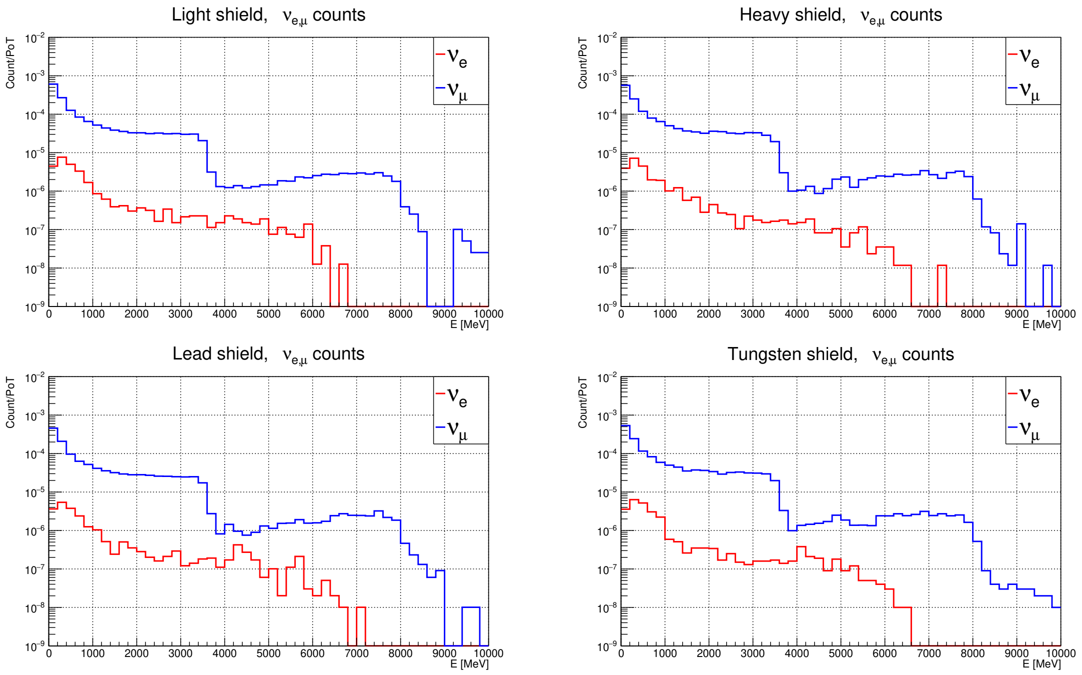

Figure 3.29: Neutrino fluxes on FVD, cut at the LArTPC section, for each dipole design. ν_e and ν_μ fluxes are reported separately.

Considering both S/N ratios and neutrino counts, the final analysis shows that lead is the best material for dipole shielding, having best test results across the board. Lead shielding can however be problematic because of overheating due to radiation, since its melting point of 601 K is relatively low compared to steel (1783 K) and tungsten (3695 K); while a complete melting of the shielding structure can be discarded as a possibility, structure integrity could be compromised. A possible solution to this problem could be using a lead alloy with a higher melting temperature, instead of pure lead.

3.2.5 Final design

Accounting for all data gathered in previous sections, a final shielding design, accounting for all previously analyzed blocks, has been drafted. Considering all approximations done in the Geant4 beamline simulations, this final design should be interpreted more as a guideline for future developments rather than an exact blueprint to follow.

In the end, the shielding design consists of:

- for the target, the “Lead” shielding design has been chosen, as described in Subsection 3.2.2.
- no shielding is present along the first beamline section
- dipoles sides are shielded with lead; design used is “Lead” dipoles shielding, as described in Subsection 3.2.4.

Final S/N ratio and neutrino fluxes estimations are reported respectively in Table 3.18 and 3.19. Final estimation S/N ratio for the beamline is 0.9127, a 69% increase with respect to the fully unshielded, “naked” beamline model. Low energy neutrino counts are also sharply reduced, halved for both muonic and electonic neutrinos.

Design	**Signal [MeV/PoT]**	**Background [MeV/PoT]**	**S/N**
Final	0.9150	1.0025	0.9127
Naked (ref.)	0.8530	1.5792	0.5402

Table 3.18: Signal and background data for final shielding design.

Design	ν_e **count (low)**	ν_e **count (high)**	ν_μ **count (low)**	ν_μ **count (high)**
Final	1.984×10^{-5}	5.360×10^{-6}	11.87×10^{-4}	4.968×10^{-4}
Naked (ref.)	4.070×10^{-5}	10.50×10^{-6}	22.18×10^{-4}	5.321×10^{-4}

Table 3.19: Neutrino counts, divided by energy range and leptonic flavor, for final design and “naked” design as comparison. Low energy count refer to neutrinos of energy < 1 GeV, high energy count for > 1 GeV. Counts are normalized on PoT event count.

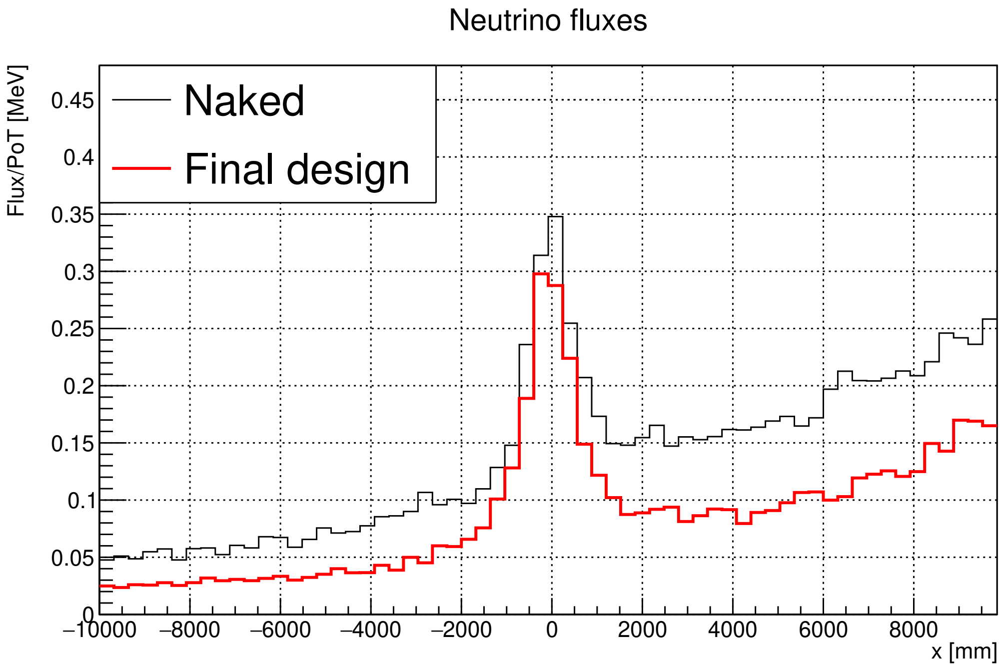

Figure 3.30: Graph of FVD neutrino hits heatmap projected on x axis, cut at $y \in [2000, 2000]$ mm, for “final” and “naked” designs

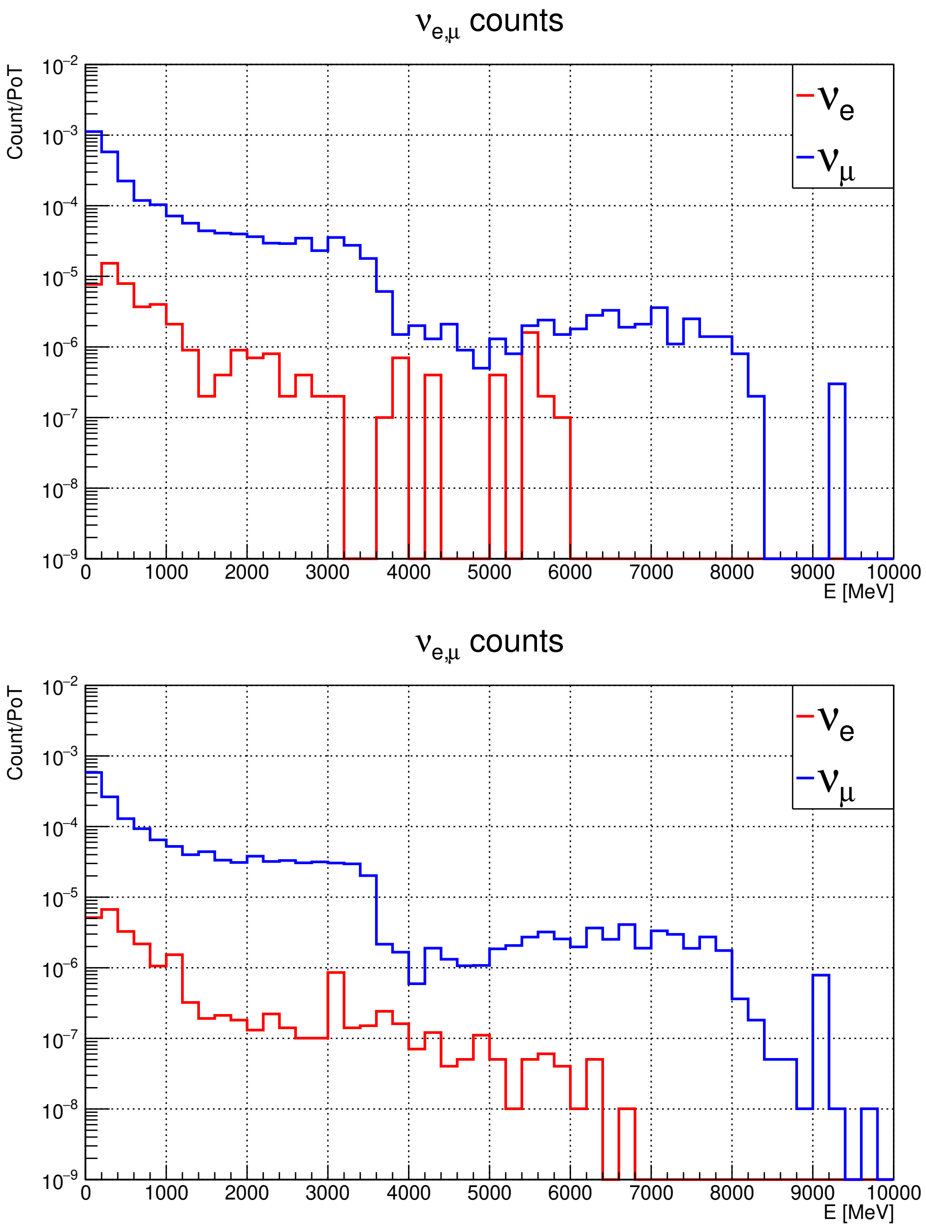

Figure 3.31: Neutrino fluxes on FVD, cut at the LArTPC section, for “naked” (up) and “final” (down) shielding designs. ν_e and ν_μ fluxes are reported separately.

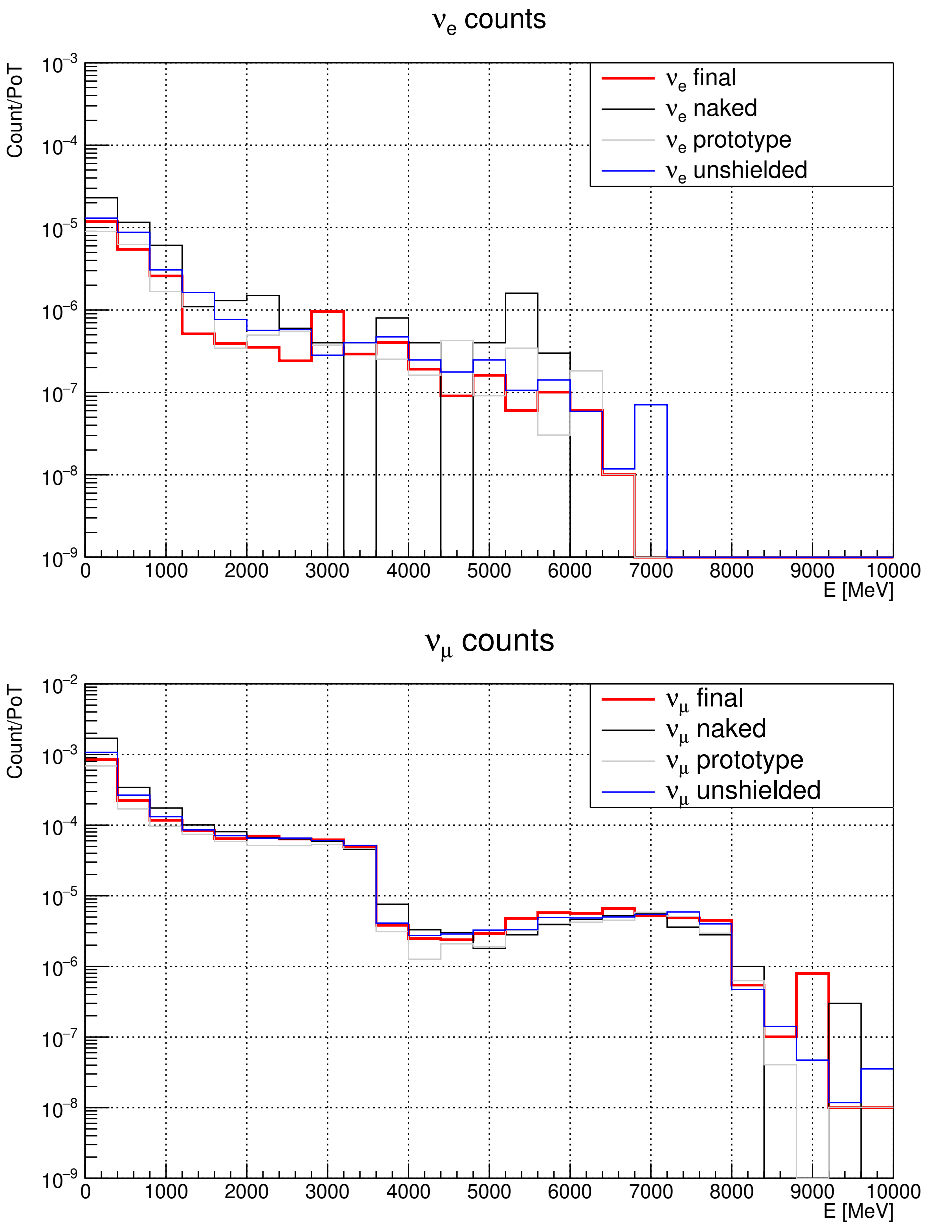

Figure 3.32: Electronic neutrino (up) and muonic neutrino (down) fluxes as a function of energy for final shielding design, compared with benchmark designs.

Conclusions

During this master thesis work I built up a full functioning simulation of the ENUBET beamline project in a Geant4 environment, in order to construct a simulating tool that was able to track particles evolution from production at target to decay tunnel entrance.

The first part of my work focused on the translation of the original `bdsim` code describing the optimized beamline to a pure Geant4 code. All beamline elements have been reconstructed and placed in their positions, along with all the elements surrounding the beamline; in particular, all concrete elements, rock layers, and prototypes for particle shielding, have been simulated too. To track particles inside the beamline and neutrinos produced, a series of virtual detector has been placed along the beamline; real silicon detectors have also been placed to simulate NuTag fast-tracking detectors, which are planned to work alongside the ENUBET tagger.

A first analysis was done on beamline performances. Mesons yields, near neutrino detector positions and positron absorber effects have been studied and measured, to check proper simulation functionality; for this analysis pion and kaon rates and energies at decay tunnel entrance, positron cut at lead plate position, and neutrino fluxes on near LArTPC detector have been studied. In total, all gathered data meet the expectations.

The second part of my study focused on the shield design; starting from some benchmark designs, each important section of the beamline (target, first line, dipoles) has been tested with different shielding designs and materials, to properly develop a final configuration. To test shielding performances, S/N ratio and low energy neutrino fluxes on near detector have been computed and compared, in order to find the design and the material best suited for this part. Final design consist of a series of heavy lead shielding around the target and dipoles, which gives a 69% increase in the S/N ratio and reduces low energy neutrino fluxes by $\sim 50\%$.

Finally, an important result of this work is the simulation software in itself; this tool will be useful for future simulation studies on beamline optimization, shielding designs, or to simulate behavior of newly implemented apparatuses, like muon spectrometers or the LArTPC near detector. Future studies may also include testing other materials for shielding purpose, in particular alloys or compound materials. This flexible and neat newly developed Geant4 framework furthermore will allow reproducing on the `bdsim` optimized beamline, the statistical analysis that proved possibility of reduction of the systematics of the fluxes at 1% level as described in [1].

Bibliography

[1] F. Acerbi *et al.*, "Design and performance of the enubet monitored neutrino beam," 2023. doi: `https://arxiv.org/abs/2308.09402`.

[2] C. Giunti and C. W. Kim, *Fundamentals of Neutrino Physics and Astrophysics.*

[3] G. Bellini *et al.*, "Neutrino oscillations," *Advances in High Energy Physics, 191960 (2014).* doi: `https://doi.org/10.48550/arXiv.1310.7858`.

[4] K. Zuber, *Neutrino Physics.* Section 8.5.

[5] I. Esteban *et al.*, "Nufit-6.0: Updated global analysis of three-flavor neutrino oscillations," *Prepared for submission to JHEP (7 Oct. 2024).* doi: `https://doi.org/10.48550/arXiv.2410.05380`.

[6] "Nufit 6.0," `http://www.nu-fit.org/?q=node/294`.

[7] J. Formaggio and G. Zeller, "From ev to eev: Neutrino cross-sections across energy scales," *(27 Nov. 2024).* doi: `https://doi.org/10.48550/arXiv.1305.7513`.

[8] S. Navas *et al.*, "Particle data group," *Phys. Rev. D110 (2024).* URL: `http://pdg.lbl.gov`.

[9] The K2K Collaboration, "Measurement of neutrino oscillation by the k2k experiment," *(26 Nov. 2024).* URL: `https://doi.org/10.48550/arXiv.hep-ex/0606032`.

[10] T. K. G. J. Feldman, J. Hartnell, "A review of long-baseline neutrino oscillation experiments," *Advances in High Energy Physics 2013 (2013), 475749.* URL: `https://doi.org/10.48550/arXiv.1210.1778`.

[11] T. K. G. J. Feldman, J. Hartnell, "The minos experiment: results and prospects," *(2 Jul. 2013).* URL: `https://doi.org/10.48550/arXiv.1307.0721`.

[12] J. Bian, "The nova experiment: Overview and status," 2013. URL: `https://arxiv.org/abs/1309.7898`.

[13] N. Agafonova *et al.*, "Observation of a first ν_τ candidate event in the opera experiment in the cngs beam," *Physics Letters B*, vol. 691, p. 138–145, July 2010. URL: `https://doi.org/10.48550/arXiv.1006.1623`.

[14] F. Terranova *et al.*, "Sbn@cern: A short-baseline neutrino beam at cern for high-precision cross-section measurements," 2025.

[15] The T2K Collaboration, “Constraint on the matter–antimatter symmetry-violating phase in neutrino oscillations,” *Nature*, vol. 580, p. 339–344, Apr. 2020. URL: `http://dx.doi.org/10.1038/s41586-020-2177-0`.

[16] The Hyper-Kamiokande Proto-Collaboration, “Hyper-kamiokande design report,” 2018.

[17] The NOνA Collaboration and D. Ayres, “Nova proposal to build a 30 kiloton off-axis detector to study neutrino oscillations in the fermilab numi beamline,” 2005. URL: `https://arxiv.org/abs/hep-ex/0503053`.

[18] B. Dasgupta and J. Kopp, “Sterile neutrinos,” *Physics Reports*, vol. 928, p. 1–63, Sept. 2021.

[19] T. A. Mueller *et al.*, “Improved predictions of reactor antineutrino spectra,” *Physical Review C*, vol. 83, May 2011.

[20] J. M. Berryman *et al.*, “Sterile neutrino at the deep underground neutrino experiment,” *Physical Review D*, vol. 92, Oct. 2015.

[21] A. Longhin, L. Ludovici, and F. Terranova, “A novel technique for the measurement of the electron neutrino cross section,” *The European Physical Journal C*, vol. 75, Apr. 2015.

[22] C. C. Delogu, *Beamline design and calorimeter prototypes for the ENUBET monitored neutrino beam facility.* PhD thesis, Università degli Studi di Padova, 2022.

[23] L. Halić *et al.*, “The enubet monitored neutrino beam and its implementation at cern,” 2025.

[24] A. Hoecker *et al.*, “Tmva - toolkit for multivariate data analysis,” 2009.

[25] F. Pupilli *et al.*, “Lepton reconstruction in the ENUBET tagger,” *PoS*, vol. NuFact2021, p. 025, 2022.

[26] A. Baratto-Roldán and M. Perrin-Terrin, “Nutag: proof-of-concept study for a long-baseline neutrino beam,” 2024.

[27] M. Perrin-Terrin, “Neutrino tagging: a new tool for accelerator based neutrino experiments.”

[28] F. Pupilli *et al.*, “The enubet narrow band neutrino beam,” 04 2019.

[29] The GEANT4 Collaboration, “Introduction to geant4, release 11.3.”

[30] V. V. Uzhinsky, “Fritiof (ftf) model.”

[31] J. Apostolakis *et al.*, “Geometry and physics of the geant4 toolkit for high and medium energy applications,” *Radiation Physics and Chemistry*, vol. 78, no. 10, pp. 859–873, 2009. Workshop on Use of Monte Carlo Techniques for Design and Analysis of Radiation Detectors.

[32] S. Agostinelli *et al.*, “Geant4—a simulation toolkit,” *Nuclear Instruments and Methods in Physics Research Section A: Accelerators, Spectrometers, Detectors and Associated Equipment*, vol. 506, no. 3, pp. 250–303, 2003.

[33] E. Wilson and B. J. Holzer, *Particle Physics Reference Library, Volume 3: Accelerators and Colliders.*

[34] B. L, M. Clément, K. Elsener, H. Gaillard, L. A. López-Hernandez, J. M. Maugain, M. Meddahi, S. Rangod, A. Spinks, G. R. Stevenson, and M. Wilhelmsson, “CNGS layout and systems: a progress report,” tech. rep., CERN, Geneva, 2003.

[35] M. Haas, A. de Haller, A. Moscariello, L. Scibile, M. Benedikt, N. Gegenhuber, and R. Galler, “A mineralogical re-use classification model of molasse rock mass in the geneva basin,” Nov. 2020. ISRM International Symposium - EUROCK 2020 ; Conference date: 14-06-2020 Through 19-06-2020.

[36] “Centre de Calcul de l’IN2P3.” website.